Leptons as a Window to Dark Matter

by

Aria Rose Radick

A dissertation accepted and approved in partial fulfillment of the
requirements for the degree of
Doctor of Philosophy
in Physics

Dissertation Committee:
Tim Cohen, Chair
Tien-Tien Yu, Advisor
David Strom, Core Member
Cathy Wong, Institutional Representative

University of Oregon
Summer 2024

DISSERTATION ABSTRACT

Aria Rose Radick

Doctor of Philosophy in Physics

Title: Leptons as a Window to Dark Matter

There is a huge amount of evidence the dark matter exists, however we still do not know what kind of particle it is. Many experiments have been performed to test different models for dark matter, but its nature still remains elusive. In this work we study two different ways of looking for dark matter by using leptons.

First, we look at low threshold experiments in the form of dark matter-electron scattering. We know that the rate of dark matter-electron scattering depends on the underlying velocity distribution of the dark matter halo. In particular, dark matter electron scattering is more sensitive to the high velocity tail which can be significantly different depending on the dark matter halo model. This work quantifies the effects of different dark matter halo models and parameter choices on these rates, finding an $\mathcal{O}(0.01\%)$ to $\mathcal{O}(100\%)$ change in the rate predictions in silicon targets.

Secondly, we use a different lepton, the muon, to search for dark matter at colliders. In particular, we simulate a particular class of dark matter model, known as flavored dark matter, at a theoretical future muon collider to predict the capability of such a machine to detect or place bounds on this model, if it were to be built. We focus on the less-explored regime of feeble dark matter interactions, which suppresses the dangerous lepton-flavor violating processes, gives rise to dark matter freeze-in production, and leads to long-lived particle signatures at colliders. We find that the interplay of dark matter freeze-in and its mediator

freeze-out gives rise to an upper bound of around TeV scales on the dark matter mass. The signatures of this model depend on the lifetime of the mediator, and can range from generic prompt decays to more exotic long-lived particle signals. In the prompt region, we calculate the signal yield, study useful kinematics cuts, and report tolerable systematics that would allow for a 5σ discovery. In the long-lived region, we calculate the number of charged tracks and displaced lepton signals of our model in different parts of the detector, and uncover kinematic features that can be used for background rejection. We show that, unlike in hadron colliders, multiple production channels contribute significantly which leads to sharply distinct kinematics for electroweakly-charged long-lived particle signals.

This dissertation includes previously published co-authored material.

CURRICULUM VITAE

NAME OF AUTHOR: Aria Rose Radick

GRADUATE AND UNDERGRADUATE SCHOOLS ATTENDED:

University of Oregon, Eugene, OR, USA
California State University Chico, Chico, CA, USA

DEGREES AWARDED:

Doctor of Philosophy, Physics, 2024, University of Oregon
Master of Science, Physics, 2020, University of Oregon
Bachelor of Science, Physics, 2018, CSU Chico
Bachelor of Science, Applied Mathematics, 2018, CSU Chico

AREAS OF SPECIAL INTEREST:

Dark Matter, Physics Beyond the Standard Model, Collider Physics, Direct Detection

PROFESSIONAL EXPERIENCE:

Graduate Research Assistant, University of Oregon, 2019-2024
Graduate Teaching Assistant, University of Oregon, 2018-2024

GRANTS, AWARDS AND HONORS:

Floyd L. English Scholarship, CSU Chico, 2017-2018
Dean's List, CSU Chico, 2015-2018

PUBLICATIONS:

A. Radick, A.-M. Taki, and T.-T. Yu, “Dependence of Dark Matter - Electron Scattering on the Galactic Dark Matter Velocity Distribution,” JCAP 02 (2021) 004, arXiv:2011.02493 [hep-ph]

P. Asadi, A. Radick, and T.-T. Yu, “Interplay of freeze-in and freeze-out: Lepton-flavored dark matter and muon colliders,” Phys. Rev. D 110 no. 3, (2024) 035022, arXiv:2312.03826 [hep-ph]

ACKNOWLEDGEMENTS

I first would like to thank my advisor, Tien-Tien Yu, for your guidance throughout the years. I am especially grateful for you graciously accepting my need for a break when I was burned out at the end of my second year, and accepting my desire to change research directions later on in my studies.

Thank you to Pouya Asadi and Ben Lillard for not only being a fantastic collaborators, but also great friends. Pouya, thank you for resparking my interest in doing physics by leading me down a different research path and convincing me to break out of my "pandemic shell" and start socializing with everyone else in the group again. I will not forget the fun we all had at board game nights. Ben, thank you for giving me the opportunity to work with you on a very exciting project that I had so much fun working on over the last 6 months. I am especially grateful to you for being so supportive as I got back into playing trombone, and coming to all my concerts. Both of you were instrumental in making my last year of grad school an enjoyable one.

To the High Energy Theory group here more broadly – Cristien Arzate, Pouya Asadi, Austin Batz, Tom Bouley, Layne Bradshaw, Spencer Chang, Tim Cohen, Joel Doss, Thomas Driscoll, Haidar Esseili, Ivan Juarez-Reyes, Graham Kribs, Ben Lillard, Xiaochuan Lu, Thomas Schwemberger, Dave Soper, Anna-Maria Taki, Tom Tong, Tien-Tien Yu – thank you for all the discussions and helping me to be a better physicist and researcher. Thank you to Claire Staley for being a great friend and listening to me as I relentlessly stress about finding a job.

Thank you to all the graduate students at University of Oregon, especially Adrian Helmling-Cornell, Viola Lum, and Will Parker, for your camradarie and friendship. Adrian, I'll always look back fondly on wildly explaining my various relationship woes to you during our first year.

Finally, I would like to acknowledge my wonderful and supportive partner, Rori Forcht, who was instrumental in helping me make it through my degree. You endured many nights of me working late to finish my projects and were always there for me through countless tears, my break from grad school, and more. I am eternally grateful for having you in my life.

TABLE OF CONTENTS

LIST OF FIGURES

Figure Page

Figure Page

Figure Page

Figure Page

Figure Page

Figure Page

Figure Page

LIST OF TABLES

Table | Page

Table Page

CHAPTER I

INTRODUCTION

The Standard Model of particle physics is one of the most successful theories of all time. Among its famous successes are the prediction of the electron anomalous magnetic dipole moment to within better than one part in one trillion [5], and the prediction of the existence of the Higgs boson, which was discovered at the LHC in 2012 [6, 7]. However, there are still many phenomena it fails to describe, including the existence of dark matter, neutrino masses, the origin of the electroweak scale, and more. One of the primary goals of particle physicists in the present age the is to understand the particle nature of dark matter.

We have a huge amount of evidence that dark matter exists [8]. In the 1930s, Oort [9] and Zwicky [10] performed some of the first observations that implied the existence of dark matter. Oort observed the velocity of stars in our solar neighborhood, and saw that they were moving too fast to be explained by only the visible matter in the galaxy. Zwicky performed an analysis using the virial theorem on the Coma galaxy cluster, which predicted a much larger mass for the cluster than the measured amount of luminous mass. Approximately thirty years later, Vera Rubin measured the rotation curves of spiral galaxies and discovered that they did not follow the expected distribution ($v_r \propto r^{-1/2}$), but instead had a nearly flat velocity profile away from the center [11]. This difference can be explained by a density distribution that falls off more slowly than the observed density distribution, implying that galaxies appear to be surrounded by a halo of dark matter.

Gravitational lensing, or how photons' paths appear to bend as they pass near massive objects, is another important source of evidence for dark matter.

Lensing observations have led to many important conclusions, including the fact that there is about five times more dark matter than baryonic matter, dark matter has at most very small cross sections with both itself and visible matter, dark matter is cold (i.e., non-relativistic), and more [12]. In particular, the fact that the amounts of dark matter and visible matter are so close seems to imply that there must be some interaction between the sectors. This provides a strong basis for looking for dark matter through its interactions with the SM.

Still more evidence comes from the cosmic microwave background (CMB), which was created when electrons and protons combined to form hydrogen and the photons in the CMB stopped interacting and started traveling through space freely [13]. The CMB provides a very high precision measurement of the total amount of dark matter in the universe. This is done by measuring the anisotropies in the power spectrum of the temperature, which are correlated with density fluctuations in the early universe, giving us an amount of cold dark matter $\Omega_\chi = 0.2589(57)$ [14]. We can use this measurement to put constraints on the strength of dark matter interactions, depending on the exact process that produced dark matter in the early universe.

There are two common production mechanisms that are hypothesized. The first is freeze-out: we assume that particles begin in thermal equilibrium with each other, including the DM. Interactions with other particles maintain thermal equilibrium between the species, but as the universe expands particles have a harder time finding interaction partners, until the point at which they decouple and remain at a fixed temperature or “freeze out”. The amount of DM left over is dependent on its annihilation cross section, the stronger the interactions the less DM remains, and vice-versa. On the other hand, if the dark matter’s interaction strength is incredibly small it could begin not in thermal equilibrium and be produced slowly through some channel as the universe is expanding. This process is known as freeze-in and has the opposite trend as freeze-out: as the interaction strength increases, there is more dark matter left over. Finally, in both cases one can solve the Boltzmann equations in order to predict the number of DM particle that will be left. For both processes the total number of DM particles left over is also dependent on the DM mass. The heavier the DM, the fewer number of particles are left over for the same energy budget. The combination of these factors leads to a relationship between the dark matter mass and its interaction strength for a given model.

Given all of this evidence, one can ask the question "what is dark matter?", as in, what kind of particle is dark matter? The evidence that we outlined above is purely gravitational, we have not yet observed dark matter interacting with the SM through any other forces. However, as stated above, it seems logical to conclude that dark matter must have some interaction with the SM, and so experimentalists have come up with many ways to look for it. Unfortunately, dark matter's interactions with the SM are likely incredibly small – and experiments have pushed a lot of this parameter space to even smaller cross-sections – so experimentalists have their work cut out for them.

The three main methods that we have for looking for dark matter are production at colliders, direct detection, and indirect detection. Collider production involves directly producing the dark matter through collisions of high energy particles. Given that dark matter interacts so weakly with the SM, we would not be able to directly see the dark matter itself, instead we would observe differences in the kinematic distributions as a result of missing transverse energy or the signatures of intermediate particles that decay to dark matter. Direct detection involves putting a large amount of material deep underground and waiting for the dark matter around us to scatter with it and create a signal. This relies on several things we know about dark matter: we know that there is some amount of dark matter moving through us at all times, because our galaxy is surrounded by halo of dark matter, we know that the dark matter is moving at non-relativistic speeds, because it's cold, and we assume that the dark matter can interact with the materials in some way. Finally, indirect detection involves looking for the products of dark matter interactions, effectively the inverse of production at colliders. These can show up as a variety of signals, and require varied instrumentation in order to detect, including gamma, x-ray, radio, or neutrino telescopes, or even instruments which can detect cosmic rays [15]. In this work, we will focus on collider production and direct detection.

The original idea for dark matter direct detection began as an experiment to detect neutrinos scattering elastically off nuclei, originally thought up by Drukier and Stodolsky in 1984 [16]. Shortly after, Goodman and Witten published a paper theorizing that this technology could also be used to detect dark matter [17]. As a result of dark matter being cold, and thus non-relativistic, it is possible to simplify the operator space down to two main types of interactions, spin-dependent and spin-independent scattering. This idea essentially served as the basis for decades of dark matter direct detection experiments, beginning with dark matter-nuclear scattering experiments. The first of these experiments took place in South Dakota in 1986, led by scientists from the Pacific Northwest National Laboratory using a germanium ionization detector [18]. Unfortunately, this experiment, and others like it, were very background limited. Though, it was not long before a solution to this was hypothesised: due to the earth's motion around the sun, we can expect there to be annual variation in the rate of direct matter direct detection. This variation most likely does not appear in any background sources, so it can be used to distinguish signal from background. This technique was first suggested by Drukier, Freese, and Spergel [19], and DD experiments still employ it to this day.

Since then, there have been a wide variety of DM-nuclear experiments, and they have been very successful in placing constraints on dark matter masses above 1 GeV, which is generally their lower limit for masses. Due to the lack of a confirmed signal, it is natural to wonder if DM might be more complex than the simple WIMP models that usually have masses that lie above 1 GeV. This leads to possibilities for masses in a much wider range, in particular the meV to GeV range, which newer so-called "low-threshold" experiments are able to probe. These experiments include devices capable of detecting single electrons, like time projection chambers (TPCs) and silicon skipper-CCDs [20]. Being relatively recent, these types of experiments are relatively less mature, but show very promising projections going forward. This dissertation features work that focuses on silicon skipper-CCD experiments.

Historically, there have been two major types of colliders: proton colliders and electron-positron colliders. Generally, proton colliders push the energy frontier, while electron-positron colliders push the precision frontier. This can be illustrated by the fact that many particles, including the top quark [21, 22], the W and Z bosons [23], and the Higgs boson [6, 7], were first discovered at hadron colliders, but the masses of the W and Z bosons were given more precisely by LEP [23], an electron-positron collider. The reason for this dichotomy is that electron-positron systems have very clean final states, because electrons are fundamental particles.

The downside is that because they are so light, there is a limit to how much energy we can give them due to synchrotron radiation, which causes electrons to lose energy in the form of photons as they are rotated around a circle. Building a linear collider can sidestep some of this, but it takes a lot more power to accelerate the electrons to the same energies. On the other hand, protons are a lot heavier, so they do not lose much energy to synchrotron radiation, but because they are composite particles, the final states are rather messy. It can be thought of as akin to throwing two trash bags at each other, and looking for diamonds to come out. While there have been many successes, there are still many unanswered questions as well, leading many to the conclusion that we should build more colliders: new electron-positron colliders to precisely measure the properties of the Higgs boson, and new proton colliders to directly look for new particles. Possible new colliders along these lines include FCC-ee, FCC-hh, and CEPC [24].

However, there is another option: a muon collider [25]. Muons are fundamental particles like electrons, so they have relatively clean final states and their full energy is available in a collision. They are also heavier than electrons, so we can accelerate them to much higher energies like we can for protons. This creates a solution to the dichotomy between proton and electron colliders. Even better, muons have a sizable vector boson component to their parton distribution function, such that a muon collider can also be thought of of as a vector boson collider. It is possible that a muon collider could both reach higher energies than the LHC and yield extremely high precision measurements. Is is not all perfect though, because muons are unstable, their decays have to be contended with. But, work is being done to solve these problems and P5 even recommended funding for further muon collider R&D (the "muon shot") [26], showing that there is community support for such a machine. Moving forward, it is useful to think about what kinds of physics we can look for at a muon collider, both to further support its construction and to guide the design in order to maximize our ability to study new physics. Thus, in this work we look at some particular models that we can search for at a muon collider.

1.1 Dependence of Dark Matter – Electron Scattering on the Galactic Dark Matter Velocity Distribution

The interpretations of DD experimental results in terms of DM-Standard Model interactions are sensitive to the astrophysical properties of the local DM halo distribution, such as the local DM density, the mean DM velocity, and DM velocity dispersion. The benchmark distribution is the Standard Halo Model (SHM) in which the DM particles are distributed in an isothermal sphere with an isotropic Maxwellian velocity distribution [19]; this type of distribution follows from a system of collisionless particles and gives a convenient proxy for the velocity profile of the DM halo due to its simple analytic form (see *e.g.* [27]). Despite its convenience, the SHM fails to provide an accurate description of how DM is distributed throughout the Galaxy (see detailed discussion in §2.2.1 and §2.2.3). This motivates the study of alternative halo models for the DM velocity distribution function (VDF). Given that the DM VDF cannot be reliably extracted from direct measurements, other methods to infer the DM halo distribution include performing numerical cosmological simulations (see relevant discussion in §2.2.3), employing Eddington's formalism [28, 29], or using stellar populations that faithfully trace the DM component [30, 31].

The effects of the uncertainties in the DM VDF on the DD observables have been studied in the past for DM-nuclear scattering interactions [32–35]. In this work, we investigate the impact of such uncertainties in the context of DM-electron scattering. The differences in the kinematics of DM-nuclear scattering compared to the DM-electron scattering warrants a dedicated analysis to explore these effects. In the latter case, the momentum transfer between the DM and the electron is dominated by the electron's momentum. However, DM masses that sit at the experimental threshold are especially sensitive to the high-velocity tail of the halo's VDF. Currently, there are several experiments with dedicated searches for DM-electron scattering such as SENSEI [36–39], SuperCDMS-HV [40], DAMIC [41], Edelweiss [42], that have recently taken or are actively taking data. The next decade will see the arrival of larger silicon CCD experiments such as the 1-kg DAMIC-M [43, 44] and the proposed 10-kg Oscura [45] experiments. Understanding the influence of astrophysical uncertainties on the observables of DM-electron scattering will allow us to interpret the results of these experiments in a more robust way.

1.2 Interplay of Freeze-In and Freeze-Out: Lepton-Flavored Dark Matter and Muon Colliders

Various future collider experiments are proposed to push the energy frontier. One such option that, thanks to increasing community interest (see *e.g.* [46]), has risen as a compelling contender is a Muon Collider (MuC) [47–52]. There are considerable technical challenges that need to be overcome before a viable high energy MuC can be constructed, see Refs. [53, 54, 46, 4, 55, 56] for recent reviews. Nonetheless, many theoretical studies are carried out to underscore the reach of such a machine in probing different BSM models and a template of well-motivated targets are being developed for searches at such a facility. The clean environment of a lepton collider, combined with substantial parton distribution function (PDF) of electroweak gauge bosons in a muon at TeV scales, turns such a machine into a suitable candidate for an in-depth study of the Higgs and precision electroweak measurements [57–70], flavorful new physics [71–86], DM candidates [87–92], as well as other general SM and BSM physics studies [93–95, 25, 96–105]. There are also proposals for earlier stage facilities, such as a beam dump with accelerated muon beams, and interesting new physics that they can probe [106, 107].

At the moment there exists no final detector design for such a future machine. Theoretical works tabulating well-motivated models can inform development of such a design. In particular, there are many well-motivated DM models that can be searched for at a MuC, including various minimal Weakly-Interacting Massive Particle (WIMP) DM models [87]. Many of these DM models, including WIMPs, are strongly constrained by direct detection searches.

In this work, we focus on a less-constrained – yet similarly minimal – class of DM models, namely flavored DM [108–116]. In such setups, the DM, which is a singlet fermion of the SM, interacts with the SM only via a new scalar mediator with the same charges as one of the SM fermion fields. We focus on the setup where the new mediator has the same charges as right-handed (RH) leptons of the SM, and study its relic abundance calculation and signals at a MuC.

Previous works on flavored DM models have focused on DM production through thermal freeze-out [108–116]. A sub-TeV DM mass gives rise to the correct relic abundance in such setups. DM coupling to SM leptons should be aligned with SM lepton Yukawa matrix in order to suppress dangerous flavor-changing neutral current (FCNC) and lepton-flavor violation (LFV) processes. These constraints can be abated by decreasing the size of the DM-mediator Yukawa coupling, which opens up a new mechanism for DM production: freeze-in [117]. The smallness of the Yukawa coupling also leads to a rich set of collider signatures, ranging from prompt to long-lived particle (LLP).

In this work, we will study in detail the production mechanism for freeze-in flavored DM, demonstrating how the interplay between mediator and DM abundance leads to a bounded parameter space, as well as the collider signatures at a future MuC. In particular, given the generic nature of the production rate of our model, our signal yield can serve as a benchmark target that will inform future experimental studies.

1.3 Outline

This dissertation is comprised of two analyses that use leptons to search for DM, along with some details of a current project that follows up on one of the previous works.

In Chapter II, we discuss the effects of different assumptions about the DM velocity distribution on DM-electron scattering, in particular for silicon targets. This chapter contains material that was previously published with co-authors Anna-Maria Taki and Tien-Tien Yu [118].

In Chapter III, we discuss the prospects for future muon collider for a specific model of DM, namely right-handed lepton flavored DM. This material has been accepted for publication, though is yet to be published, but a preprint is available. This work was co-authored with Pouya Asadi and Tien-Tien Yu [119].

In Chapter IV, we discuss future work on other flavored dark matter models at muon colliders. This is ongoing work with collaborators Sam Homiller, Pouya Asadi, and Tien-Tien Yu.

CHAPTER II

DEPENDENCE OF DARK MATTER – ELECTRON SCATTERING ON THE GALACTIC DARK MATTER VELOCITY DISTRIBUTION

From A. Radick, A.-M. Taki, and T.-T. Yu, "Dependence of Dark Matter - Electron Scattering on the Galactic Dark Matter Velocity Distribution," JCAP 02 (2021) 004, arXiv:2011.02493 [hep-ph]

2.1 Dark Matter - Electron Scattering Formalism

In this section, we give a brief review of the formalism behind DM-electron scattering; more details can be found in [120]. For a spherically-symmetric DM velocity distribution, the differential rate for DM-electron scattering in a crystal target is given by

$$\frac{dR}{d\ln E_e} = N_{\rm cell}\frac{\rho_{\rm DM}}{m_\chi}\frac{\overline{\sigma}_e \alpha m_e^2}{\mu_{\chi e}^2}\int d\ln q\,\frac{E_e}{q}\left[|F_{\rm DM}(q)|^2|f^{\rm crystal}(E_e,q)|^2\eta(v_{\rm min}(q,E_e))\right]\,, \tag{2.1}$$

where $\rho_{\rm DM}$ is the local DM density, m_χ is the DM mass, q is the momentum transfer between the DM and the electron, E_e is the energy transferred to the electron, $\alpha \simeq 1/137$ is the fine-structure constant, while m_e and $\mu_{\chi e}$ are the mass of the electron and reduced mass of the DM-electron system, respectively. The material dependence of the rate is encoded in $f^{\rm crystal}(E_e,q)$, which is the crystal form-factor for an electronic transition of E_e and q, and $N_{\rm cell} \equiv M_{\rm target}/M_{\rm cell}$, which counts the number of unit cells per mass in the crystal; for silicon, $M_{\rm cell} = 2\times m_{\rm Si} =$ 52.33 GeV. We use the values of $f^{\rm crystal}(E_e,q)$ calculated from `QEdark` [120] for silicon.[1]

[1] We choose silicon for illustrative purposes. Nonetheless, our calculations can be performed for any semiconductor material with qualitatively the same conclusions. Similar calculations can also be made for noble liquid targets such as xenon and argon; however, noble liquids will be less sensitive to changes in the DM VDF compared with semiconductor crystals.

The momentum-dependent DM-electron scattering cross section due to a mediator particle of mass m_V is factorized as $\sigma_e(q) = \overline{\sigma}_e \times |F_{\rm DM}(q)|^2$, where the interaction strength is given by

$$\overline{\sigma}_e \equiv \frac{\mu_{\chi e}^2 \overline{|\mathcal{M}_{\rm free}(\alpha m_e)|^2}}{16\pi m_\chi^2 m_e^2}\,, \tag{2.2}$$

while the DM form factor

$$|F_{\rm DM}(q)|^2 \equiv \frac{\overline{|\mathcal{M}_{\rm free}(q)|^2}}{\overline{|\mathcal{M}_{\rm free}(\alpha m_e)|^2}} = \begin{cases} 1 & ,\ m_V \gg \alpha m_e \text{ (contact)} \\ \left(\frac{\alpha^2 m_e^2}{q^2}\right)^2 & ,\ m_V \ll \alpha m_e \text{ (light med.)} \end{cases} \tag{2.3}$$

expresses the momentum dependence of the interaction – the top line corresponds to a contact interaction via a heavy vector mediator, while the bottom line corresponds to a long-range interaction via the exchange of a massless or ultralight vector mediator. $\mathcal{M}_{\rm free}(\vec{q})$ is the matrix element for the free-elastic scattering of DM with an electron, while $\overline{|\mathcal{M}|^2}$ denotes the absolute square of $\mathcal{M}$ averaged over initial and summed over final particle spins. The DM halo velocity profile is encoded in the velocity average of the inverse speed, defined as

$$\eta(v_{\rm min}) = \int \frac{d^3v}{v} f_\chi(v)\,\Theta(v - v_{\rm min}) \tag{2.4}$$

where Θ is the Heaviside step function. Energy conservation is captured by the minimum speed needed by the DM particle in order for an electron to gain energy E_e with momentum transfer q,

$$v_{\rm min}(E_e, q) = \frac{E_e}{q} + \frac{q}{2m_\chi}, \tag{2.5}$$

while $f_\chi(v)$ is the velocity distribution of dark matter in our Galaxy and is the focus of our work. Note that $f_\chi(v)$ is evaluated in the detector (Earth) frame and is sensitive to the Earth's velocity. This dependence manifests itself as an annual modulation of the count rate, which we will discuss in more detail in §2.3.4.

DM-electron scattering experiments measure electron-hole pairs N_e, rather than electron energy E_e. The conversion of E_e to N_e involves secondary scattering processes, the exact modeling of which is ongoing and beyond the scope of this work. Instead, we use a linear response model given by

$$N_e = 1 + \left\lfloor \frac{E_e - E_g}{\varepsilon} \right\rfloor , \tag{2.6}$$

that provides a reasonable estimate for the conversion of E_e to N_e. Here, E_g is the band-gap energy of the detector material and ε is the energy needed to produce an additional electron-hole pair above the band-gap. The floor operator $\lfloor x \rfloor$ rounds x down to the nearest integer. The corresponding values for silicon are measured at $E_g \simeq 1.2$ eV and $\varepsilon \simeq 3.8$ eV [121, 122].

We end this section with a discussion about the kinematics of DM-electron scattering and its dependence on the DM velocity. In DM-electron scattering the target is a bound electron; therefore, the electron does not have a definite momentum but rather can take on a wide range of values. One can relate the momentum transfer q to E_e via energy conservation, according to

$$E_e = \vec{q} \cdot \vec{v} - \frac{q^2}{2m_\chi} . \tag{2.7}$$

Since the velocity of a bound electron is $v_e \sim Z_{\text{eff}}\alpha \gg v_\chi \sim 10^{-3}$, the typical momentum transfer is set by the electron's momentum. Therefore, $q_{\text{typ}} \sim Z_{\text{eff}}\alpha m_e$, where $Z_{\text{eff}} = 1$ for the outer shell electrons and increases for inner shells.

The energy transfer in eq. 2.7 is dominated by the first term on the right-hand side for m_χ well-above the threshold energy, $E_{\text{min}} = \frac{1}{2}\mu_{\chi N}^2 v^2 \simeq \frac{1}{2}$ eV $\left(\frac{m_\chi}{\text{MeV}}\right)$, where $\mu_{\chi N}$ corresponds to the reduced mass of the DM-nucleus system. In this regime, the minimum momentum transfer required to obtain an energy transfer E_e is given by $q_{\text{min}} = E_e/v \sim E_e/(Z_{\text{eff}} \cdot 4 \text{ eV}) \times q_{\text{typ}}$. What we learn from this scaling is that the typical momentum transfer leads to transitions of a few eV; a more energetic transition requires higher DM velocity, or, alternatively, a high electron momentum which is suppressed. From this, we can deduce that the rate is sensitive to the DM halo velocity profile and in what follows we quantify this sensitivity.

2.2 Halo Models

In this section, we describe the halo models under study: the Standard Halo Model, the Tsallis model, and an empirical model derived from numerical simulations. We present the functional forms for the corresponding halo distributions and motivate the choice of each model. Note that although we present the functional forms of the VDFs in the galactic rest frame, the quantity that enters the rate calculation must be evaluated in the Earth's rest frame. The normalization of each halo model satisfies $\int f(v) d^3v = 1$. We show the general form for η and $v^2 f(v)$ for the halo models under discussion in figs. 1 and 2 along with their dependence on astrophysical parameters, which we will discuss in more detail in §2.3.

2.2.1 Standard Halo Model. The Standard Halo Model (SHM) [19] has been featured extensively in several analyses of DM detection experiments, serving as a convenient option for the modeling of the dark halo. The model assumes an isothermal spherical distribution for the Galactic dark matter with a density profile that scales with the distance from the center of the Galaxy as r^{-2}, to match the behavior borne out in the observations of galactic rotation curves. Under these assumptions, an isotropic Maxwell-Boltzmann (MB) velocity distribution emerges self-consistently as the solution to the collisionless steady-state Boltzmann equation [123]. A physical cutoff for the distribution is imposed at the local escape speed v_{esc} while, within this approximation of a singular isothermal sphere, its most probable speed v_0 is identified with the local circular speed [32]. The MB distribution is given by

$$f_{\rm MB}(\vec{v}) \propto \begin{cases} e^{-|\vec{v}|^2/v_0^2} & |\vec{v}| < v_{\rm esc} \\ 0 & |\vec{v}| \geq v_{\rm esc}. \end{cases} \tag{2.8}$$

When boosted to the detector's (Earth) frame, the distribution takes the form

$$f_{\rm SHM}(\vec{v}) = \frac{1}{K} e^{-|\vec{v}+\vec{v}_E|^2/v_0^2} \Theta(v_{\rm esc} - |\vec{v}+\vec{v}_E|), \tag{2.9}$$

where v_E is the Earth's Galactic velocity and

$$K_{\rm SHM} = v_0^3 \left(\pi^{3/2} \, \mathrm{erf}(v_{\rm esc}/v_0) - 2\pi \frac{v_{\rm esc}}{v_0} e^{-v_{\rm esc}^2/v_0^2} \right) \tag{2.10}$$

is the normalization constant that results from enforcing that $\int f(v) d^3v = 1$.

For a spherically-symmetric system with an isotropic velocity tensor, the Eddington formula [28] can be used to derive the DM phase-space distribution function from first principles [124]. This method warrants that the inferred speed distribution flows naturally from the choice of the spatial density profile of the DM component, providing a self-consistent connection to the total gravitational potential of the Galaxy. [2] Though for the scope of this work we are solely interested in distributions for which there is no preferred direction for the velocities of the DM particles at the solar vicinity, if we choose to retire the assumption of isotropy we come across anisotropic realizations of the DM VDF. Such models break the 1-1 direct relation between the density distribution and the velocity distribution of the dark matter [34] and can have important implications for the DM detection observables [128–131]. For some synthetic halos that have been

[2] For a review on the Eddington approach and its anisotropic extensions see ref. [29] and references therein. Generalizations of Eddington's inversion method to axisymmetric systems are considered in refs. [125–127].

found to exhibit such anisotropic behaviors at a varying degree, see representative examples in refs. [132, 133, 32, 134, 135].

The average inverse speed for the SHM can be calculated analytically in two kinematic regimes,

1. $v_{\min} < v_{\text{esc}} - v_E$,

2. $v_{\text{esc}} - v_E < v_{\min} < v_{\text{esc}} + v_E$

where $v_{\text{esc}},\ v_E,\ v_{min} > 0$.

Following ref. [136], we arrive at

$$\begin{aligned}
\eta_1(v_{\min}) &= \frac{v_0^2\pi}{2v_E K}\left(-4e^{-v_{\text{esc}}^2/v_0^2}v_E + \sqrt{\pi}v_0\left[\text{Erf}\left(\frac{v_{\min}+v_E}{v_0}\right) - \text{Erf}\left(\frac{v_{\min}-v_E}{v_0}\right)\right]\right) \qquad (2.11)\\
\eta_2(v_{\min}) &= \frac{v_0^2\pi}{2v_E K}\left(-2e^{-v_{\text{esc}}^2/v_0^2}(v_{\text{esc}} - v_{\min} + v_E) + \sqrt{\pi}v_0\left[\text{Erf}\left(\frac{v_{\text{esc}}}{v_0}\right) - \text{Erf}\left(\frac{v_{\min}-v_E}{v_0}\right)\right]\right)
\end{aligned}$$

where the subscript corresponds to the case number. Note that the two cases converge to the same value for $v_{\min} = v_{\text{esc}} - v_E$.

The SHM does not reproduce the features of the VDFs inferred by DM-only simulations, in particular when it comes to the high-velocity tail of the distribution [137, 132, 138, 32, 139], although it is in better alignment with VDFs resulting from simulations that include baryonic physics [133, 140–144] (see detailed discussion in §2.2.3). In general, it is safe to say that the SHM does not provide a realistic description of the DM distribution in the Galactic halo, thus motivating the discussion of alternative models for the DM VDF in the following subsections.

2.2.2 Tsallis Model. The use of the Tsallis VDF [145] was proposed to describe data from numerical N-body simulations with baryons [146–148]. While the SHM follows the assumption of standard Boltzmann-Gibbs entropy, $S_{BG} = -k\sum p_i \ln p_i$, where p_i is the probability for a particle to be in state i, the Tsallis model results from Tsallis statistics [145], a generalization of the standard definition of entropy via the introduction of the entropic index q,

$$S_q = -k \sum_i p_i^q \ln_q p_i, \tag{2.12}$$

where $\ln_q p = (p^{1-q} - 1)/(1-q)$ is defined as the q-logarithm [149]. By taking the limit $q \to 1$ we recover the standard Boltzmann-Gibbs entropy. The Tsallis VDF is the exact analog of the SHM but in the generalized Tsallis regime, and describes non-extensive systems. With this Tsallis entropy, one arrives at the Tsallis VDF,

$$f_{\mathrm{Tsa}}(\vec{v}) \propto \begin{cases} \left[1 - (1-q)\frac{\vec{v}^2}{v_0^2}\right]^{1/(1-q)} & |\vec{v}| < v_{\mathrm{esc}} \\ 0 & |\vec{v}| \geq v_{\mathrm{esc}}. \end{cases} \tag{2.13}$$

An argument in favor of using the Tsallis model to describe the velocity profile of the DM halo is due to the fact that this distribution has the escape speed already built-in for the $q < 1$ regime, thus the cutoff does not have to be artificially added as in the SHM case. For $q < 1$, v_{esc} is fixed by q and v_0 through the relation $v_{\mathrm{esc}}^2 = v_0^2/(1-q)$, but for $q > 1$ the escape speed is an independent parameter and still has to be added manually. By examining the velocity distributions inferred by simulations [133], we observe that the high-speed tails exhibit a steeper fall-off and a smoother transition to zero compared to the abrupt fall-off of the SHM VDF. This is a feature that has been associated with relaxed, collisionless structures and is a key characteristic of the Tsallis VDF [150, 149, 151].

The standard parameter choices of $v_0 = 220$ km/s and $v_{\mathrm{esc}} = 544$ km/s correspond to $q = 0.836$, and our suggestions for $v_0 = 228.6$ km/s and $v_{\mathrm{esc}} = 528$ km/s lead to $q = 0.813$. Ref. [148] fits the Tsallis model to a simulation using the RAMSES code [152] with $R_0 = 8.0$ kpc and yields $q = 0.773$ and $v_0 = 267.2$ km/s, corresponding to $v_{\mathrm{esc}} = 560.8$ km/s; we note that these values are well within the error margins for the standard parameters.

2.2.3 Empirical Models.

Cosmological simulations have been instrumental in shaping our understanding of physical processes that one cannot directly observe, such as the non-linear evolution and formation of cosmological structures. A detailed overview of the relevant developments in numerical cosmological simulations can be found in ref. [153]. In this section, we briefly review how cosmological simulations are constructed and their applications to deriving the DM VDF.

Cosmological simulations are broadly divided into two categories: N-body methods, where simulation codes are employed to describe the dynamics of pure collisionless dark matter, and the full hydrodynamical approach where numerical techniques are implemented to study the behavior of the DM component in the presence of baryons. Both classes of simulations trace the phase-space density evolution of the DM fluid, facilitating the extraction of a local VDF associated with each cosmological setup. As revealed by several studies [137, 132, 138, 32, 139] that used data from DM-only simulations, the general trend followed by the associated local VDFs translates into a considerable deviation from the SHM, with the simulation distributions exhibiting a suppressed peak compared to the shape of the truncated Maxwellian and a surplus of particles at the high-speed tail.

Although a layer of appreciable complexity is added to the simulations when incorporating baryonic processes, this step is crucial for replicating realistic conditions in the simulated cosmological environments, and indispensable in order to make robust predictions. Ref. [135] provides a comprehensive review of several analyses [133, 140–144] that drew data from various hydrodynamical simulations. The different design of these simulations can lead to large variations in their final products, including discrepancies in the respective local speed distributions inferred from each simulation, as well as a halo-to-halo scatter concerning the local speed distributions within the same simulation suite. Despite their individual differences, the simulations that include baryonic effects shift the peak of the velocity distributions to higher speeds and, in most cases, show a better convergence with the standard Maxwellian distribution, compared to their DM-only counterparts. Nevertheless, an exact shape for the DM VDF has yet to be captured, and more higher-resolution simulations with an accurate implementation of baryonic physics are required for a universal agreement to be established.

There are several empirical approaches to the DM halo velocity profile derived from various cosmological simulations [154–156]. For our purposes, we will be focusing on the empirical model of refs. [157, 158] based on the DM-only simulation packages Rhapsody [159] and Bolshoi [160]. Previous work has investigated the sensitivity of DM-electron scattering on the DM velocity profile using empirical models derived from the IllustrisTNG simulations [156]. Our work is complementary given that we consider a different set of halo models. In the Galactic rest frame, the empirical halo velocity distribution is given by

$$f_{\mathrm{emp}}(\vec{v}) \propto \begin{cases} e^{-|\vec{v}|/v_0} \left(v_{\mathrm{esc}}^2 - |\vec{v}|^2\right)^p , & |\vec{v}| < v_{\mathrm{esc}} \\ 0, & |\vec{v}| \geq v_{\mathrm{esc}}, \end{cases} \tag{2.14}$$

where the circular speed v_0 and the power p are allowed to vary.

This function is composed out of two terms: an exponential term, that accounts for the anisotropy in the halo's velocity dispersion, and a cutoff term that regulates the number of particles that are bound to the Galactic potential. After fitting each simulated halo with the Navarro-Frenk-White (NFW) density profile, the authors argue that the dominant theoretical uncertainty on the VDF —and correspondingly the scattering event rate— can be traced to the term r/r_s in the NFW profile, *i.e.* the ratio of the radial position where the VDF is measured to the scale radius of the halos' density profile. This quantity points directly to the VDF's connection to the gravitational potential, and ultimately determines the shape of the VDF that exhibits a broader peak and steeper tail, in contrast to the SHM.

Ref. [140] studies the effects of baryonic feedback on the local DM VDF, comparing the resulting distributions extracted from halos in the Eris [161] and ErisDark simulations. Both are well fitted by the empirical distribution in eq. 2.14, while the best-fit parameters are $(v_0, p) = (330$ km/s, 2.7) for Eris, and (100 km/s, 1.5) for its DM-only counterpart. We use $p = 1.5$ for our fiducial model.

2.2.4 Debris Flows from Observational Data.

Observational missions allow us to use stars to trace the evolution and distribution of DM structures in the Milky Way halo. In ref. [30] the authors suggest that an empirical velocity distribution for the DM can be determined through the study of metal-poor stars in the solar vicinity. After testing the correlation between the stellar and the DM distributions using the Eris hydrodynamic simulation [161], they extrapolated this correspondence to infer the VDF for the virialized DM component using SDSS data [162]. The resulting distribution exhibits differences when contrasted with the SHM, with notably the anisotropic behavior of the metal-poor stellar distribution. The correlation between the stellar and DM kinematic distributions demonstrated in [30] prompted the reconstruction of the local velocity distribution associated with the smooth DM component in [163], with the use of metal-poor stellar populations from the RAVE [164]-TGAS [165] catalog.

But no VDF can be complete unless it accounts for the features associated with DM substructure. The study of a combined SDSS [166]-*Gaia* DR2 [167] sample of accreted stars in [31] indicates that a non-negligible fraction of the DM in the halo could be comprised of debris flow, kinematic substructure that consists of many streams or other kinematic features resulting from the debris of orbiting satellites that dissolve. This would only hold true provided that the selected stars adequately trace the DM component. Once this anisotropic stellar population is included in the analysis, the resulting velocity distribution deviates from the SHM prediction. Earlier works [168, 169] have studied the formation and emergence of this velocity phase-space substructure in N-body Via Lactea II (VL2) simulations [170, 171], where the debris flow was identified as spatially-homogeneous material that accumulated from tidally-stripped luminous satellites that fell into our Galaxy. A detailed discussion of the effects of debris flow on the DD observables in the context of DM-nuclear scattering can be found in [172]. We used the results from refs. [31, 173] to simulate the debris flow component of the DM VDF. We find that the addition of this substructure component has a subdominant effect in DM-electron scattering compared to varying the astrophysical parameters of the halo model. The reason for this is twofold: the debris flow is a sub-component of the total distribution, and it contributes mostly at low velocities. Therefore, we do not discuss the effect of debris flows in detail. Nevertheless, the sensitivity of DM-electron scattering to the DM velocity distribution can be exploited to provide information about the underlying DM substructure; the effects of different types of DM substructure, including debris flows and stellar streams, are explored in the context of DM-electron scattering in [174].

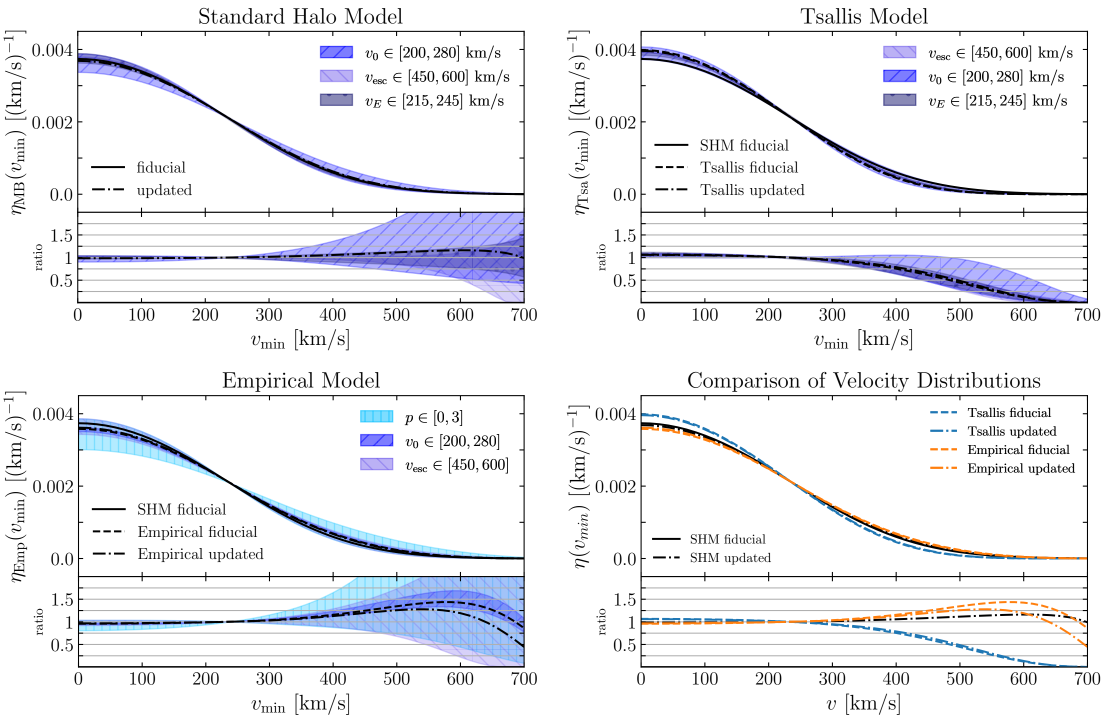

Figure 1. Integrated $\eta(v_{\rm min})$, as defined in eq. 2.4, for the three velocity distributions varied over their parameters. In the bottom, right panel, we show a comparison between the three models at their fiducial values. The black solid line corresponds to the SHM, while the dashed lines represent the Tsallis and empirical distributions, all evaluated at their fiducial parameters. The dash-dotted curves in each panel result from evaluating each model at their updated parameters. When varying over one parameter, the remaining parameters are kept fixed to their fiducial values.

2.3 Astrophysical Parameters

The main astrophysical quantities involved in the calculation of the DM-electron scattering recoil spectrum are the local DM density $\rho_{\rm DM}$, the circular velocity v_0, the escape velocity $v_{\rm esc}$, and the Earth velocity v_E. Here we review how these parameters are measured, and summarize the corresponding sets of measurements provided by currently ongoing experiments. We recommend the use of parameter values from these updated measurements.

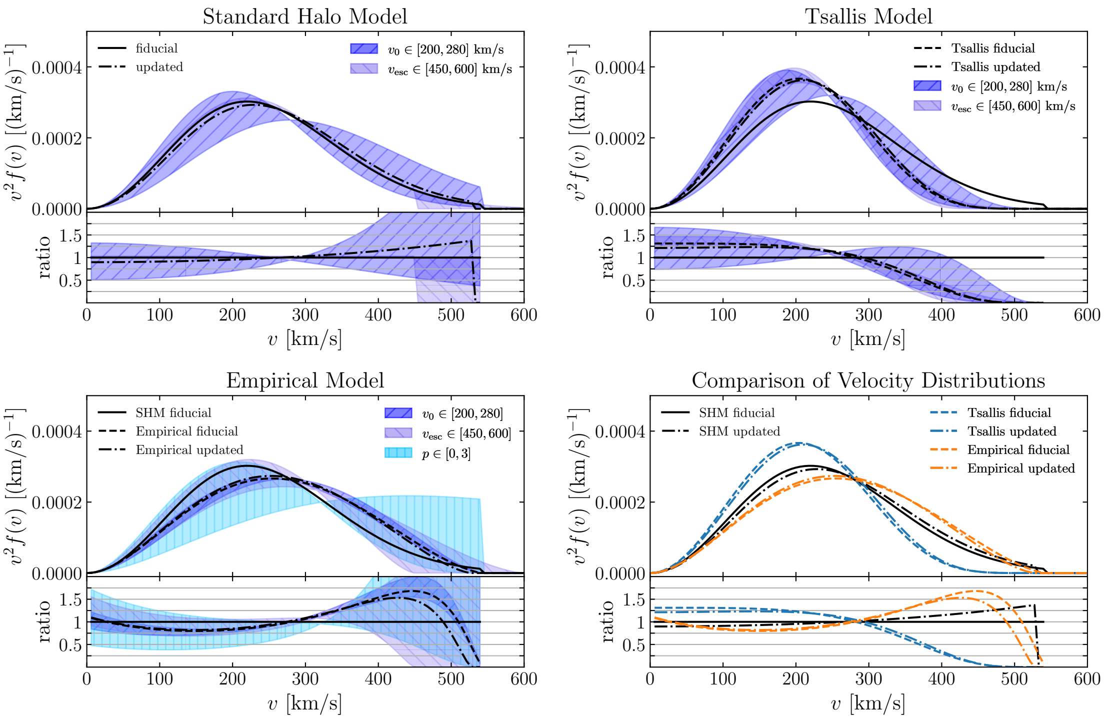

Figure 2. $v^2 f(v)$ for the three velocity distributions varied over their parameters. The black solid line corresponds to the SHM, while the dashed lines represent the Tsallis and empirical distributions, all evaluated at their fiducial parameters. The dash-dotted curves in each panel result from evaluating each model at their updated parameters. The panel on the bottom right corner shows the comparison among the three models. When varying over one parameter, the remaining parameters are set to their fiducial values.

2.3.1 Local Dark Matter Density. The local DM density, $\rho_{\rm DM}$, appears as an overall scaling for the DM scattering rate. The value of $\rho_{\rm DM}$ can be measured via both local [175–181] and global [182–185] methods that offer complementary information about the galactic structure, albeit employing independent techniques (see ref. [186] for a thorough review on the subject, as well as an extensive list of the relevant measurements for the $\rho_{\rm DM}$ parameter).

Local measurements utilize the vertical —in the direction perpendicular to the plane of the Milky Way disk— motions of stellar tracers, located within a small volume surrounding the solar circle, to probe the gravitational potential of the Galaxy. To isolate the contribution of the DM component to the total Galactic potential, substantial modeling is required to assess how baryonic matter is distributed within the Galactic disk. The latter undertaking poses one of the greatest challenges in determining the local DM density in this way. Considering that distinct populations of stars can result in different estimates for the local density, caution should be exercised also when choosing a representative stellar sample [186, 187].

Global measurements rely on a set of dynamical observables to fit parametrized models of the Milky Way. Specifying the model parameters in this fashion, among which the local DM density, posits spherical symmetry for the shape of the Galactic halo, notwithstanding potential departures from sphericity have been shown to give rise to systematic errors in the determination of $\rho_{\rm DM}$ [188–190].

Local-type probes have been gaining ground lately with the advent of high-precision astrometric measurements spearheaded by the *Gaia* satellite. Recently, refs. [187, 191] analyzed stellar data from the *Gaia* DR2 catalog and reported results over the interval (0.4 - 1.5) GeV/cm^3, while according to ref. [192] studies relying on global methods reported values that vary in the range (0.2 - 0.6) GeV/cm^3. Predating *Gaia's* second data release, ref. [193] analyzed SDSS-SEGUE G-dwarf stellar data and reported the value of $0.46^{+0.07}_{-0.09}$GeV/cm^3 for $\rho_{\rm DM}$. This is the value we propose to the experimental collaborations for replacing the value of $\rho_{\rm DM} = 0.4$ GeV/cm^3, that has been the standard suggestion by the PDG [194] and has been in widespread use so far.

2.3.2 Circular Velocity. The rotation curve of the Milky Way $v_c(R)$ specifies how the orbital velocities of the stars and gas vary as a function of distance R from the Galactic center, and consequently reflects how matter is distributed in the Galaxy. For an axisymmetric gravitational potential Φ, the rotation curve is defined as $v_c(R) \equiv R^2 \frac{\partial \Phi}{\partial R}|_{z=0}$, where z corresponds to the height above the Galactic disk plane. We define the circular velocity at the solar Galactocentric distance R_0 as $v_0 \equiv v_c(R_0)$.

There are two broad categories of methods devoted to the determination of the local circular velocity: methods that are independent of R_0 and methods that rely on measurements of R_0. The first category sidesteps the complications related to the measurement of the Galactocentric radius and entails direct probes of the local radial force. Examples of this method involve measurements of the GD-1 stellar stream that yield $v_0 = 221^{+16}_{-20}$ [195], as well as the determination of the Oort constants from the analysis of *Hipparchos* data in [196] that lead to a value consistent with the established IAU recommendation of 220 km/s [197]. Data taken from the Apache Point Observatory Galactic Evolution Experiment (APOGEE) yields a local circular velocity at $v_0 = 218 \pm 6$ [198], without any assumptions about the relation between v_0 and the solar motion. However, this method is limited by the accuracy of the respective data sets and can be improved with increased statistics.

The second category relies on measurements of R_0 and, in principle, inherits the associated uncertainties. However, R_0 is increasingly well-measured (see *e.g.* [199] and references therein), and therefore the values of v_0 derived from the aforementioned method have progressively smaller uncertainties. Given a fixed value for R_0, one can then infer a value for v_0. For example, one can measure the Sun's motion with respect to a fixed reference point, relative to the Milky Way's center. The most prominent point of reference to date is Sagittarius $A^{\star}$, the massive black hole radio source at the center of the Galaxy. The apparent motion of Sagittarius $A^\star$ in the galactic plane is primarily influenced by the effects of the solar orbit around the Galactic center [200]. This observation can be translated into a constraint for the angular motion of the Sun, $\Omega_0 = (v_0 + V_\odot)/R_0$, where $V_\odot$ corresponds to the component of the solar peculiar motion with respect to the Local Standard of Rest (LSR) in the direction of Galactic rotation, a quantity whose measurement introduces another source of uncertainty.[3] For $R_0 = (8.0 \pm 0.5)$ kpc [203], one obtains $v_0 = 241 \pm 17$ km/sec from the motion of Sagittarius $A^\star$ [204].

Ref. [205] studied motions of stars orbiting Sagittarius $A^\star$ and measured the distance from the Sun to the Galactic center to be $R_0 = 8.28 \pm 0.33$ kpc. Ref. [206] employed very long baseline interferometry techniques to obtain parallax and proper motion data of masers and found a consistent value at $R_0 = 8.34 \pm 0.16$ kpc. More recently, ref. [207] derived the Galactic rotation curve by relying on the available 6-d phase-space information on a sample of red giants at Galactocentric radii in the range $5 \lesssim \mathrm{R} \lesssim 25$ kpc, combining data from the APOGEE DR14 [208], *Gaia* DR2 [167], 2MASS [209], and WISE [210] surveys, and employing the Jeans equation to relate the circular velocity to the number density, as well as the radial and transverse velocity dispersions of the selected stellar tracers. Following the analysis in [211], they precisely determined the distances to the stellar tracers under study, bringing the systematic uncertainties for their estimate of v_0 down to the $(2 - 5)\%$ level. Resorting to their modeling function for the circular velocity curve, $v_0(R) = (229.0 \pm 0.2)\mathrm{km/s} - (1.7 \pm 0.1)\mathrm{km/s/kpc}(R - R_0)$, we find that for a

[3] The $V_\odot$ components are challenging to determine due to the dependence of their associated asymmetric drift on the velocity dispersion of the stellar sample invoked to measure the solar peculiar motion vector $\vec{v}_\odot$ [201, 202]. The authors in [202], by studying stellar data from the *Hipparchos* catalogue, inferred the stellar velocity distributions based on a model that takes into account the Galaxy's chemodynamical evolution, and determined the value of $v_\odot$ at (11.1,12.24,7.25) km/s.

distance of 8.34±0.16 kpc the resulting circular velocity equals (228.6±0.34) km/s.[4] This is our recommendation to the experimental collaborations for substituting the canonical IAU-reported value of 220 km/s [197].

We end this sub-section with a brief discussion about the correlation between the astrophysical parameters R_0 and v_0 [213, 214, 206]. Such a correlation further implies a correlation between v_0 and $\rho_{\rm DM}$ [33], as the latter quantity is a function of R_0. Ref. [206] suggests that the two parameters are no longer strongly correlated and constrains the angular solar motion Ω_0 with an accuracy of ±1.4% at 30.57 ± 0.43 km/s/kpc for $R_0 = 8.34 \pm 0.16$ kpc. However, assuming that such a correlation between R_0 and v_0 persists, the spatial dependence of the DM density $\rho_{\rm DM}$ is contingent upon the particular choice of the DM density profile. For an NFW profile, this implies that if we fix Ω_0 and R_0 at the aforementioned values, allowing v_0 to vary by ±30 km/s/kpc would alter the DM density by $^{-17}_{+22}$%. This change in the DM density then proportionally affects the differential scattering rate, as can be seen in eq. 2.1. By referring to table 2, the reader can get a sense of how changes in v_0 impact $\rho_{\rm DM}$, and by extension the scattering rate.

2.3.3 Escape Velocity. The Galactic escape velocity sets the threshold beyond which a test particle is no longer bound to the Galactic potential at the solar location, $\Phi(R_0)$, and is defined as $v_{\rm esc} = \sqrt{-2\Phi(R_0)}$. One approach to estimating $v_{\rm esc}$ is built upon sampling high-velocity halo stars and postulating a power law ansatz for the tail of their velocity distribution, truncated at the escape speed [215]; this approach is insensitive to the shape of the rotation curve. The distribution function characterizing these stars is assumed to be isotropic and

[4]Note that the GRAVITY collaboration recently constrained the value of the Galactocentric radius with great precision to $R_0 = 8.249 \pm 0.009(\text{stat.}) \pm 0.045(\text{syst.})$ kpc [212], and their result yields a v_0 value consistent with our recommendation.

in steady-state. Another approach that does not rely on the above hypotheses, uses kinematic, photometric, and theoretical constraints to build a dynamical mass model of the Milky Way, and estimates $v_{\rm esc}$ through the resulting Galactic potential [185].

The RAdial Velocity Experiment (RAVE) team employs the former methodology by studying spectroscopic stellar data, and performing simulations which assess the validity of the ansätze used to model the distribution of the stellar velocities. Their measurement of $v_{\rm esc} = 544^{+64}_{-46}$ km/s at 90% confidence level (C.L.) [216] is currently the standard value for DM DD searches; a more recent estimate by RAVE finds $v_{\rm esc} = 533^{+54}_{-41}$ at 90% CL [217]. Note that the dark halo model implemented by the RAVE collaboration leads to correlations among $v_{\rm esc}$ and the other local DM halo parameters [217]; therefore, one must take care to use consistent halo parameters when adopting the reported value of $v_{\rm esc}$ [218], and not treat $v_{\rm esc}$ as an independent quantity.

The value of $v_{\rm esc}$ can also be extracted from the velocities of halo stars, and this has become a reliable method thanks to the improvements in the astrometry frontier. These extractions use a simple model for the tail of the velocity distribution of halo stars at a fixed radius, based on a truncated power law [215]. A recent analysis noted that the power-law scaling of the high-velocity tail of the stellar sample is contingent upon features of the stellar halo [219], and concluded that there is a smaller prior on the scaling compared to previous analyses [216, 217, 220]. This new prior is appropriate for strongly eccentric orbits in the solar vicinity, and when applied to data from *Gaia* DR2, results in $v_{\rm esc} = 528^{+24}_{-25}$ km/s [219]. We use this value of $v_{\rm esc}$ for our updated analysis.

2.3.4 Earth Velocity.

The final parameter we will discuss in this section is the Galactic velocity of the Earth, v_E. This parameter enters DM DD calculations as one must calculate the rate in the reference frame of the Earth. Therefore, the VDF that appears in eq. 2.4 should be evaluated at the detector's frame; this is achieved by performing a Galilean boost to the galactic-frame velocity distribution, $f_G(\vec{v})$, in the following manner

$$f_E(\vec{v}) = f_G(\vec{v} + \vec{v}_E(t)), \tag{2.15}$$

where the subscripts G, E indicate the Galactic- and Earth-frame, respectively.

The Earth's velocity, $\vec{v}_E(t) = \vec{v}_{LSR} + \vec{v}_\odot + \vec{v}_E^{orb}(t)$ describes the motion of the Earth with respect to the galactic frame and is comprised out of three components: $\vec{v}_{LSR} = (0, v_0, 0)$ that denotes the motion of the LSR with v_0 the circular velocity at the Solar radius (see §2.3.2), $\vec{v}_\odot = (U_\odot, V_\odot, W_\odot)$ that corresponds to the Sun's peculiar motion velocity vector with respect to the LSR, and $\vec{v}_E^{orb}(t)$ for the Earth's orbital motion around the Sun, defined as $\vec{v}_E^{orb}(t) = v_E^{orb}\,[\hat{e_1}\mathrm{sin}\lambda(\mathrm{t}) - \hat{e_2}\mathrm{cos}\lambda(\mathrm{t})]$ [221] with $v_E^{orb} = 29.8$ km/s, while $\lambda(\mathrm{t})$ is the solar ecliptic longitude, and $\hat{e_1} = (-0.0670, 0.4927, 0.8676)$, $\hat{e_2} = (-0.9931, -0.1170, 0.01032)$ are the two orthogonal unit vectors defining the Earth's plane at the time of the spring equinox and summer solstice, respectively, expressed here in galactic coordinates. In this work, we adopt a value of $\bar{v}_E = 232$ km/s with a modulation of ± 15 km/s over the course of the year [222, 223]. This time-dependent revolution of the Earth around the Sun leads to an annual modulation of the scattering event rate, an effect that represents one of the most striking signatures in DM detection and provides a powerful handle in differentiating between signal and background [19].

2.3.5 Summary of Astrophysical Parameters.

In figs. 1 and 2, we show the effects of varying the astrophysical parameters on the η and $v^2 f(v)$

functions, respectively, for the different halo models discussed in this section. We see that the choice of astrophysical parameters has a significant effect on the shape of η, with a mild variation among the halo models. As we will see in the next section, this effect has substantial consequences on the predicted rates for DM-electron scattering. Therefore, we advocate in favor of updating the benchmark values for the SHM parameters that appear throughout the bibliography of DM searches, and recommend a new set of values that can be adopted by the experimental groups that study the DM-electron scattering interactions. Table 1 displays all the relevant galactic parameters used in our analysis, accompanied by the values broadly used in the literature to date (*current*), as well as more recent determinations of the parameters in question (*suggested*). In what follows, we quantify the effects that the variations of the astrophysical parameters have on the calculations of DM-electron scattering.

	current	suggested
v_0 [km/s]	220^{+60}_{-20} [197]	228.6 ± 0.34 [207]
$v_{\rm esc}$ [km/s]	544^{+56}_{-94} [216]	528^{+24}_{-25} [219]
$\rho_{\rm DM}$ [GeV/cm^3]	0.4 [194]	$0.46^{+0.07}_{-0.09}$ [193]
v_E [km/s]	232 ± 15 [222]	232 ± 15 [222]
R_0 [kpc]	8.0 ± 0.5 [203]	8.34 ± 0.16 [206]

Table 1. Measurements for the local circular speed v_0, escape speed $v_{\rm esc}$, local DM density $\rho_{\rm DM}$, Galactic Earth velocity v_E, and solar radius R_0. The central values in the middle column correspond to the canonical values for the parameters, in use by experimental groups so far; the central values in the last column are our recommendations to the experimental collaborations for future use.

2.4 Results

In this section, we present the results for the rate and cross-section sensitivities for DM-electron scattering, from varying the SHM over its associated parameters. We present the detailed results for the Tsallis and empirical models in appendices A.1 and A.2, respectively, while showing comparisons among all the models considered in this analysis throughout the main text.

Standard Halo Model (m_χ=10 MeV)

N_e	1		2		3		4	
F_{DM}	1	$(\alpha m_e/q)^2$	1	$(\alpha m_e/q)^2$	1	$(\alpha m_e/q)^2$	1	$(\alpha m_e/q)^2$
Fiducial	7.8×10^4	3.6×10^4	7.9×10^4	1.3×10^4	1.5×10^4	9.9×10^2	2.3×10^3	67
Updated	9.2×10^4	4.3×10^4	9.6×10^4	1.6×10^4	1.9×10^4	1.3×10^3	3.0×10^3	86
rel. diff.	0.17	0.20	0.22	0.25	0.28	0.30	0.30	0.28
$v_{0,min}$	7.5×10^4	3.2×10^4	6.6×10^4	9.9×10^3	1.0×10^4	6.2×10^2	1.3×10^3	35
$v_{0,max}$	8.7×10^4	4.7×10^4	1.1×10^5	2.2×10^4	3.0×10^4	2.3×10^3	6.0×10^3	2.0×10^2
rel. diff.	0.15	0.41	0.58	0.91	1.3	1.7	2.1	2.5
$v_{esc,min}$	7.7×10^4	3.4×10^4	7.4×10^4	1.1×10^4	1.2×10^4	6.6×10^2	1.2×10^3	25
$v_{esc,max}$	7.9×10^4	3.7×10^4	8.0×10^4	1.3×10^4	1.5×10^4	1.1×10^3	2.6×10^3	85
rel. diff.	0.015	0.057	0.074	0.16	0.27	0.43	0.60	0.89
$v_{E,min}$	7.5×10^4	3.3×10^4	7.1×10^4	1.1×10^4	1.2×10^4	7.9×10^2	1.7×10^3	48
$v_{E,max}$	8.1×10^4	3.8×10^4	8.6×10^4	1.4×10^4	1.7×10^4	1.2×10^3	2.8×10^3	85
rel. diff.	0.080	0.14	0.19	0.24	0.32	0.38	0.45	0.55

0.0 0.1 0.5 1.0

relative difference

Standard Halo Model (m_χ=1000 MeV)

N_e	1		2		3		4	
F_{DM}	1	$(\alpha m_e/q)^2$	1	$(\alpha m_e/q)^2$	1	$(\alpha m_e/q)^2$	1	$(\alpha m_e/q)^2$
Fiducial	1.1×10^3	5.0×10^2	1.7×10^3	2.7×10^2	5.9×10^2	39	1.9×10^2	5.9
Updated	1.3×10^3	5.9×10^2	2.0×10^3	3.3×10^2	7.2×10^2	49	2.3×10^2	7.5
rel. diff.	0.15	0.18	0.18	0.21	0.22	0.25	0.25	0.28
$v_{0,min}$	1.1×10^3	4.6×10^2	1.6×10^3	2.3×10^2	4.9×10^2	29	1.4×10^2	4.0
$v_{0,max}$	1.1×10^3	5.9×10^2	2.0×10^3	3.8×10^2	8.5×10^2	68	3.2×10^2	12
rel. diff.	-0.00033	0.26	0.21	0.54	0.60	0.98	0.93	1.4
$v_{esc,min}$	1.1×10^3	4.8×10^2	1.7×10^3	2.5×10^2	5.5×10^2	33	1.6×10^2	4.3
$v_{esc,max}$	1.1×10^3	5.0×10^2	1.7×10^3	2.7×10^2	6.0×10^2	40.	1.9×10^2	6.3
rel. diff.	-0.0017	0.036	0.024	0.087	0.087	0.18	0.17	0.34
$v_{E,min}$	1.1×10^3	4.7×10^2	1.6×10^3	2.4×10^2	5.3×10^2	34	1.6×10^2	4.8
$v_{E,max}$	1.1×10^3	5.2×10^2	1.8×10^3	2.9×10^2	6.4×10^2	44	2.1×10^2	6.8
rel. diff.	0.016	0.095	0.092	0.17	0.18	0.26	0.24	0.34

0.0 0.1 0.5 1.0

relative difference

Table 2. Expected number of events in 1 kg-year for various values of the SHM parameters $v_0, v_{\rm esc}$, and v_E, as well as the relative difference between the minimum and maximum values for each parameter, for a given N_e bin and DM form factor $F_{\rm DM}$. The top panel displays the results for $m_\chi = 10$ MeV, and the bottom panel for $m_\chi = 1$ GeV. The color scale indicates the size of the relative difference, with white (red) being the smallest (largest) relative difference.

2.4.1 Standard Halo Model Rate and Cross Section.

We summarize the effects of varying over the parameters of the SHM on the predicted number of events in table 2, fixing the exposure at 1 kg-year and assuming a cross section of $\overline{\sigma}_e = 10^{-37}$ cm^2. We calculate the number of events for each N_e bin up to 4 (for the DM form factors $F_{\rm DM} = 1$ and $F_{\rm DM} = (\alpha m_e/q)^2$) for each parameter combination, where e.g., $v_{0,\rm min}$ refers to v_0 at its minimum value with the other parameters held constant at their fiducial values. In each bin and for each parameter, the relative difference is defined by taking the difference between the rates for the maximum and minimum values of the underlying parameter, and dividing it by the fiducial rate, i.e.,

$$\text{rel. diff.} = \frac{\text{Rate}_{\rm max} - \text{Rate}_{\rm min}}{\text{Rate}_{\rm fid}}. \tag{2.16}$$

From this table we see that v_0 gives the largest variance in the rate for these 4 bins for $m_\chi = 10$ (1000) MeV, ranging from $\sim$ 15% (0.03%) for $N_e = 1$ and $F_{\rm DM} = 1$ to $\sim$ 250% (140%) for $N_e = 4$ and $F_{\rm DM} = (\alpha m_e/q)^2$. The larger differences at low masses are to be expected, as low mass DM is more sensitive to the high-speed tail of the velocity distribution. Similar tables that summarize how the count rates and cross sections are affected due to the variation of the underlying halo model for the Tsallis and empirical distributions can be found in appendices A.1 and A.2, respectively.

In fig. 3, under the assumption of the SHM for the DM velocity profile, we present the spectrum of events as a function of the electron energy E_e, for two DM form factors ($F_{\rm DM} = 1$ and $F_{\rm DM} = (\alpha m_e/q)^2$) and two candidate masses ($m_\chi = 10$ MeV and 1 GeV). As expected, increasing the ionization threshold N_e leads to a rate drop-off. However, for the lower-mass candidate at the high-energy regime, this fall-off is much more pronounced; lowering v_{esc} significantly affects the rate, since for more energetic transitions to be realized, DM particles need to be moving much faster. Thus by decreasing v_{esc}, we effectively constrain the number of particles in the halo that are available to scatter. In all other cases we see that v_0 is leading the changes to the event rate, as is the case for the SHM's associated inverse mean speed in fig. 1. Analogous plots that show how variations in the halo-model parameters impact the rates for the Tsallis and empirical distributions can be found in the appendices A.1 and A.2, respectively.

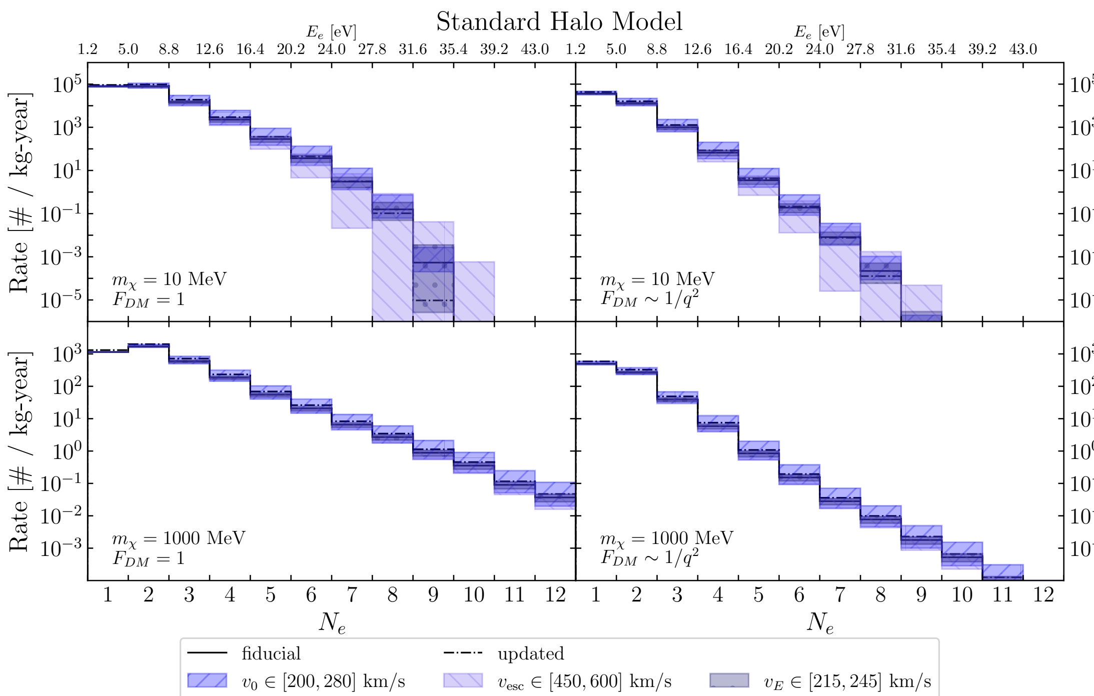

Figure 3. Rate spectra for the SHM at 1 kg-year exposure and $\overline{\sigma}_e = 10^{-37}$ cm^2 for a range of halo parameters, as a function of the number of observed electrons, N_e, and electron energy E_e. The rate for the SHM with fiducial halo parameters is given by the black solid line, while the rate for the updated halo parameters is given by the black dash-dotted line. The top (bottom) panels show the rate for $m_\chi = 10$ MeV ($m_\chi = 1$ GeV), and the left (right) panels for $F_{\text{DM}} = 1$ ($F_{\text{DM}} = (\alpha m_e/q)^2$).

In fig. 4, we show the projected sensitivity at 95% C.L. ($\sim$3 events) to the DM-electron scattering cross section, $\overline{\sigma}_e$, as a function of the DM mass, m_χ, setting the exposure at 1 kg-year and assuming zero background events. We present the resulting curves for the first three N_e bins, which correspond to the purple, orange, and green lines, respectively. The color bands around each curve indicate the maximal and minimal differences in $\overline{\sigma}_e$, resulting from the variation of the SHM VDF across its parameters, v_0, $v_{\rm esc}$, and v_E. Specifically, the lower edge of each band results from setting these three velocities at their maximum values, while the upper part corresponds to the minimum values of the velocities' respective ranges. When increasing the DM mass, this DD observable becomes more resilient to changes in the halo parameters, especially for the $N_e = 1$ bin. In the lower end of the mass spectrum, changes in the halo-model parameters can change the lowest detectable mass by up to a factor of ~ 2. The updated parameters for the SHM generally result in an improved reach, primarily driven by the increase in $\rho_{\rm DM}$. Although the SHM is most sensitive to variations in v_0, our recommendation for using more recent measurements shifts the central value of this parameter by only a few percent. In contrast, the updated $\rho_{\rm DM}$ is $\sim$ 15% larger; the effect of this larger value for the density is particularly noticeable at high masses, where the cross-section limits are the least sensitive to variations in the other halo-model parameters. Similar plots that show how the cross section is affected by the variation of the halo model across its associated parameters for the Tsallis and empirical distributions can be found in the appendices A.1 and A.2, respectively.

2.4.2 Comparison Between Halo Models. In fig. 5, we compare the scattering event rates for the three VDFs considered in this work. We note that, as an overall trend, the empirical model tends to result in slightly higher

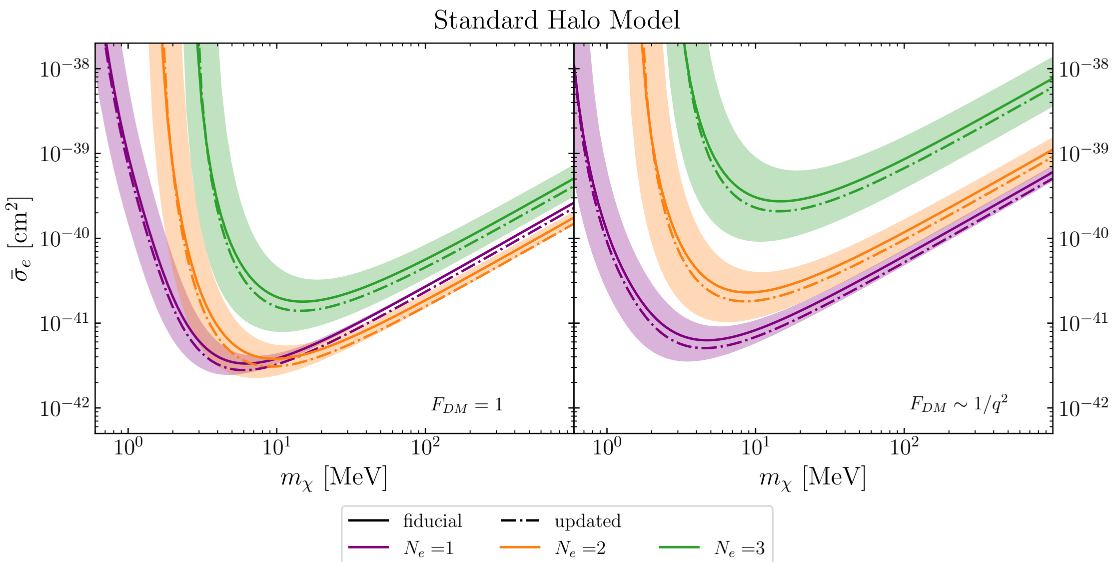

Figure 4. Projected 95% C.L. cross-section reach for the SHM, assuming 1 kg-year exposure and zero background events. The predictions for the $N_e = 1, 2, 3$ bins are given in purple, orange, and green respectively. The solid curves are calculated using the fiducial values for the halo parameters, while the dash-dotted curves are calculated with the updated parameters. The bands denote the range of cross sections resulting from the variation of all the halo parameters within their allowed intervals.

rates than the SHM, while the Tsallis model yields drastically lower rates. This is especially true for the higher N_e bins, where we are more sensitive to the high-speed tails of the VDFs. This trend can be traced back to the corresponding η plots for the models in fig. 1, where for high $v_{\min}$ values, the Tsallis distribution results in a significantly lower η, and by extension to smaller rates.

The qualitative differences in the differential rates, for the three VDFs under study, call for a statistical analysis in pursuit of the minimum exposure at which one can differentiate among the underlying halo models. Note that such an analysis is only feasible if the DM mass and model are known; determining these requires a separate, independent measurement, the details of which are beyond the scope of this work. We proceed by assuming we know the DM mass and model. One can then perform a simple log-likelihood shape test to compare the event rates for the various velocity distributions. Following the procedure outlined in ref. [224], we find that the SHM and Tsallis distributions can be easily distinguished for exposures below a kg-year and DM masses in the range 1 MeV-1 GeV, whereas differentiating between the SHM fiducial and updated models requires much larger exposures, ranging from a few hundred gram-years for $m_\chi \simeq 10$ MeV to above 30 kg-years for $m_\chi \simeq 1$ GeV. These preliminary results motivate a more in-depth statistical analysis of DM-electron scattering data, which we leave for future work.

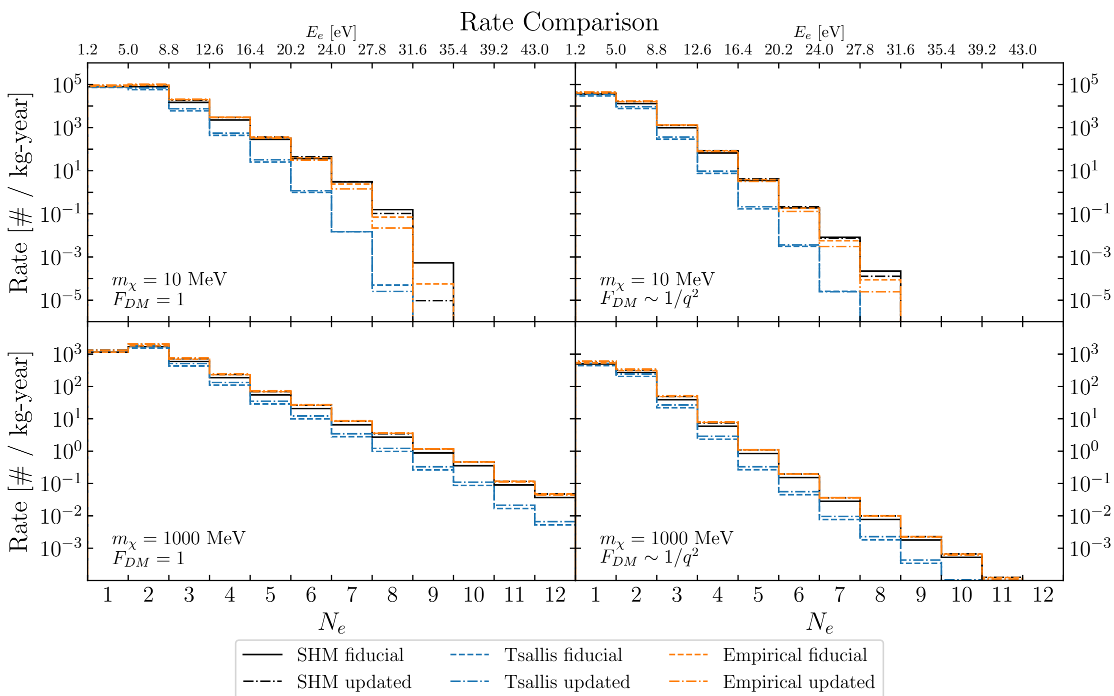

Figure 5. Comparison of the rate spectra for the SHM (black), Tsallis (blue), and empirical (orange) velocity distributions, assuming $\overline{\sigma}_e = 10^{-37}\mathrm{cm}^2$ and 1 kg-year exposure. The solid/dashed (dash-dotted) curves correspond to the rates evaluated at their fiducial (updated) parameters. The top (bottom) panels show the rate for $m_\chi = 10$ MeV ($m_\chi = 1$ GeV), and the left (right) panels for $F_{\mathrm{DM}} = 1$ ($F_{\mathrm{DM}} = (\alpha m_e/q)^2$).

In fig. 6, we compare the cross-section 95% C.L. projections for a kg-year exposure across the three VDFs under consideration. In this figure, the solid lines correspond to the SHM, dashed to the Tsallis model, and dash-dotted to the empirical model. We observe that in all cases, similarly to the rate, the Tsallis model results in a more limited reach, compared to the SHM and empirical model. For the most part, the empirical model exhibits a slightly better reach than the SHM, as confirmed from the first three N_e bins of the rate plots as well. As in the SHM case, the cross section shows increased resilience to the choice of the VDF at higher masses, and especially for the $N_e = 1$ bin. Interestingly, for our choice of parameters, the empirical model closely follows the SHM.

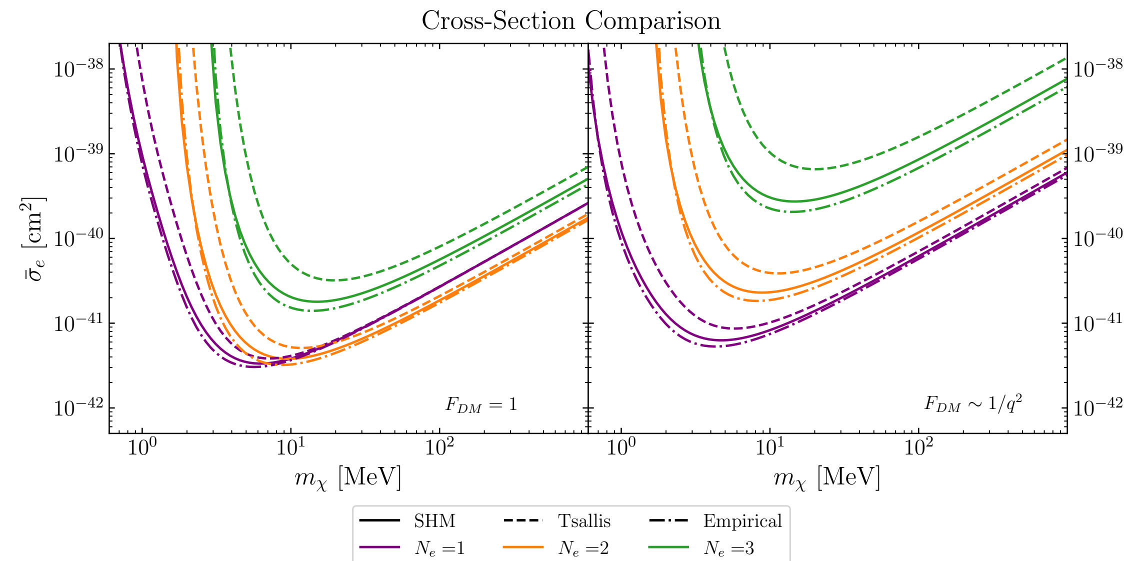

Figure 6. Cross-section comparison between the SHM (solid), Tsallis model (dashed), and empirical model (dash-dotted) for $N_e = 1, 2, 3$ (purple, orange, green). All 95% C.L. curves are computed using the canonical values for the halo parameters ($v_0 = 220$ km/s, $v_{\rm esc} = 544$ km/s, $v_E = 232$ km/s, and $p = 1.5$).

2.4.3 Annual Modulation of the Scattering Rate. Due to the Earth's annual rotation around the Sun, its velocity relative to the Galactic center, v_E, evolves in time, as a result of which the count rate experiences an annual modulation. In this section, we briefly discuss the behavior of this annual modulation for the three considered halo models; a more detailed treatment of the annual modulation of the DM-electron scattering rate under the assumption of the SHM can be found in ref. [120]. The annual modulation of the scattering rate is defined as

$$\text{Modulation}(N_e, t) = \frac{\text{Rate}(N_e, v_E(t)) - \text{Rate}(N_e, \bar{v}_E)}{\text{Rate}(N_e, \bar{v}_E)}, \tag{2.17}$$

where $\bar{v}_E = 232$ km/s is the fiducial average v_E value. The other halo parameters are set to their respective fiducial values.

In fig. 7 we show the annual modulation of the rate as a function of time. The plots in the top row correspond to the resulting modulation for the SHM for the $N_e = 1, 2, 3$ bins. The bottom panels present the comparison among the SHM (black), Tsallis (blue) and empirical (orange) distributions for $N_e = 1$. The modulation is calculated for two candidate masses, $m_\chi = 10$ MeV (solid) and $m_\chi = 1$ GeV (dashed), and two form factors $F_{\text{DM}} = 1$ (right) and $F_{\text{DM}} = (\alpha m_e/q)^2$ (left). As the plots in fig. 3 suggest, varying v_E has a larger effect toward the higher N_e bins, which are in general more susceptible to variations of the halo model, with the effect being more pronounced for the DM form factor proportional to $1/q^2$. These effects manifest themselves in the case of the annual modulation of the rate as well, as it is evident from the high-N_e behavior of the modulation for the SHM, and the resulting modulation for all the models for the $F_{\text{DM}} = (\alpha m_e/q)^2$ form factor. As emphasized earlier, larger DM masses tend to be more robust to changes in the astrophysical parameters, as verified by the lower annual modulation resulting for the $m_\chi = 1$ GeV candidate mass.

Comparing between the three VDFs, we see that the Tsallis model results in the greatest modulation, while the empirical model results in the smallest. This behavior is justified by the fact that the Tsallis velocity distribution is overall more sensitive to changes across its associated parameters, followed by the SHM and the empirical distribution. Since changes in v_E are effectively changes in velocity for the calculation of the inverse mean speed η (see eqn. 2.4), this behavior propagates into the event rates resulting for each model.

2.5 Discussion and Conclusions

In this work, we quantify the dependence of the observables of DM-electron scattering, namely the differential scattering rate and the cross section, on the uncertainties of the underlying DM halo velocity distribution. We consider three halo models: the SHM, the Tsallis model, and an empirical model. We study the effects of varying the astrophysical parameters within each model, and calculate the projected event rates and cross-section bounds. In addition, we give a brief overview of the measurements of the relevant astrophysical parameters and propose updated values for $v_0, v_{\rm esc}$, and $\rho_{\rm DM}$.

Ultimately, we find that the empirical model sets the strongest constraints, while the Tsallis model sets the weakest. When varying the halo models across the relevant astrophysical parameters, we find that v_0 is the most influential parameter in the cases of the SHM and Tsallis distributions, while p is the dominant parameter for the empirical model. For $m_\chi = 10$ (1000) MeV, the variation in v_0 leads to changes in the rate ranging from $\sim 15\%$ (0.03%) for $N_e = 1$ and $F_{\rm DM} = 1$ to $\sim 300\%$ (140%) for $N_e = 4$ and $F_{\rm DM} = (\alpha m_e/q)^2$. In the empirical model, the variation in p leads to changes in the rate ranging from $\sim 5\%$ (1%) for $N_e = 1$ and $F_{\rm DM} = 1$ to $\sim 500\%$ (240%) for $N_e = 4$ and $F_{\rm DM} = (\alpha m_e/q)^2$. Overall, the empirical model varies the most within the allowed intervals for its parameters, while the SHM varies the least. Across all three models we see a pattern according to which, the direct detection observables depend more on our choice of VDF and its associated parameters for the lower DM masses, higher threshold energies (N_e), and $F_{DM} \sim 1/q^2$, while the choice of the VDF has a weaker effect when increasing the DM mass, lowering the ionization threshold N_e and setting $F_{DM} = 1$. For all three models, updating the canonical value of the local DM density with a higher value, leads to a stronger bound on the projected cross section.

The sensitivity of DM-nuclear scattering to astrophysical uncertainties is well-known, and must be taken into account when interpreting the results of the direct detection experiments (see *e.g.* [225]). Our results quantify the sensitivity of DM-*electron* scattering observables to the astrophysical parameters, and highlight the importance of extracting accurate measurements for these parameters, aiming at a consistent interpretation of the relevant experimental efforts. Several proposals account for these astrophysics-driven uncertainties in the case of DM-nuclear scattering, ranging from marginalizing over astrophysical uncertainties [226], to presenting the results in a halo-independent manner [227–232]. We emphasize that similar techniques can be developed and applied in the context of DM-electron scattering interactions and are worthy of a dedicated study.

Once data from ongoing and upcoming DD experiments start flowing in, the emergence of a positive signal would mark the onset of the DM discovery mode. Such a development would necessitate/expand the design of statistically-robust analyses, allowing one to accurately reconstruct the properties of the DM particle, through the study of the available DD data [226, 233]. Once such analyses would be in place, one would be in position to ask how well the DM VDF can be determined, by performing various statistical tests with the potential to pin down the underlying DM halo model. Preliminary analyses along these lines show great promise for DM-electron scattering [234], and this direction warrants further exploration.

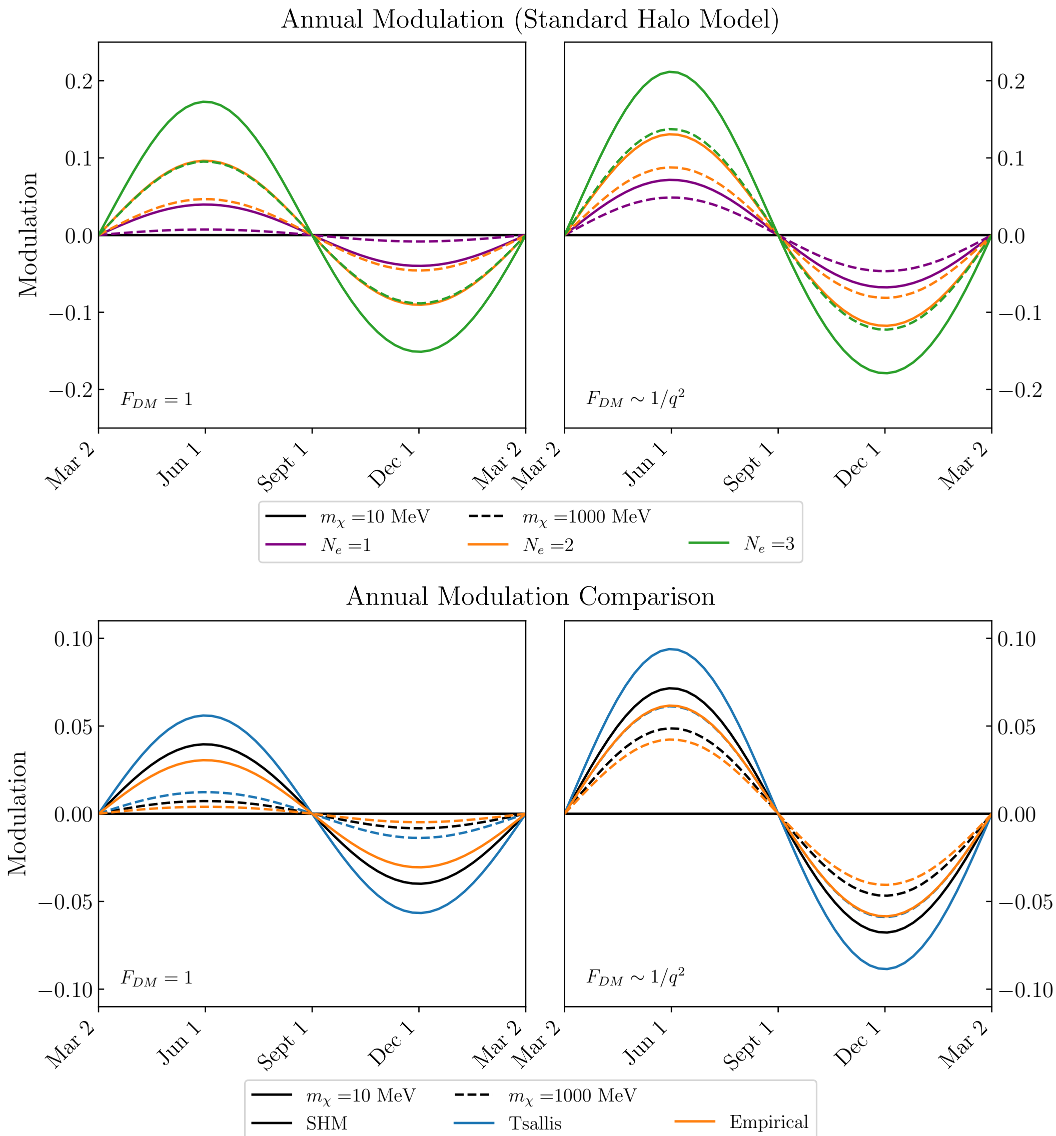

Figure 7. Annual modulation for $F_{\rm DM} = 1$ (left) and $F_{\rm DM} \propto 1/q^2$ (right). The top panels shows the modulation for the SHM for $m_\chi = 10$ MeV (solid), 1 GeV (dashed) and $N_e = 1, 2, 3$ (purple, orange, green). The bottom panels show the modulation comparison among the SHM (black), Tsallis (blue), and empirical (orange) distributions for $N_e = 1$.

CHAPTER III

INTERPLAY OF FREEZE-IN AND FREEZE-OUT: LEPTON-FLAVORED DARK MATTER AND MUON COLLIDERS

From P. Asadi, A. Radick, and T.-T. Yu, “Interplay of freeze-in and freeze-out: Lepton-flavored dark matter and muon colliders,” Phys. Rev. D 110 no. 3, (2024) 035022, arXiv:2312.03826 [hep-ph]

3.1 Lepton-Flavored Dark Matter Model

We start by introducing the model under study in this paper. We augment the SM with a scalar mediator, ϕ, that has the same charges under SM gauge groups as RH charged leptons, and neutral fermion χ,[1]

$$\mathcal{L} \supset -m_\chi \bar{\chi}_\alpha \chi^\alpha - m_\phi^2 |\phi|^2 - \lambda_{i,\alpha} \phi \bar{e}_i \bar{\chi}_\alpha. \tag{3.1}$$

Here i (α) is SM fermion (DM) flavor index, $\bar{e}$ denotes SM charged leptons of RH chirality, χ is the fermionic DM candidate, ϕ is the mediator that has the same charges under SM gauge group as a RH charged lepton, and m_χ (m_ϕ) denotes the shared DM (mediator) mass. While having multiple DM flavors can give rise to interesting physics [108–115], we will consider only one DM flavor as multiple flavors will not affect our collider study.

It should be noted that such setups are studied under other names such as Effective WIMP [235, 236], Fermion Portal DM [237, 238], and colored mediator models [239, 240] as well. Flavored DM model can be considered a more general framework compared to these models since it also includes multiple DM flavor indices. Thus, we use the umbrella term flavored DM for our model, even though having multiple DM flavors, for the most part, does not change our study. We

[1] With the same field content we could also have ϕLL and $H\bar{\chi}L$ terms that could potentially destabilize DM. We postulate a $\mathbb{Z}_2$ parity acting on ϕ, χ, and $\bar{\chi}$ that forbids these terms.

should also note that we focus on the case where the neutral particle, χ, is a fermion. We could also consider the scenario in which this DM candidate is scalar and its mediator to SM is a charged heavier fermion.

In the existing studies of such setups (including a recent study of its signal at a MuC [90]), DM is assumed to be a thermal relic, freezing out of the SM bath at some point in the early universe. Nonetheless, DM abundance could also be determined via the freeze-in mechanism [117] instead,[2] where DM never reaches thermal equilibrium with SM. While there exists some studies of flavored DM abundance via UV freeze-in [242] or LHC signatures in this region of the parameter space [243, 244], a proper study of the interplay between the DM freeze-in and its mediator's freeze-out, and their implications for collider searches are still undelivered.

In the upcoming sections, we will study the relic abundance of DM in such a setup more carefully, highlighting an interesting interplay of freeze-in and freeze-out which gives rise to an upper bound on DM mass and interesting signals at future colliders. It should be noted that we are implicitly assuming the reheating temperature in the early universe is above the mediator mass m_ϕ, such that there initially exists an abundance of ϕ in equilibrium with SM, which subsequently freezes out before decaying to DM χ. If the reheat temperature is below ϕ mass, DM is only produced via UV freeze-in [241] and it will not have an upper bound on its mass.

The original flavored DM setups required an artificial introduction of a non-trivial flavor ansatz to suppress dangerous FCNC and LFV. In the freeze-in regime, smallness of the λ Yukawa coupling guarantees an automatic suppression of these

[2]The original freeze-in proposal is now known as IR freeze-in; see Ref. [241] for what is known as UV freeze-in.

processes. We will leave explorations of a natural realization of such small Yukawa couplings in the UV to future works and focus on their phenomenology at colliders in this work.

3.1.1 Relic Abundance.

In this section we go through the relic abundance calculation of our setup. We will show that the interplay between the freeze-in and the freeze-out processes bounds our viable parameter space from all directions. Further details about our calculation of the relic abundance can be found in Appendix B.1; see also Refs. [245, 246] for a similar relic abundance calculation in a quark-flavored DM model.

We start by reasserting that ϕ reaches equilibrium in the early universe, *i.e.* the reheat temperature is higher than the ϕ mass. As a result, we should solve the coupled set of Boltzmann equations governing the abundances. Neglecting Pauli blocking and Bose enhancement, and assuming symmetric particle–anti-particle abundances, we can rewrite the evolution equations for ϕ and χ abundances, as [247, 117]

$$\begin{aligned}\frac{dY_\phi}{dx} =& -\sum_{\mathcal{F}} \frac{m_\phi^3 \langle\sigma v\rangle_{\phi\phi\to\mathcal{F}}}{H(m_\phi)x^2}\left[Y_\phi^2 - Y_{\phi,\mathrm{EQ}}^2\right] \\ & -\sum_{\ell} \frac{x^3}{H(m_\phi)}\frac{g_\phi \Gamma_{\phi\to\ell\chi}}{2\pi^2} K_1(x)\left[\frac{Y_\phi}{Y_{\phi,\mathrm{EQ}}} - \frac{Y_\chi}{Y_{\chi,\mathrm{EQ}}}\right], \end{aligned} \tag{3.2}$$

$$\frac{dY_\chi}{dx} = \sum_{\ell} \frac{x^3}{H(m_\phi)}\frac{g_\phi \Gamma_{\phi\to\ell\chi}}{2\pi^2} K_1(x)\left[\frac{Y_\phi}{Y_{\phi,\mathrm{EQ}}} - \frac{Y_\chi}{Y_{\chi,\mathrm{EQ}}}\right], \tag{3.3}$$

where $H(m_\phi) = 1.66\sqrt{g_*^\rho} m_\phi^2/M_{\mathrm{Pl}}$ is the Hubble constant at m_ϕ and $x = m_\phi/T$. $Y_X = n_X/T^3$ is the yield of particle X with n_X the number density for particle X, and $Y_{X,\mathrm{EQ}}$ is the equilibrium value of Y_X. The expression for Y_ϕ consists of two parts that contribute to the depletion of ϕ: the first line corresponds to the annihilation of ϕ, where $\langle\sigma v\rangle_{\phi\phi\to\mathcal{F}}$ is the thermally averaged cross-section for $\phi^+\phi^- \to \mathcal{F}$ with $\mathcal{F} \in [\ell\bar{\ell}, q\bar{q}, \gamma\gamma, ZZ]$, while the second line corresponds to the

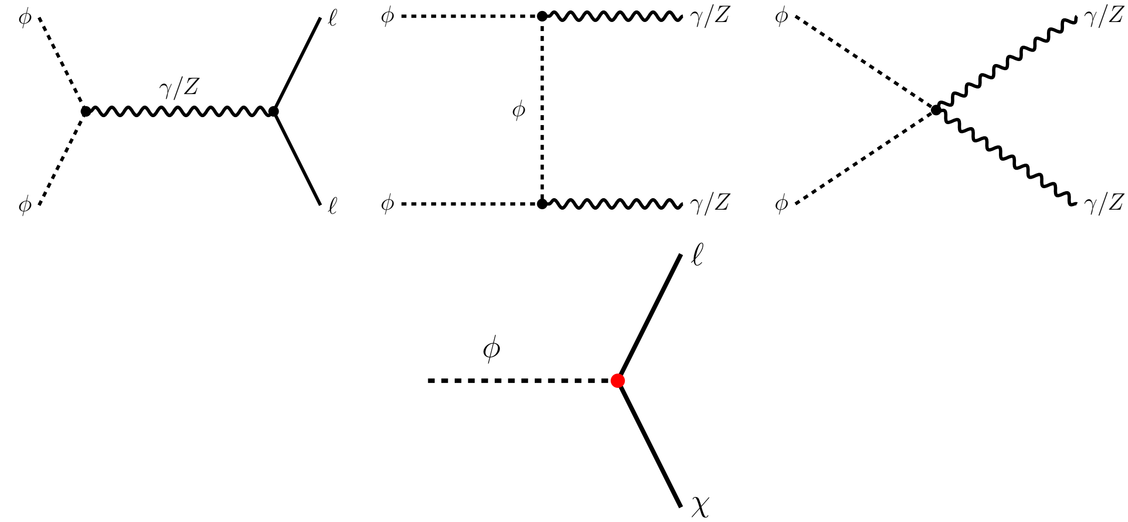

Figure 8. Some diagrams relevant for Boltzmann equations governing freeze-out of ϕ (**top**) and the freeze-in of χ (**bottom**). The freeze-out diagrams are controlled by the electroweak gauge coupling (the black dots), while the freeze-in process is proportional to the small Yukawa coupling λ (red dot). We assume comparable coupling to different lepton flavors in our calculation. Other diagrams with higher number of λ vertices or particle multiplicity are suppressed.

decay of ϕ, where $\Gamma_{\phi\to\ell\chi}$ is the decay width, $g_\phi = 1$ is the number of spin degrees of freedom of ϕ, and K_1 is the first order modified Bessel function of the second kind. The expression for Y_χ has one term which corresponds to the production of χ from $\phi \to \ell\chi$. In the calculations that follow, we assume the couplings $\lambda_i = \lambda$ are all equal. In Figure 8 we see the relevant diagrams for our calculation. In this freeze-in calculation other diagrams involving more λ couplings or additional external particles are suppressed and negligible [117].

We numerically solve these coupled differential equations. In Figure 9 we see the results for benchmark masses and a fixed mediator lifetime. We have chosen the Yukawa coupling λ such that we get the correct final χ relic abundance. From this figure, we see that there are two scenarios that can give rise to the same final χ abundance. For the lighter ϕ, freeze-in of χ dominates its final abundance, gaining

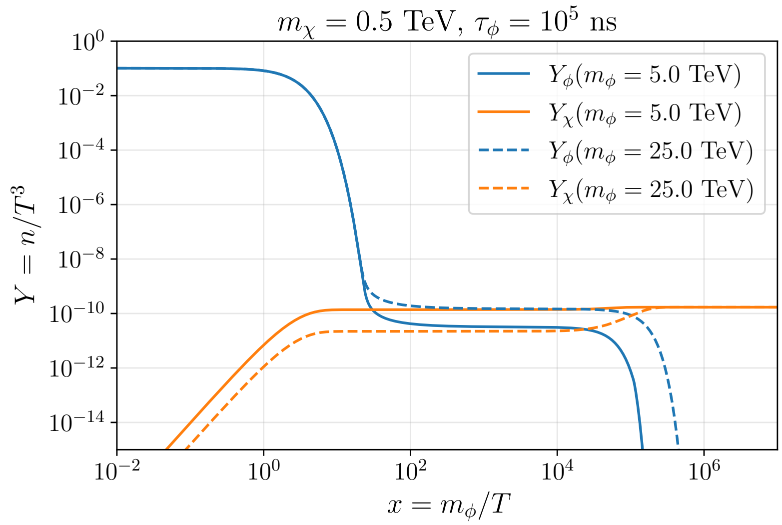

Figure 9. Abundance of χ (orange) and ϕ (blue) for the two m_ϕ values that result in today DM abundance for χ with the given m_χ and ϕ lifetime. Solid (dashed) lines correspond to the light (heavy) ϕ scenarios. The figure shows that we can have scenarios where χ abundance today is mostly dominated by freeze-in of χ itself (solid) or freeze-out, and subsequent decay, of the mediator ϕ (dashed). It also shows that with fixed lifetime and DM mass, there are two different mediator masses (and λ couplings) that give rise to the right relic abundance.

merely a small boost when ϕ decays, while for a heavy ϕ we see that freeze-out of ϕ and its subsequent decay to χ dominates the final χ abundance.

We can then use the final χ yield to calculate its expected relic abundance. Assuming that χ constitutes all of the DM we set $\Omega_\chi h^2 = 0.12$, *e.g.* see Ref. [248], and find the value of the coupling $\lambda = \lambda'$ that recovers this for each pair of ϕ and χ masses. In our analysis we assume the same coupling between DM and all SM RH leptons. In Appendix B.1 we detail our semi-analytic approximation for calculating λ'.

In Figure 10 we show contours of λ' for every point on the mass plane. For large enough m_ϕ values the ϕ freeze-out cross-section will be small enough that we are left with too many ϕ particles after their freeze-out such that, after their decay to χ, the universe will be overclosed. As we decrease m_ϕ, and for a fixed m_χ, at

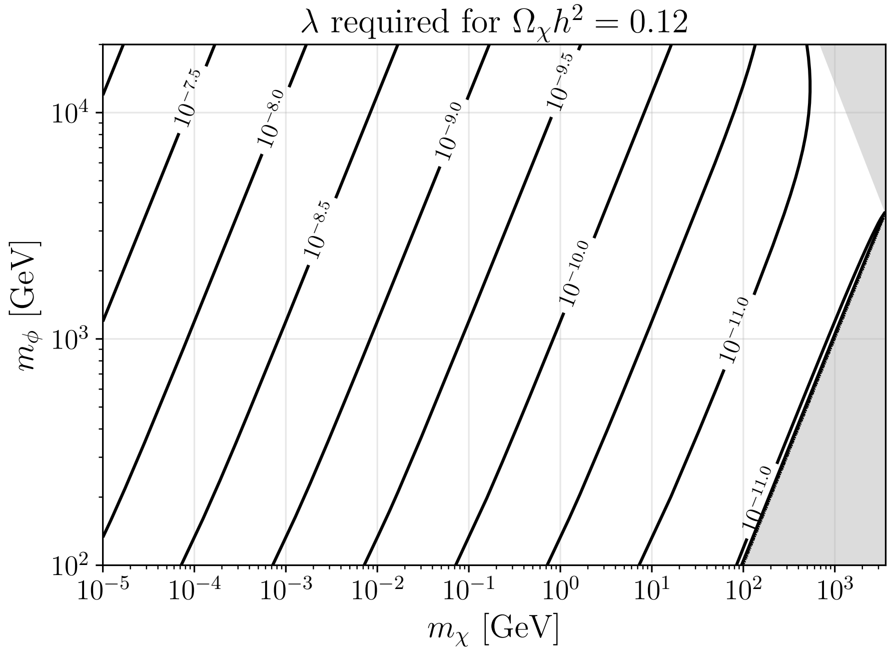

Figure 10. The DM Yukawa coupling, λ', that gives rise to the right relic abundance today. We assume the coupling to each fermion is the same.

some point the freeze-out ϕ abundance will be low enough that, after decaying to χ, we find the correct relic abundance today. The contribution from DM freeze-in to the abundance today will be sub-dominant. For lower m_ϕ values, the DM abundance from ϕ freeze-out and decay is augmented by a non-negligible freeze-in contribution to get the right relic abundance today. Stability of DM also puts a lower bound on the mediator mass $m_\phi \geqslant m_\chi$.

The upper bound on the mediator mass (from DM relic abundance) and the lower bound on it (from DM stability), suggests a bounded viable parameter space. This also implies an upper bound on the DM mass. Our relic abundance calculation shows that this upper bound is

$$m_\chi \lesssim 3.6 \text{ TeV}. \tag{3.4}$$

3.1.2 Existing Constraints.

The on-going searches at LHC already constrain parts of our parameter space. These constraints depend strongly on the lifetime of the mediator. In Figure 11 we show the lifetime of the mediator as given by

$$\tau_\phi = (3\Gamma_{\phi\to\ell\chi})^{-1}, \tag{3.5}$$

where the factor of three is due to the three charged lepton channels. In this calculation we assume the same branching ratio to each final state lepton. This lifetime affects the signal of our model at future colliders as well as at the LHC.

To find the bounds from LHC, we note that our mediator is identical to a right-handed slepton. Many searches for sleptons have been carried out at the LHC, *e.g.* see [249, 250], however, the majority of these searches assume that the sleptons decay promptly. To map the prompt region onto our parameter space, we take anything that has a proper lifetime of $\tau_\phi \lesssim 3\times10^{-2}$ ns as prompt (see further details in section 3.2.2). With this, the prompt searches do not reach high enough ϕ masses to be visible on our bounds plot, regardless of combination of slepton flavors.

On the other hand, searches for long-lived sleptons can probe some parts of the parameter space. In Figure 11 we show the bounds from the long-lived sleptons in Ref. [1] on our model. In applying these bounds we assumed a branching ratio of 1 to the strongest charged lepton channel (selectrons in this case), to be optimistic about the reach of LHC in our parameter space. We also show the bounds from CMS search for staus as heavy stable charged particles in the detector [2]. Figure 11 clearly shows a substantial part of the viable parameter space remains unavailable to LHC, and this motivates searches for this model in future colliders, which we turn to next. Additionally, limits from LEP are always

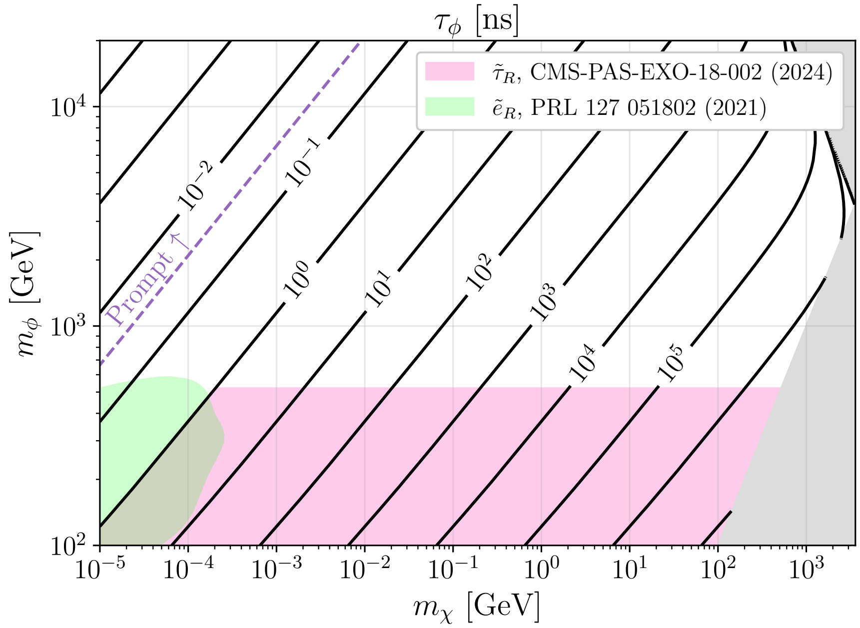

Figure 11. The charged mediator ϕ proper lifetime, τ_ϕ, assuming the Yukawa couplings required to get the right relic abundance (as given in Figure 10). Depending on this quantity, the signal, and thus the collider search strategy, varies significantly across the parameter space. The green (pink) region is already ruled out by the LHC search in Ref. [1] (Ref. [2]). This figure shows a large part of the viable parameter space is not probed by the LHC, motivating future collider searches. The dashed purple line denotes the boundary between our prompt (Section 3.3) and LLP (Section 3.4) search regions, see Section 3.2 for details.

taken into account by assuming that $m_\phi > 100$ GeV [251, 252] and small-scale cosmological structure observables set a limit on the mass of freeze-in DM such that $m_\chi \gtrsim 10$ keV [245, 253, 246].

3.2 Production at Muon Colliders

We now turn to signals of our flavored DM model at a MuC. In our analysis we assume there exists only one flavor of DM. We also remain inclusive over the final state charged leptons in our analysis. Our mediator production rate is independent of the branching ratio to different charged leptons and can be repeated straightforwardly for models where the mediator decays with different branching ratios.

We will calculate the signal yield of our model at a future MuC and comment on the reach of a future MuC in its parameter space. When possible, we will also report the tolerable systematic uncertainty that will still allow a discovery of our model with the aim that our results can inform the detector designs and simulations, especially with regards to LLP signals. We start with a review of the relevant aspects of a future MuC design and then discuss the production cross-section of our model's mediator at such a facility.

3.2.1 A Future Muon Collider. There are many on-going experimental studies about the feasibility and features of a future MuC, including works on a detector design; see Refs. [53, 54, 46, 4, 55, 56] for recent reviews. A final and complete detector design is still an on-going field of research. While this prevents a detailed study of phenomenology of BSM models at a MuC, it underscores the importance of developing a template of canonical models that, in turn, informs the development of the detector.

While further studies are in order, recent progress in the cooling system [254] has revived the hopes for achieving large luminosities at a MuC. The benchmark target luminosity for a high energy MuC with center of mass energy of $\sqrt{s}$ is given by [51]

$$\mathcal{L} \approx 10 \text{ ab}^{-1} \times \left(\frac{\sqrt{s}}{10 \text{ TeV}}\right)^2 , \tag{3.6}$$

which we use in our study as well. We will focus on bechmark center of mass energies $\sqrt{s} = 3$ TeV and $\sqrt{s} = 10$ TeV, for which Eq. (3.6) suggests benchmark 1 (10) ab^{-1} integrated luminosities, respectively.

Subsystem	Region	L dimensions [cm]	$\lvert Z \rvert$ dimensions [cm]	η bound	Material
Vertex Detector	Barrel	$3.0 - 10.4$	65.0	$\lesssim 2.53$	Si
	Endcap	$2.5 - 11.2$	$8.0 - 28.2$	$\lesssim 1.65$	Si
Inner Tracker	Barrel	$12.7 - 55.4$	$48.2 - 69.2$	$\lesssim 1.05$	Si
	Endcap	$40.5 - 55.5$	$52.4 - 219.0$	$\lesssim 1.07$	Si
Outer Tracker	Barrel	$81.9 - 148.6$	124.9	$\lesssim 0.76$	Si
	Endcap	$61.8 - 143.0$	$131.0 - 219.0$	$\lesssim 1.21$	Si
ECAL	Barrel	$150.0 - 170.2$	221.0	$\lesssim 1.08$	W + Si
	Endcap	$31.0 - 170.0$	$230.7 - 250.9$	$\lesssim 1.18$	W + Si
HCAL	Barrel	$174.0 - 333.0$	221.0	$\lesssim 0.62$	Fe + PS
	Endcap	$307.0 - 324.6$	$235.4 - 412.9$	$\lesssim 0.71$	Fe + PS
Solenoid	Barrel	$348.3 - 429.0$	412.9	$\lesssim 0.85$	Al
Muon Detector	Barrel	$446.1 - 645.0$	417.9	$\lesssim 0.61$	Fe + RPC
	Endcap	$57.5 - 645.0$	$417.9 - 563.8$	$\lesssim 0.79$	Fe + RPC

Table 3. Different components of the current proposed detector design for a high energy MuC. Table is adapted from Ref. [4]. The L (Z) dimension refers to the segment size in the transverse (longitudinal) direction. The η bound column is added to the table of Ref. [4] and shows the highest value of pseudorapidity η for a track that completely goes through that region. This information will enter our LLP search in Section 3.4.

In Section 3.4 we outline an LLP search for our model, whose primary signature is displaced leptons at different transverse distances from the beam. This highlights the need for a rough estimate for the size of different components of the detector, hence the need for assuming a benchmark detector design. We use the design sketched in Ref. [4, 55], which in turn is informed by the existing lepton collider designs, *e.g.* see the CLIC [255] and ILC designs [256]. The size of different segments of the detector are reported in Table 3 (table taken from Ref. [4]). We will use the barrel region of these segments in our LLP analysis of Section 3.4.

The closest part of the detector to the beam is a vertex detector that spans transverse distances of up to ten centimeters. The next part is the silicon-based tracking system, filling up the space until transverse distance of around a meter. Outside the tracking detector reside the silicon-tungsten ECAL with thickness of tens of centimeters and a multi-layer HCAL, followed by the magnetic field solenoids stretching roughly up to a radius of four meters away from the beam. Finally, a muon spectroscopy system starts at around transverse distances of four meters and surrounds the entire system.

In addition to these, to mitigate the effect of the beam-induced background (BIB) at a MuC, two tungsten nozzles cladded with borated polyethylene are included in each forward direction. These nozzles limit the access to forward directions; we will assume pseudorapidity $|\eta| \gtrsim 2.4$ is not accessible. See Refs. [256, 4, 55] for further details about the design.

We should remind the reader that Table 3 should not be construed as the final MuC detector design. Our upcoming analysis can straightforwardly be repeated once a concrete design is developed.

The design in Ref. [4] uses a large magnetic field as well. Nonetheless, the effect of this magnetic field will be negligible on our study. In particular, our proposed LLP search in Section 3.4 relies on transverse displacement of displaced leptons, which is not particularly sensitive to the magnetic field (for any feasible magnetic field size in the detector).[3]

3.2.2 Flavored Dark Matter at a Future Muon Collider. In this section we go over basics of our model signals in a future MuC. Since we are focusing on the freeze-in regime, the Yukawa coupling of the DM to SM leptons and the mediator ϕ is very small, thus direct DM production is strongly suppressed. The mediator ϕ, on the other hand, is charged under SM gauge groups and can be produced ubiquitously if kinematically allowed. Subsequently, ϕ can only decay to the DM and a lepton, giving rise to a charged lepton and missing energy in the

[3]An adequately precise measurement of some LLP signals, such as closest approach of the track to the primary vertex, requires a proper inclusion of the magnetic field effect - see Ref. [257] for a recent review. However, we will not study such signals in this paper.

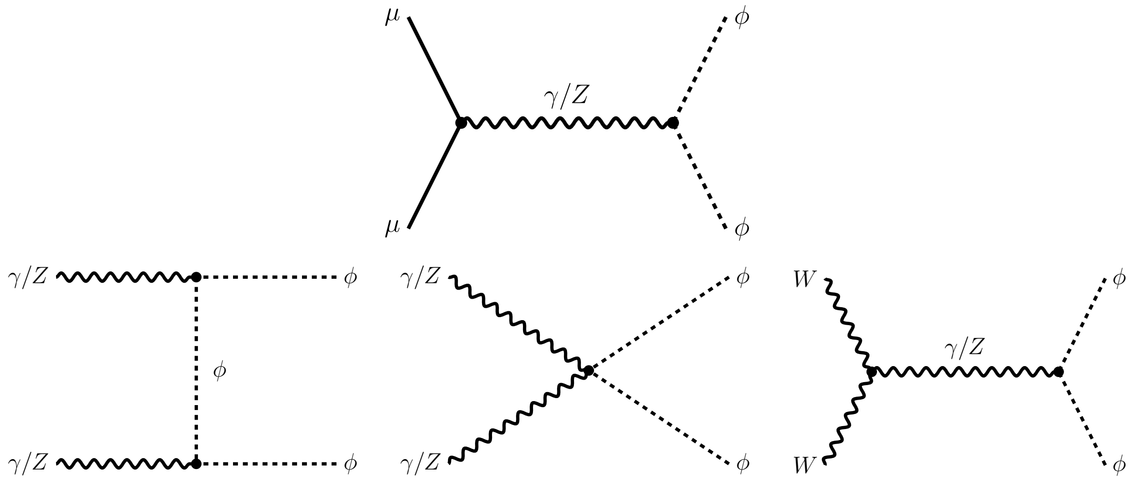

Figure 12. Diagrams pair-producing ϕ at a future MuC. The initial state can be either SM charged leptons (**top**), or electroweak gauge bosons (**bottom**). We refer to these production channels as Drell-Yan (DY) or vector boson fusion (VBF), respectively. The produced ϕ particles are on-shell and will eventually decay to DM χ and a charged lepton. All diagrams involving an off-shell ϕ or their single-production are suppressed by the small Yukawa coupling to DM in our freeze-in setup.

detector. Since the production is determined by SM gauge couplings, our model is a well-motivated target whose signal yield can be used for a plethora of different BSM models, and can inform future detector designs.

Diagrams relevant for ϕ production at a MuC are shown in Figure 12. The kinematic distribution of final states will change depending on the production channel. Similar topologies exist for other flavored DM setups (where ϕ has same charges as other SM fermions). They give rise to a pair of ϕ particles, each of which subsequently decays to a DM particle and a lepton. The branching ratio to different charge leptons will depend on the Yukawa couplings. Without any further structure on the flavor texture, we expect these different branching ratios to be comparable. We remain agnostic about the value of these branching ratios in this work.

The top diagram in Figure 12, which resembles a Drell-Yan (DY) production, comes from initial state muons, whose PDF [258–260] is dominated by longitudinal fractional momentum $x = 1$, while the other three diagrams are similar to vector boson fusion (VBF) production channels. In the VBF production channels the original lepton typically goes undetected in the forward direction down the beam. Nonetheless, it sometimes recoils enough to fall within the detectable η range and will give rise to an extra charged lepton in the final state. We will not consider such events in our search.

We use `MadGraph5` [3] for event generation and study of kinematic distributions. Based on the existing results on various SM particles PDF in a muon [258–260], in our simulations we assume the muons are all produced with longitudinal fractional momentum $x = 1$, while electroweak gauge bosons are modeled with the effective vector approximation (EVA) and already included in `MadGraph5` [260]. The total cross-section for ϕ pair production, from various initial states are shown in Figure 13. We can see from these figures that for heavy mediator masses the production is strongly dominated by DY production channels, while at low m_ϕ values the VBF channel contribution become more relevant (especially for center of mass energy $\sqrt{s} = 10$ TeV). The contribution from DY processes with other SM fermion initial states are negligible compared to the aforementioned production channels.

The model's signal at a collider is substantially affected by the lifetime of the ϕ mediator, see Figure 11. We divide the parameter space of the model by ϕ lifetime, τ_ϕ. Specifically, we will consider two different strategies.

- For $\tau_\phi \lesssim 3 \times 10^{-2}$ ns the mediator decays **promptly** to a lepton and the missing energy in the vicinity of the interaction point.

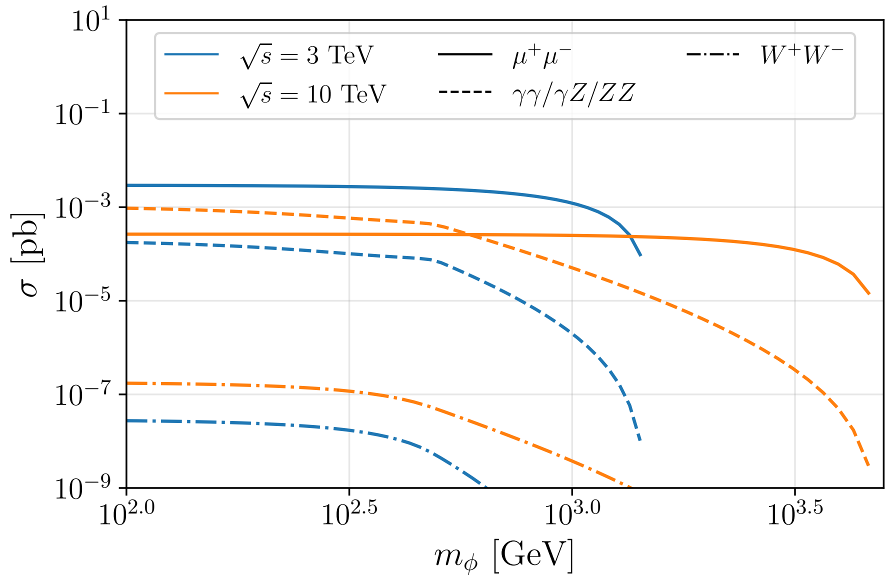

Figure 13. Cross-section for pair production of ϕ mediators at a future MuC with center of mass energy of 3 TeV (**blue**) or 10 TeV (**orange**). We do this calculation using `MadGraph5` [3]. Results for different initial states are shown with line styles, with DY as solid, W VBF as dot-dashed, and γ/Z VBF as dashed. We find that the production is dominated by the DY channel for the mediator masses above a few hundred GeV.

– For $\tau_\phi \gtrsim 3 \times 10^{-2}$ ns the produced mediator particles are **LLP**s, moving inside the detector for a macroscopic distance and leaving a charged track. Depending on the lifetime, they can either decay inside the detector (giving rise to displaced leptons), or escape it (like heavy stable charged particles). In either case, they will leave a detectable charged track in some parts of the detector.

It should be emphasized that our division of the parameter space into prompt and LLP is dependent on detector geometry and exact process details; whether a cut-and-count analysis for prompt signals is applicable to longer lifetimes, or if an LLP search strategy to shorter lifetimes, should be studied on a case-by-case basis and once a final detector design exists.

In the upcoming sections we detail a search strategy and calculate the signal yield in each region. We should emphasize that our proposal is a rudimentary analysis intended to lay out simple search strategies and to demonstrate the power of a high enregy MuC in probing this well-motivated model. In the prompt region we calculate the SM background and report the systematics uncertainties that can be tolerated while still allowing for a discovery. In the LLP region the irreducible background is generated via BIB and the detector response, better understanding of which requires simulations beyond the current work. Thus, in this region we simply report the signal yield and some of its unique features, leaving further studies of the background, systematics, and the reach of a high energy MuC to future works.

3.3 A Search for the Prompt Region

3.3.1 Kinematics and Signal Regions. As the name implies, in this part of the parameter space the signal of our model will be a pair of charged

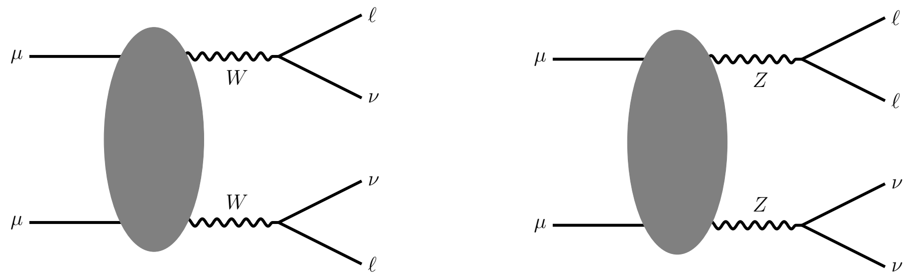

Figure 14. Dominant SM background for our search in the prompt region. The W^+W^- pair-production is potentially the most constraining background; we can suppress this background by applying M_{T2} cuts, see the text for further details.

leptons and missing energy coming from the prompt decay of the mediator ϕ. In this section we go over the kinematics of events in this part of the parameter space and put forward a rudimentary search proposal. We will show that our proposal can discover our model almost over the entire kinematically-accessible region.

The cross-section for ϕ pair production, from various initial states are shown in Figure 13. The main background for this search comes from electroweak gauge bosons pair production and decay in Figure 14.

To reduce these backgrounds, we propose a cut on the event's transverse missing mass M_{T2} [261], the lepton system invariant mass $m_{\ell\ell}$, and the lepton system transverse momentum $p_{T,\ell\ell}$. The background from a pair production of Z bosons can be significantly reduced by $m_{\ell\ell}$ or $p_{T,\ell\ell}$. This is due to the fact that charged leptons originating from SM gauge bosons decays have a much lower invariant mass $m_{\ell\ell}$ and transverse momentum $p_{T,\ell\ell}$ compared to leptons coming from our mediator's decay. The remaining background from pair production of the W boson can also be strongly suppressed by the use of M_{T2}. To see that, we should keep in mind that in our pair production topologies M_{T2} is bounded from above by the mediator mass [261]. Thus, W pair production events have much lower M_{T2} values than the signal events from decays of ϕ.

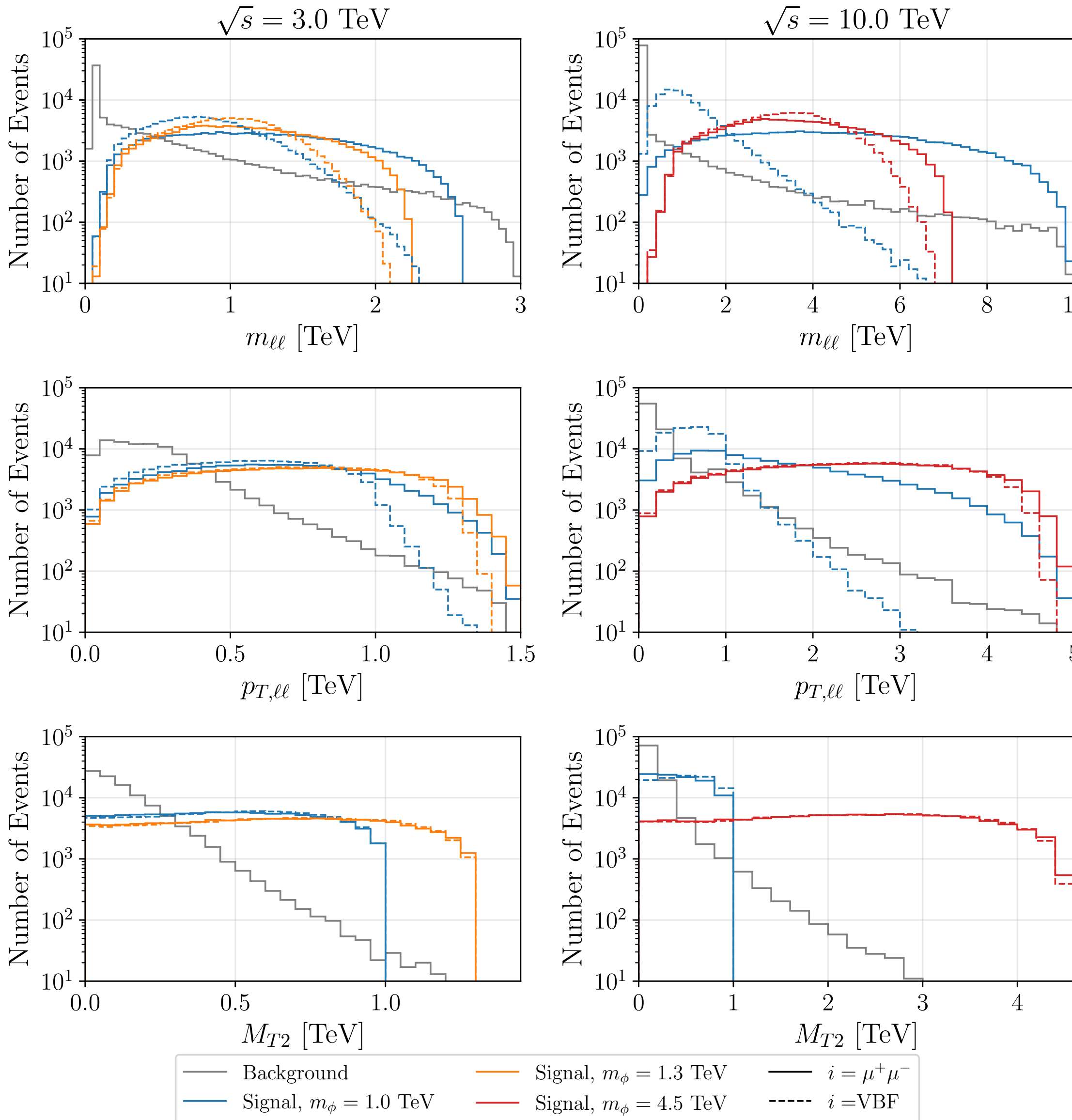

Figure 15. Histograms of invariant lepton mass (**top**), lepton transverse momentum (**middle**), and M_{T2} (**bottom**) for our model (colored) and for SM (gray) at a MuC with center of mass energies of 3 TeV (**left**) and 10 TeV (**right**). The bin size for each observable is 50 (200) GeV for $\sqrt{s} = 3$ (10) TeV. We use `MadGraph5` with 10^5 events to generate each histogram. The solid (dashed) colored histograms refer to signal processes from the DY (VBF) channel. In each figure we show the distribution for two ϕ masses towards the two kinematically accessible ends of the mass ranges. We find a sharp contrast between the SM's and our model's predictions, motivating use of these cuts in our analysis.

To better justify using these cuts, in Figure 15 we show the distribution of events in various kinematic observables, as well as the SM background distributions. We find that the distributions of the SM background and our model differ by orders of magnitude in certain ranges of M_{T2}, $m_{\ell\ell}$, and $p_{T,\ell\ell}$, hence motivating use of these variables. In particular, we find SM background distributions are concentrated at lower values of these parameters, thus justifying the use of a lower bound cut on their value in our analysis. We should also note the difference in the distribution of events from the two signal channels (DY and VBF - see Figure 12).

We use `MadGraph5` [3] to generate events for these histograms. For SM background, we consider the processes $\mu^-\mu^+ \;\to\; \ell^-\ell'^+\bar{\nu}_\ell\nu_{\ell'}$ with $\ell^{(\prime)} \;\in\; [e,\mu]$. Other background channels that come from VBF diagrams (namely $VV \to \mu\mu\nu\nu$) can be approximated with the Improved Weizsacker-Williams (IWW) [262, 263] implementation in `MadGraph5`. We find that the VBF contributions give rise to sub-percent level corrections to the background and can be safely ignored, even before any kinematic cuts.

We propose putting a cut on the three kinematic variables M_{T2}, $m_{\ell\ell}$, and $p_{T,\ell\ell}$ and counting the number of events from our model and from SM backgrounds. We propose different signal regions (with different cuts on each kinematics observable) and allow for different signal regions to have overlaps. For every point in the parameter space we choose the signal region that has the most sensitivity to our signal.

Assuming a Gaussian distribution of SM background events in each signal region, the statistical error bar on each signal region is simply square root of the average number of SM events in that region, denoted by $\sqrt{B}$. Hence, we can quantify the significance of the signal count S in each signal region by simply calculating $S/\sqrt{B}$. (For signal regions for which our `MadGraph5` simulations predict $\sqrt{B} \leqslant 2$, we use statistical error of $\sqrt{B} = 2$ instead to be conservative.) For any given mediator mass, all regions with $S/\sqrt{B} \geqslant 5$ allow a 5σ discovery of our model.[4]

For $\sqrt{s} = 10$ TeV, we find the cuts on $m_{\ell\ell}$, $p_{T,\ell\ell}$, and M_{T2} that optimize our sensitivity to the model with $m_\phi = 1, 4.5$ TeV:

$$\text{Optimized Sensitivity } m_\phi = 1 \text{ TeV} \;:\; (m_{\ell\ell}, p_{T,\ell\ell}, M_{T2}) = (3.60, 1.30, 0.20) \text{ TeV} \tag{3.7}$$

$$\text{Optimized Sensitivity } m_\phi = 4.5 \text{ TeV} \;:\; (m_{\ell\ell}, p_{T,\ell\ell}, M_{T2}) = (1.50, 0.20, 3.50) \text{ TeV} \tag{3.8}$$

For $\sqrt{s} = 3$ TeV, we find the cuts on $m_{\ell\ell}$, $p_{T,\ell\ell}$, and M_{T2} that optimize our sensitivity to the model with $m_\phi = 1, 1.3$ TeV

$$\text{Optimized Sensitivity } m_\phi = 1 \text{ TeV} \;:\; (m_{\ell\ell}, p_{T,\ell\ell}, M_{T2}) = (0.45, 0.69, 0.53) \text{ TeV} \tag{3.9}$$

$$\text{Optimized Sensitivity } m_\phi = 1.3 \text{ TeV} \;:\; (m_{\ell\ell}, p_{T,\ell\ell}, M_{T2}) = (0.26, 0.87, 0.86) \text{ TeV} \tag{3.10}$$

Further details about how we arrive at these cuts are included in Appendix B.2. We use the benchmark mass $m_\phi = 1$ TeV since it is around the lowest mediator mass inside the prompt region, see Figure 11; $m_\phi = 4.5$ TeV ($m_\phi = 1.3$ TeV) for $\sqrt{s} = 10$ TeV ($\sqrt{s} = 3$ TeV) is also around the maximum mass ($\sqrt{s}/2$) that is kinematically accessible. We should note that since the mediator coupling to DM is very small, the signal is completely suppressed for the mass ranges where the mediator can not be produced on-shell.

We use the cuts from Eqs. (3.7)–(3.10) and the average of the cuts on the two extreme mass cases for each center of mass energy to define 27 overlapping

[4] Since we use individual signal regions for a discovery, we do not need to resort to more sophisticated likelihood calculations; repeating this analysis with more complete statistical treatment is straightforward.

signal regions for each center of mass energies. For each point in the parameter space we identify the signal region that has the best $S/\sqrt{B}$. In Figure 16 we show signal regions, as defined in Appendix B.2, that are most sensitive to each point in the parameter space and allow a 5σ discovery. The marked mass range for each signal region shows where that signal region gives rise to a discovery, while neglecting systematics; the small dots for each mass point indicate the best-fit signal region for that mediator mass. It should be noted that this analysis is independent of the DM mass m_χ; for virtually every point in the prompt decay region the DM can be treated as massless.

We find that the cuts are strong enough that essentially any part of the parameter space where ϕ pairs can be produced on-shell can be probed in future MuCs. We find that for most mediator masses there are multiple signal regions that allow a 5σ discovery.

3.3.2 Target Systematics. We have thus far ignored various systematics uncertainties for each signal region. There are many on-going experimental efforts for designing the MuC detector and estimation of systematic uncertainties. Tolerable systematics on well-motivated models, such as the ones studied in this work, can serve as a motivated target in such studies.

In Figure 17 for each ϕ mass we calculate the maximum systematic uncertainties (as a fraction of the statistical uncertainty in that region) that still allows a discovery of our model for that point in the parameter space. In doing so, we assume systematics and statistical uncertainties are uncorrelated. (We also used $\sqrt{B} = 2$ for signal regions that have $\sqrt{B} \leqslant 2$ in our simulations.)

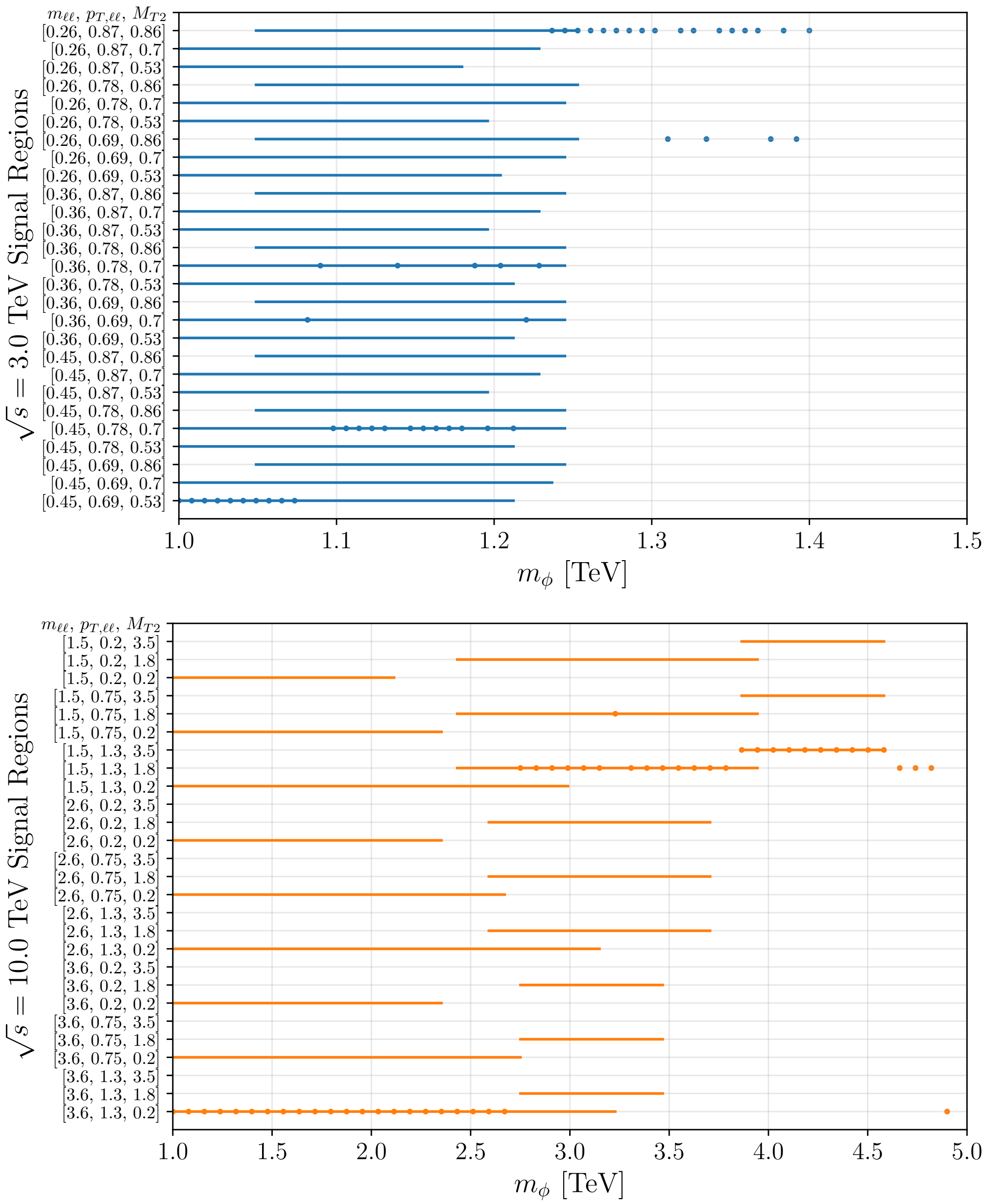

Figure 16. The range of mediator masses that each signal region could discover with 5σ confidence at a future MuC with center of mass energies of 3 TeV (**top**) or 10 TeV (**bottom**), assuming zero systematic uncertainties. The lines indicate the mass range in which each signal region yields a discovery, while the dots denote the best-fit signal region for each mass point. We find that for all masses above a TeV, and almost upto $\sqrt{s}/2$, a future MuC can discover the signal of our model.

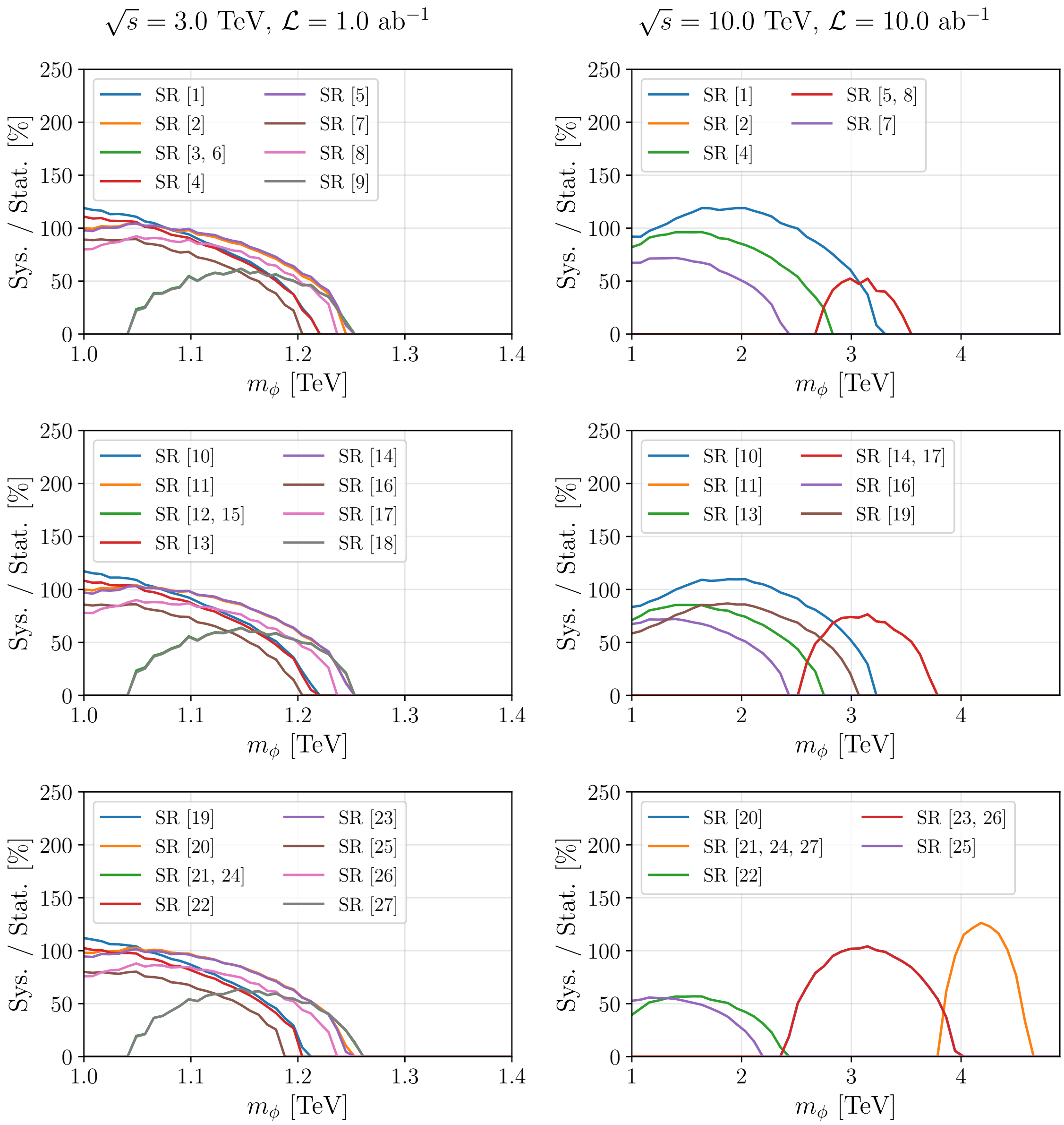

Figure 17. Tolerable systematic uncertainty for each signal region, as a fraction of statistical uncertainty, that still allows a discovery of our model for different mediator masses, see Figure. B.3 for definitions of signal regions. The **left** (**right**) column includes signal regions at a 3 TeV (10 TeV) MuC. We only include signal regions with more than twenty signal events. Signal regions not included in this figure either have fewer signal events or do not give rise to a 5σ discovery of the signal, even in the absence of systematics uncertainties.

This figure shows that even with systematics uncertainties that are comparable to the statistical error in the most-sensitive signal regions, we can still discover our model in the kinematically accessible parts of its parameter space.

Finally, we should point out that in our analysis we used the average background prediction in each signal region according to the results of `MadGraph5` simulations. Theoretical uncertainties on this prediction should also be included in an actual analysis by smearing the SM prediction in each signal region by a Gaussian distribution. We will leave a thorough treatment of all systematics, statistical, and theoretical uncertainties for future works.

It should also be noted that our search can be repeated for other types of flavored DM models. In the case of quark flavored models, we expect to have a jet, instead of the charged lepton, from the primary vertex and our search should be updated accordingly. We expect cuts on similar set of kinematics observables will allow us to probe the prompt region parameter space of all such models as well.

3.4 A Search for the Long-Lived Region

For longer lifetimes, the pair of mediators can leave a charged track in the detector and give rise to various LLP signals, see Refs. [264, 257] for recent reviews of LLPs. In our setup, depending on the lifetime, the produced ϕ particles subsequently either decay to a charged lepton and a DM particle inside the detector, or escape the detector without decaying. Further studies are required for better understanding of the background for these searches, see the discussion below. This prevents us from reporting the discovery reach of a future MuC in our model's parameter space at the moment. Instead, here we focus on the signal yield of our model. In particular, we will calculate the distribution of expected number of displaced leptons in different detector components.[5] We also show that our model exhibits a double-peak feature in some kinematic distributions, that distinguishes it from SM background. Given the fact that our setup is a theoretically-motivated target and its production rate and signals are generic for any electroweakly-charged LLP, we hope this signal yield can serve as a target for experimental studies and detector design efforts.

3.4.1 Long-Lived Particle Kinematics. Previous studies of LLPs at a high energy MuC focused on scenarios where the long lifetime is an artifact of a small mass splitting between the LLP and its neutral daughter [266–268]. In such scenarios the charged decay product, *e.g.* a SM charged lepton, can carry a small momentum and escapes detection, giving rise to a disappearing track signature. In our setup, on the other hand, the mediator and DM have a large mass splitting and the long lifetime of the mediator is an artifact of a small Yukawa coupling. As a result of this large mass splitting, if the mediator decays inside the detector the charged lepton will be easily detectable.

We study the distribution of $\beta\gamma$, where $\beta = v/c$ and $\gamma = (1 - \beta^2)^{-1/2}$, and pseudorapidity η. In Figure 18 we show 1D histograms of $\beta\gamma$ and η for a few different points on our parameter space and for center of mass energies of $\sqrt{s} =$ 3 TeV and $\sqrt{s} = 10$ TeV. In making these histograms we run `MadGraph5` with 10^5 events for each production channel (DY and VBF). We then weigh the number of events from each production channel by its corresponding cross-section to get the combined distribution.

[5] In our model the mediators are always produced in pairs. Thus, each signal event includes two charged tracks and two displaced leptons that could further enhance the search [265]. We, however, will not explicitly use this property in our rudimentary analysis here.

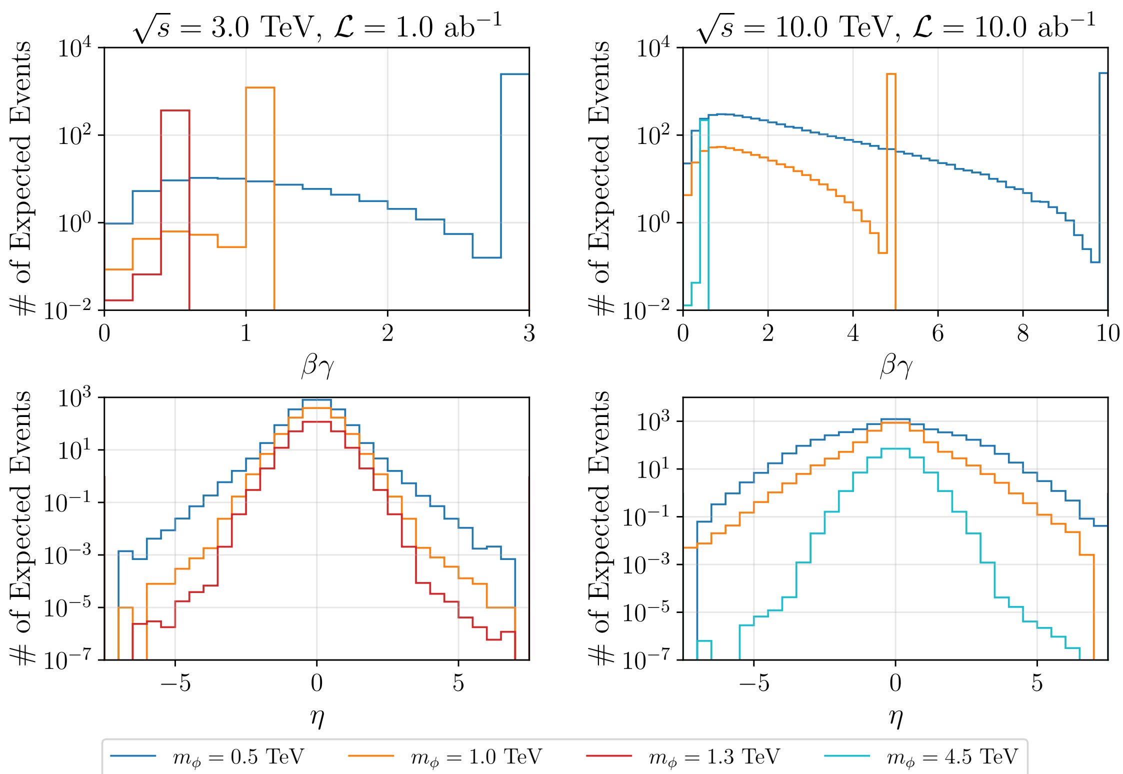

Figure 18. Distribution of events in ϕ's $\beta\gamma$ (**top**) and η (**bottom**) for different mediator masses at a MuC with center of mass energy of $\sqrt{s} = 3$ TeV (**left**) or $\sqrt{s} = 10$ TeV (**right**). The bin sizes are 0.2 and 0.5 for $\beta\gamma$ and η, respectively. The peak feature in the $\beta\gamma$ is due to events from the DY production channel, see Figure 12.

In Figure 18 we see features that are distinct to the individual production channels, DY and VBF, which in turn help inform the types of cuts we can use in a search for our model. In the DY channel, the initial muons each carry $E = \sqrt{s}/2$, which in turn gives rise to the maximum value of $\gamma = E/m_\phi$ for a given m_ϕ and leads to the very sharp peak in the $\beta\gamma$ distribution. An increase in m_ϕ results in a smaller γ, so the peak of the $\beta\gamma$ distribution will shift to lower values.[6] We find that this channel gives rise to centralized ϕ particles (small $|\eta|$) as well. This motivates searches focusing on this region. The VBF production channel gives rise to a wider spread in both $\beta\gamma$ and η, owing to the wider spread of initial gauge bosons PDF [258–260].

3.4.2 Background and Time-of-flight. The background for LLPs can be divided into a reducible SM background, and an irreducible background from the detector response. While there are a handful of SM particles that appear as LLPs at a collider (*e.g.* see Ref. [269]), using various kinematic observables, such as time-of-flight or anomalous ionization rate (dE/dx), allows us to distinguish them from heavy new physics LLPs. Other techniques such as empty bunch crossing also allows us to better understand and reject SM background; see Ref. [264] for further discussions of SM background mitigation techniques.

[6] Currently the muon PDF in a muon beam is not implemented in `MadGraph5`. Thus, in our simulations we assumed each muon enters the interaction with $\sqrt{s}/2$ energy as an approximation. The PDF of a muon in the beam has support for $x \neq 1$ as well [258–260]. As a result, the real distribution of $\beta\gamma$ from this channel is slightly diffused to values smaller than $\sqrt{s}/2$. Including the PDF will soften the peak in the distribution of events from the DY channel. Nonetheless, given the sharp peak in a muon PDF [258–260], we still expect a large peak in various kinematic distributions from this channel if the real muon PDF is included in the simulation.

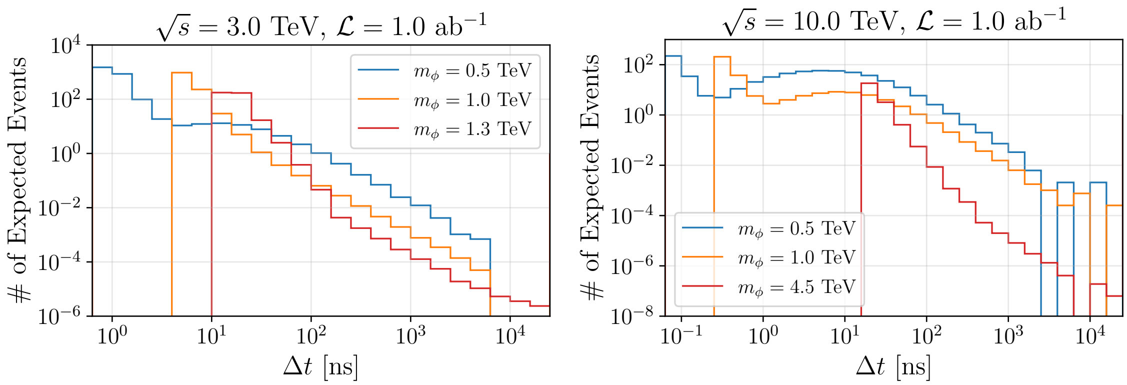

Figure 19. Distribution of the difference between the arrival time of ϕ and a massless particle moving in the same direction at the onset of the muon system ($L = 446.1$ cm), as predicted in our `MadGraph5` simulation for three different mediator masses. In these histograms the log-scale x-axis is binned in steps of 0.2 decades. The arrival time scales linearly with L. Events at lower (higher) Δt values correspond to the DY (VBF) production channel. As the mediator mass increases, the LLPs move more slowly, shifting the distributions to higher Δt values.

A useful quantity in reducing the SM background is the time-of-flight.[7] In particular, the difference between the arrival time of a ϕ particle and SM particles in the same direction, $\Delta t = t_{\rm LLP} - t_{\rm SM}$, can be used to distinguish it from SM particles, which move with $\beta = 1$. In Figure 19 we show the distribution of this variable, at the inner border of the muon system ($L = 446.1$ cm transverse distance from the beam in the design of Table 3). The time difference scales linearly with the transverse distance L at which we measure it, thus we can use this figure to calculate the time difference at different transverse distances in the detector.

[7] Another useful quantity in LLP searches is the anomalous ionization rate dE/dx. In particular, this quantity can be used in reconstructing the track mass and cutting away SM background. At LHC, measuring dE/dx has a smaller uncertainty when only the barrel region pixel layers are used. This motivates LLP searches focusing on the central events at a MuC as well. A proper calculation of this rate depends on characteristics of the detector material and tracks interactions with the detector, which can only be extracted from simulations. As a result, we acknowledge the possibility of using this quantity and its importance in the LLP searches, leaving more in-depth studies for future.

Small Δt events in Figure 19 are produced by the DY initial channel (with larger β and $\beta\gamma$ values), while events from the VBF channel arrive later since they have lower values of β. This figure shows that, at $L = 446.1$ cm, timing resolution of around $0.1 - 1$ ns ($1 - 100$ ns) is enough to separate most events from the DY (VBF) channel from SM background. When compared to the current timing resolution at LHC ($\sim 0.1 - 1$ ns for comparable L values), we find that majority of events, especially from the VBF channel or for large enough m_ϕ values, arrive with enough delay that we can use the time-of-flight information to discern our LLP signal from background.

In addition to the SM reducible background discussed above, interactions of the beam, various tracks, or the BIB, with the material in the detector give rise to an irreducible background. Currently, there are limited studies on this topic [266]. Nonetheless, they have shown that such background events can be mitigated by timing information, track quality, and tracks directionality information. Further studies are in order to completely understand the detector response and background for LLP searches at a high energy MuC and, depending on the lifetime, different background mitigation strategies have to be deployed.

To be able to discover our model, we need to estimate this irreducible background as well. This can only be done with extensive simulations, beyond the scope of this work. Nonetheless, the signal yield of our model sets a reasonable target precision. Given the theoretical motivation of our model, and how generic its signal yield is for all models of electroweakly-generated LLPs, we hope our results in the upcoming section inform the on-going studies in developing the detector design.

3.4.3 Charged Tracks and Displaced Leptons Signal.

In this section we calculate the signal yield of our model on the LLP part of the parameter space. We will show that our model gives rise to many events across the entire kinetically-accessible part of the parameter space. We will, in particular, highlight a double-peak feature in the distribution of events in the detector, and argue that it is a shared signature of all electroweakly-charged LLPs at a high energy MuC.

The kinematic quantities $\beta\gamma$ and η directly enter the calculation of the trajectory of LLPs inside the detector. In LLP searches we are in particular interested in the transverse direction away from the beam, L. It can be shown that for realistic magnetic field values, the track curvature for $m_\phi \gtrsim 1$ TeV is very small and will not affect the LLP observables under study here.[8] Thus, we neglect the effect of the magnetic field and assume the tracks move on straight lines after their production.

We can show that as a function of time, the transverse distance from the beam at time t (in the lab frame) is given by

$$L(t, \beta, \eta) = \frac{\beta t}{\cosh \eta}. \tag{3.11}$$

Using this we can calculate the transverse displacement for every event at $t = \gamma\tau_\phi$. The time $t = \gamma\tau_\phi$, is the average time at which the ϕ particle decays to a charged lepton and missing energy, giving rise to a displaced lepton.

In Figure 20 we show the distribution of transverse displacement L at $t = \gamma\tau_\phi$ for a few different points in our parameter space. The sharp peak in large L/τ_ϕ values in the distributions corresponds to events from the DY channel that all have a very large $\beta\gamma$ value. We also find that for smaller mediator masses the

[8]For precise measurements of some LLP observables, such as closest approach of the track to the primary vertex, one needs to include the effect of the magnetic field. However, this is not the case for the displaced leptons and charged tracks signals studied in this work.

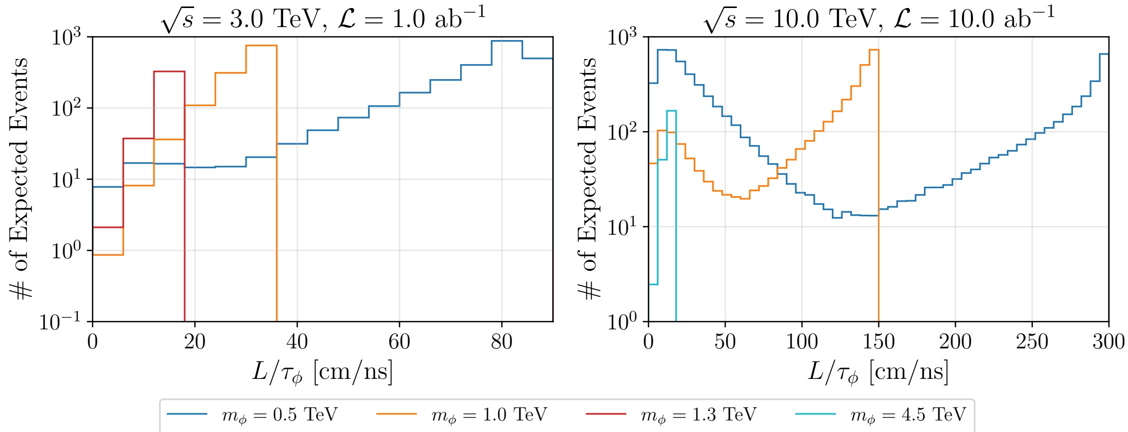

Figure 20. Distribution of events in ϕ's transverse displacement at $t = \gamma\tau_\phi$ normalized by the lifetime, L/τ_ϕ for different mediator masses at a MuC with center of mass energy of $\sqrt{s} = 3$ TeV (**left**) or $\sqrt{s} = 10$ TeV (**right**). The bin sizes are 6 cm/ns. The shape of the L/τ_ϕ can be inferred from distributions in Figure 18 and Eq. (3.11). For different points in the parameter space the mediator lifetime τ_ϕ can be read off of Figure 11; combined with these plots, we can then find the transverse displacement for events at any point in the parameter space for every DM mass. The double-peak feature in the right figure can give rise to interesting LLP signals, as elaborated in the text.

distribution stretches to larger values of L/τ_ϕ, giving rise to more displaced leptons further away from the beam.

The L/τ_ϕ distribution exhibits an interesting double-peak feature; the peak at large values arises from the DY production while the peak at lower values is an artifact of the η dependence in Eq. (3.11) and arise from VBF channel. Since these production channels universally apply to all electroweakly-charged LLPs, we expect a similar double-peak feature in the distribution of L/τ_ϕ in all such models.[9] The main irreducible background for LLP searches come from secondary interactions of particles with the detector material and this double-peak feature may not be manifested in this background. As a result, this feature could be a

[9]Once the muon PDF is properly included in the simulations, we expect this peak to spread out to some extent. Nonetheless, the sharp peak at $x \to 1$ in this PDF [258–260] still will give rise to a peak in the $\beta\gamma$ and in L/τ_ϕ distributions, maintaining this double-peak feature.

smoking gun signature of electroweakly-charged LLPs at a MuC and could be used for an efficient background rejection.

In Figure 21 we show the joint distribution of events on the plane of $\eta - \beta\gamma$ for a few different mediator masses. In each plot we can see a cluster of events at highest physically possible value of $\beta\gamma$ which correspond to the DY-generated events. The VBF-generated events have a wider distribution in both η and $\beta\gamma$, as expected.

We also show contours of constant L/τ_ϕ on the $\beta\gamma - \eta$ plane in Figure 21. The shape of these contours can be inferred from Eq. (3.11). For a fixed value of τ_ϕ, these contours tell us at what transverse distances the ϕ particle will (on average) decay and inform the signal yield of our model. For $\tau_\phi = 1$ ns these contours show L in cm, while for larger lifetimes, the contours of constant L move down on the plots. We can repeat this calculation for all mediator and DM masses to calculate the rate for displaced leptons appearing in any transverse distance segment of the detector, inclusive over other kinematic variables such as η and $\beta\gamma$. The rate for displaced leptons appearing at a given transverse distance is our model's main signature in the LLP region.

The transverse distance can be mapped to detector components as defined in Table 3. We show the average number of displaced leptons in the barrel region of each detector component on our model parameter space in Figures 22 and 24 (Figures 23 and 25) for $\sqrt{s} = 3$ TeV ($\sqrt{s} = 10$ TeV).[10] Endcap regions are neglected since, similar to LHC, it is reasonable to expect more SM background in endcaps

[10]In the compressed region, $m_\phi \approx m_\chi$, the daughter lepton from ϕ decay will be soft and will typically escape detection, giving rise to a disappearing track if they decay inside the detector. However, the lifetime τ_ϕ is very long in this region of the parameter space (see Figure 11), so our signal will still be a heavy stable charged track. The disappearing track signals for LLPs that decay inside a MuC are studied extensively in Ref. [266].

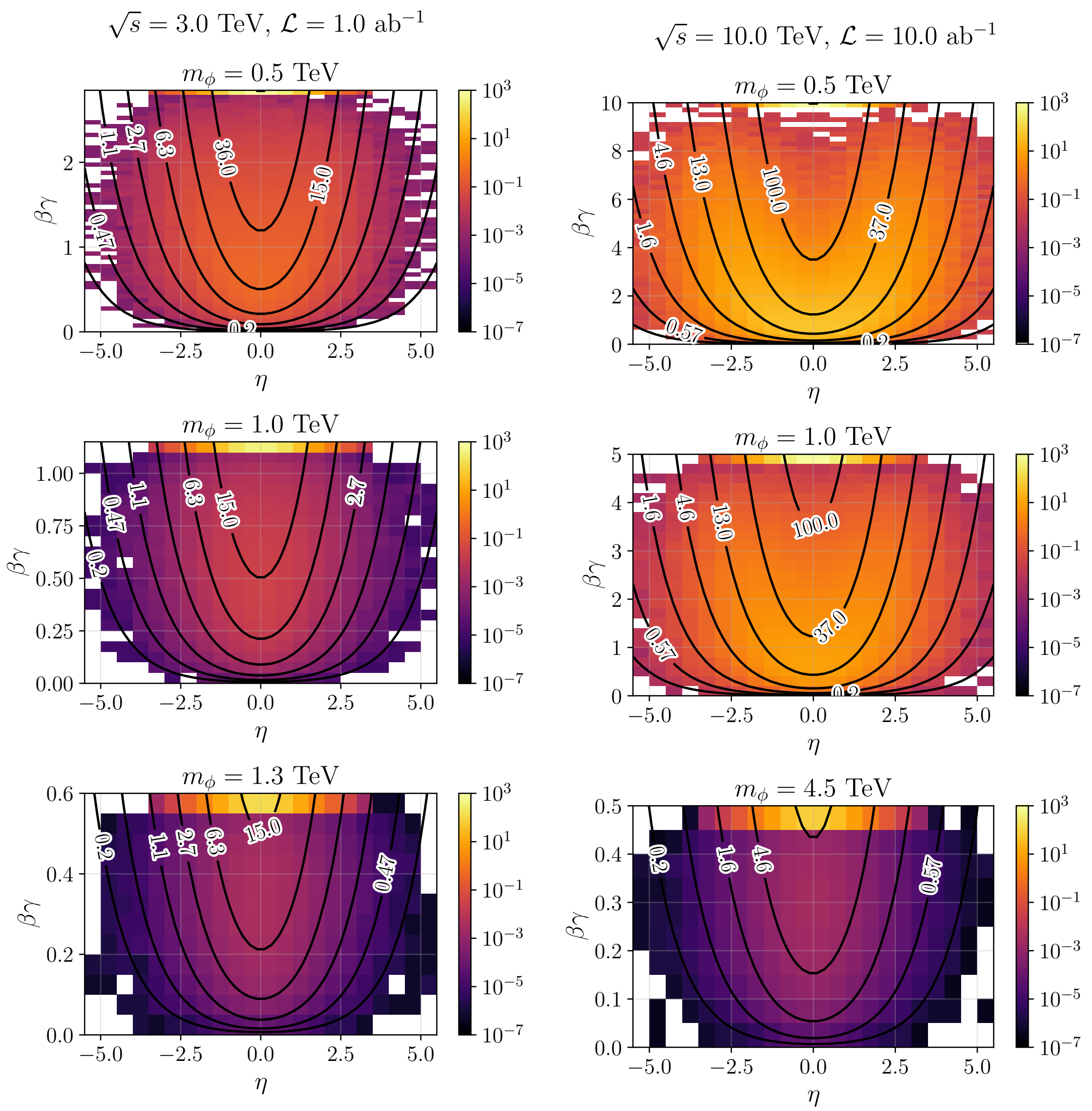

Figure 21. Distribution of events in the $\eta - \beta\gamma$ plane for different ϕ masses at a 3 (10) TeV MuC on **left** (**right**). The bin sizes are 0.5 for η. For $\beta\gamma$, the bin size is 0.05 except for $\sqrt{s} = 10$ TeV and $m_\phi \leq 1$ TeV, where we use 0.2. Contours of constant L/τ_ϕ [cm/ns] are shown as well (see Eq. (3.11)), see the text for further explanation on the shape of the contours. The cluster of events at maximum $\beta\gamma$ values are from the DY production channel. We find that majority of events from the DY and the VBF channel appear with different kinematics.

with large track masses that are difficult to distinguish from LLP signals, and that dE/dx measurements in the endcaps are slightly less accurate compared to their barrel region counterparts. Our analysis can be straightforwardly repeated for the endcap regions as well.

In Figures 22 and 23 we show the signal yield on the plane of m_χ-m_ϕ. In each detector component, the distribution of events clearly divides up into two separate regions. The upper cluster of events in these figures - at lower m_χ and higher m_ϕ values - corresponds to events originating from initial DY channel, while the other cluster of events come from the initial VBF channel. These two separate clusters of events are a manifestation of the previously explained "double-peak" feature seen in Figure 20.

The features of the signal regions in Figures 22 and 23 can be understood through the shape of the L contours in Figure 21. Recall that for a fixed value of τ_ϕ, the contours in Figure 21 tell us at what transverse distances the ϕ particle will (on average) decay, *i.e.* $L(t = \gamma\tau_\phi)$. At very short lifetimes, the contours associated with each barrel region in Figure 21 are above the entire distribution of events. As the lifetime increases, contours of constant L move down on Figure 21 (see Figure 11 for contours of constant lifetime). For fixed m_ϕ, τ_ϕ increases with higher m_χ values, and so we find that the events at low m_χ are predominantly from the DY channel (as they are on top of 2D histograms in Figure 21). As we increase m_χ (and τ_ϕ), the VBF channel increasingly contributes. Since distributions of DY- and VBF-generated events peak at different $\beta\gamma$ values in Figure 21, we find two separate cluster of events in each detector component in Figures 22 and 23. The slope of each cluster of events is inherited from contours of constant lifetime on the mass plane, see Figure 11.

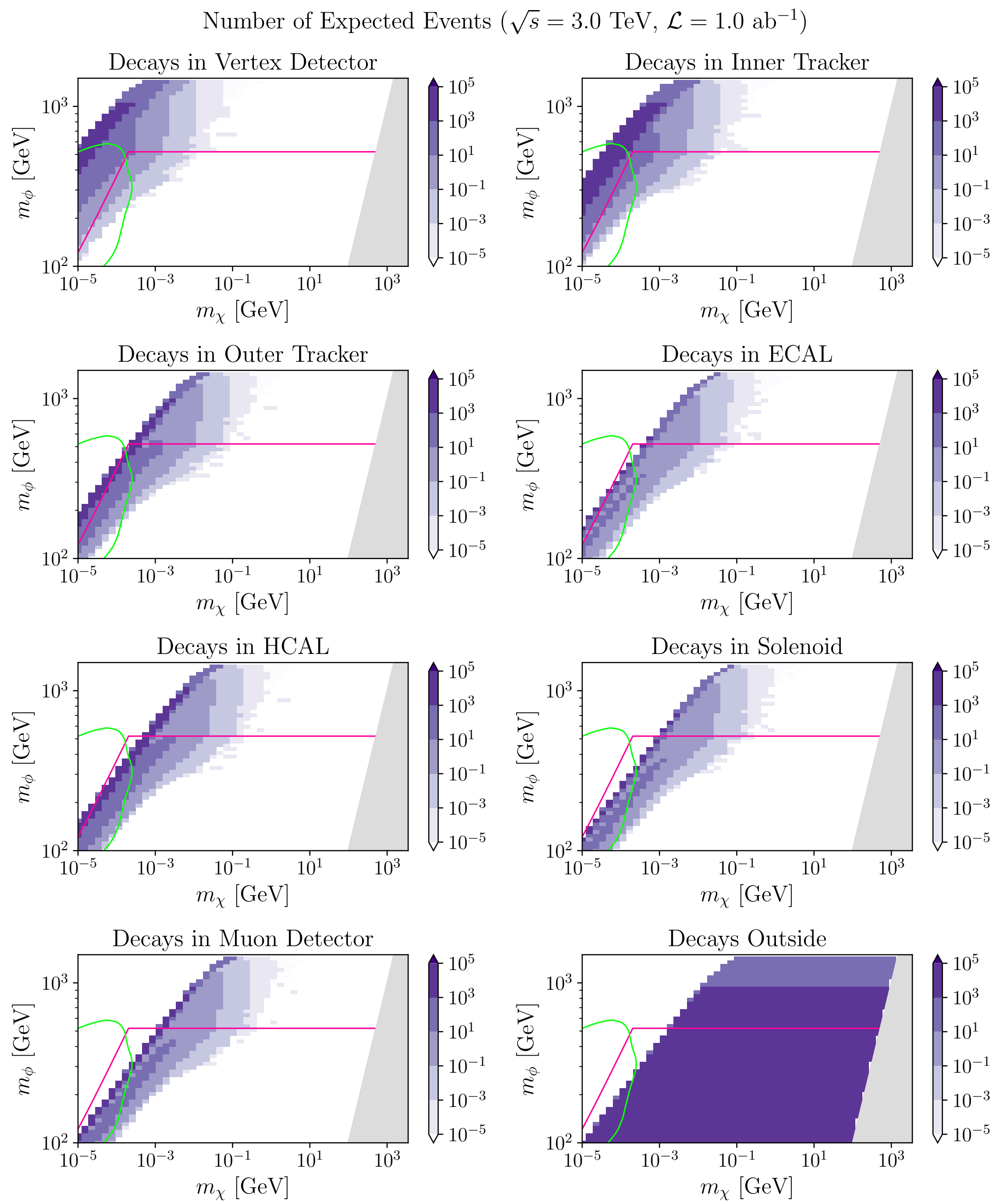

Figure 22. Average rate of displaced leptons in different barrel regions of the detector for a 3 TeV MuC, assuming the tentative design of Table 3, as well as average number of detector-stable charged tracks. The DM Yukawa coupling to the mediator is chosen to get the right relic abundance today. The left (right) cluster corresponds to events from the initial DY (VBF) channel of Figure 12, see the text for further explanation about the shape of contours. The gray region corresponds to $m_\chi > m_\phi$ and is not phenomenologically viable. Our model's signal yield can serve as a benchmark in studies of tolerable systematics in LLP searches at a MuC. The region below the green (pink) line is already ruled out by the LHC search in Ref. [1] (Ref. [2]).

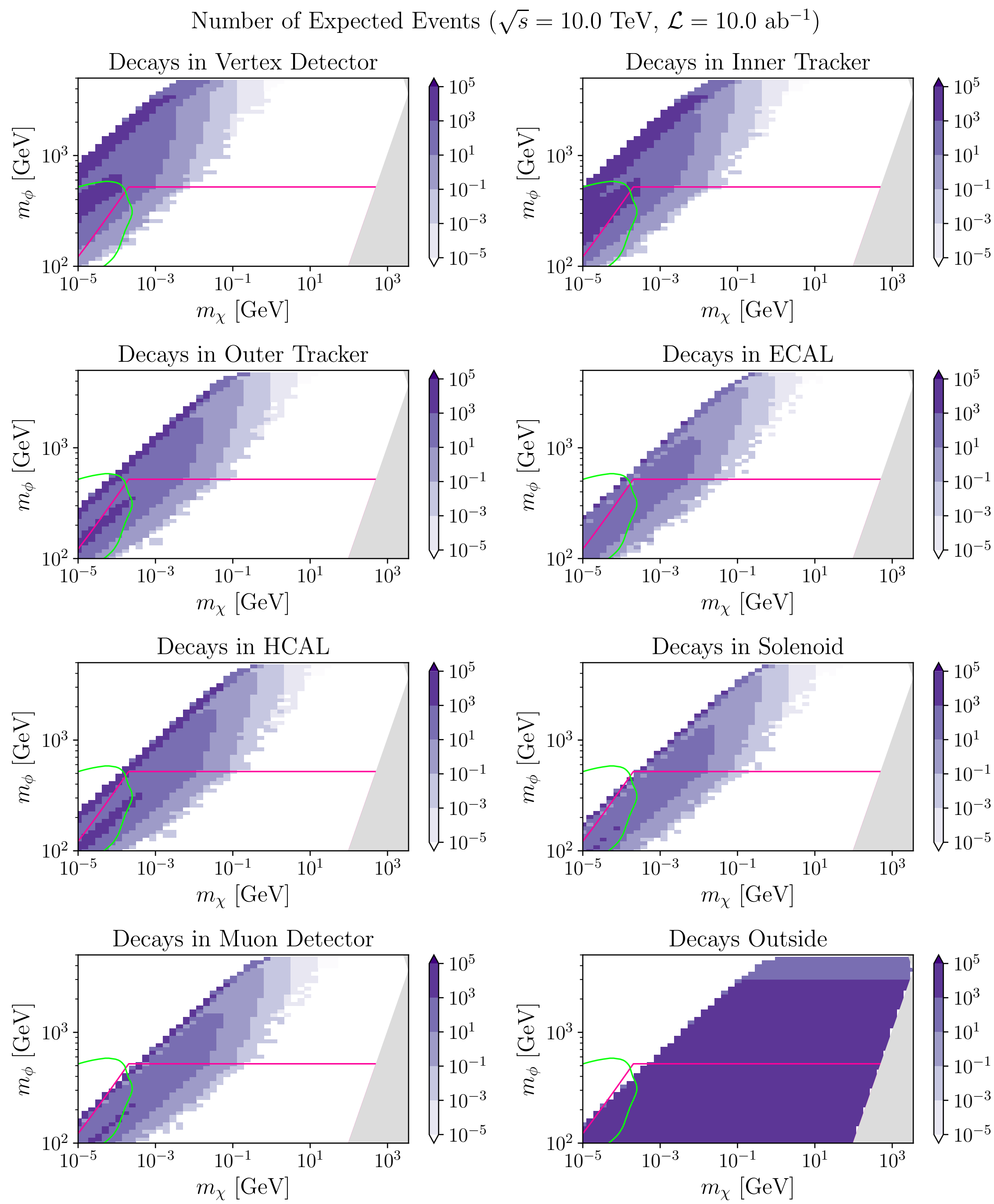

Figure 23. Similar to Figure 22, but for a MuC with center of mass energy of $\sqrt{s} = 10$ TeV. We again find that virtually the entire kinematically-accessible part of the parameter space gives rise to large numbers of charged tracks and displaced leptons. The region below the green (pink) line is already ruled out by the LHC search in Ref. [1] (Ref. [2]).

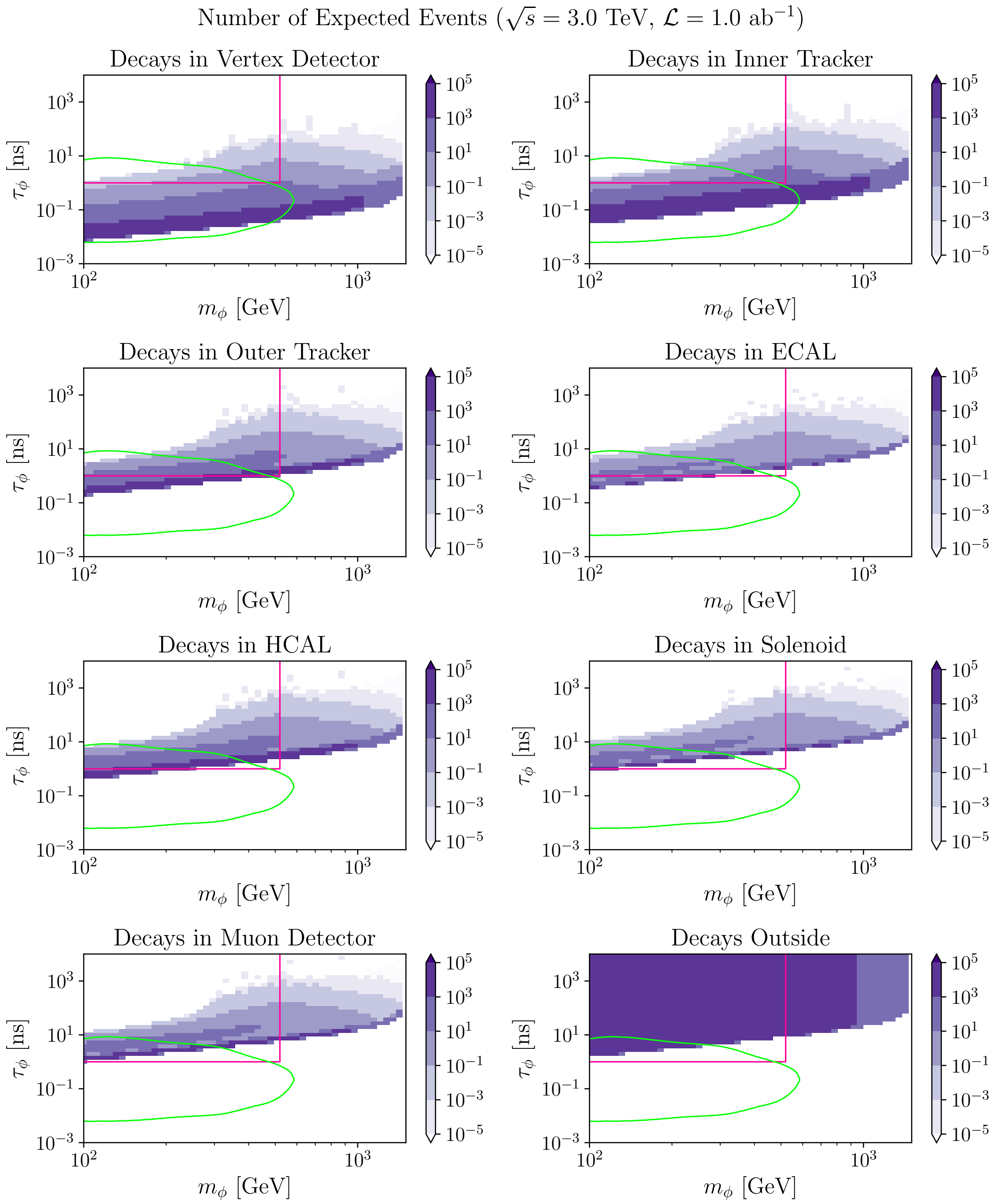

Figure 24. Same as Figure 22 but on the plane of m_ϕ-τ_ϕ. We find a large signal yield, in at least one component of the detector, for most of the parameter space beyond the current LHC reach. The region below the green (pink) line is already ruled out by the LHC search in Ref. [1] (Ref. [2]).

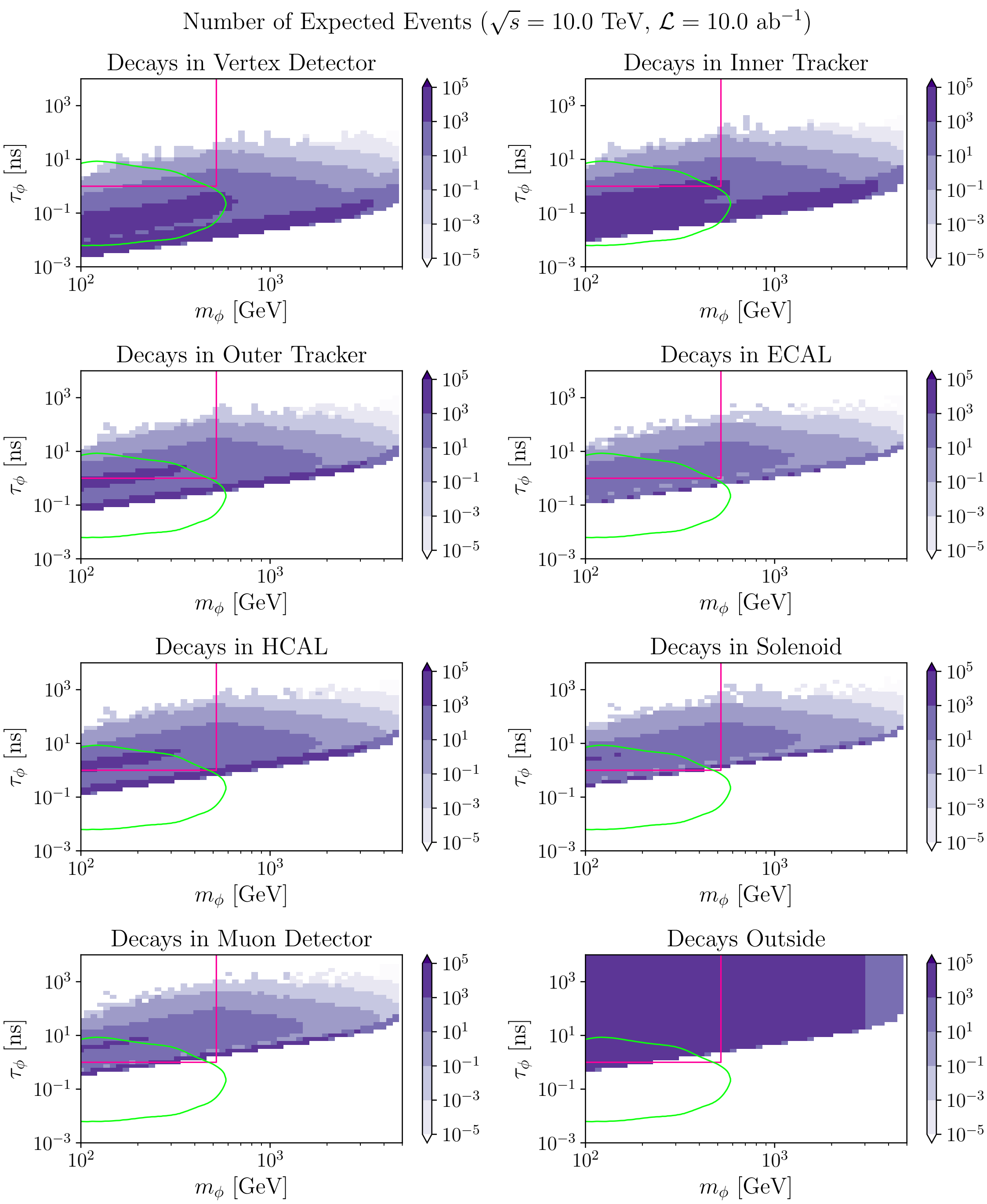

Figure 25. Same as Figure 23 but on the plane of m_ϕ-τ_ϕ. We find a large signal yield, in at least one component of the detector, for most of the parameter space beyond the current LHC reach. The region below the green (pink) line is already ruled out by the LHC search in Ref. [1] (Ref. [2]).

The last panel in both Figures 22 and 23 corresponds to tracks that are expected to go outside the detectors without decaying. We only include the tracks with small enough ηs that go through all barrel regions, *i.e.* $\eta \lesssim 0.61$, see Table 3. These panels clearly show a large number of such stable tracks are expected on a large part of the viable parameter space, allowing us to look for the signals of this model on virtually the entire kinematically accessible parameter space.

In Figures 24 and 25 we present the same information (the signal yield in each detector component) on the m_ϕ-τ_ϕ plane. Existing LHC bounds on the parameter space are marked again. We clearly see that at a MuC, a large part of the parameter space unaccessible at LHC will have a large signal yield. The double-peak feature discussed above is clearly visible in these plots as well.

Our results should be contrasted to the current bounds from LHC on Figure 11. Putting the numbers from all panels of Figures 22–25 together, we find that we have at least 10^3 events in at least one part of the detector for almost the entire kinematically-accessible parts of our parameter space, see Appendix B.3. Hence, once a reasonable degree of systematics is achieved, future high energy MuCs can sift through a much larger part of the parameter space than LHC. This clearly underscores the supremacy of a high energy MuC in searching for this DM model. Crucial in this supremacy are the stable tracks that go through the entire detector without decaying, see the last panel of Figures 22–25. For most of the parameter space this is the dominant LLP signal and can be used for probing the parameter space inaccessible by displaced lepton signals in the detector. The double-peak feature, which in turn is an artifact of two distinct production channels, suggests for many points in the parameter space we can have many displaced leptons in more than one component of the detector.

We should emphasize that Figures 22–25 show the *average* number of decays and displaced leptons (or stable charged tracks). The true number of events in each barrel region will be drawn from a Poisson distribution around this average. Further details about kinematics of our model in the LLP region are included in Appendix B.3.

3.5 Conclusions

We initiated a detailed study of the freeze-in flavored DM setup in which flavored DM coupling to the slepton-like mediator is very small. We showed that the interplay of direct freeze-in and the mediator freeze-out gives rise to an interesting abundance calculation, such that the dark matter mass should be below a few TeV in order to avoid overclosing the universe. Combined with the existing collider and astrophysical bounds, this gives rise to a bounded viable parameter space for this model.

We also studied signals of our model at a future high energy Muon Collider (MuC). As a result of the feeble Yukawa coupling of DM, all signals of the model in a MuC originate from the on-shell pair production of the mediator. The range of mediator masses and lifetimes in the viable parameter space is such that we can have prompt, as well as various long-lived particle signals at a MuC. We divided our parameter space into two broad ranges according to the mediator's lifetime, namely prompt and LLP regions.

In the prompt decay region, we proposed a rudimentary analysis and identified the target systematics that ought to be achieved in order to discover our model at a MuC. Our analysis uses cuts on invariant leptonic system mass $m_{\ell\ell}$, missing transverse mass parameter M_{T2}, and the leptonic system transverse momentum $p_{T,\ell\ell}$. We found that in the part of the parameter space with prompt mediator decay, if systematic uncertainties are comparable or smaller than SM background, our proposed analysis can discover this model at effectively the entire kinematically-accessible parameter space.

For longer lifetimes, we will have a charged track in the detector which, depending on the lifetime, can either decay to a lepton and missing energy or decay outside the detector. While the SM background can be reduced away using quantities such as time-of-flight or anomalous ionization rate, detector response can give rise to an irreducible background. A proper study of these effects requires extensive simulations and is left for future works. In the absence of concrete simulations, here we reported the signal yield and various kinematics distributions. In particular, we showed that the displaced lepton distribution has a double-peak signature that could potentially be used for efficient background rejection. This feature appears as two large sets of signal events, produced through the two distinct channels (DY and VBF), in different detector components.

Our work can be extended in many directions. Foremost among them is a detailed study of the detector design that enables detailed studies of the background. Given the great reach of future MuCs in our model's parameter space, the universality of its production rate, and its theoretical motivation, we believe our model can serve as a motivated benchmark target for future studies on development of the detector by setting a target for systematics of such works.

Our analysis can also be repeated for other flavored DM models, *i.e.* mediators with same charges as other SM fermions. All these setups have the added bonus that the artificial alignment of the DM Yukawa and SM Yukawas in flavored DM models, required for evading bounds from flavor-changing neutral currents and lepton flavor violation, are completely avoided thanks to the feeble

DM coupling. While the relic abundance calculation resembles the calculation here, we expect a different collider phenomenology for some of them thanks to their different production and decay channels.

Furthermore, as alluded to earlier, the muon PDF is not yet included in `MadGraph5`, thus we neglected its effect in the DY production channel. With the ever-growing interest in BSM signals at a MuC, it is interesting to work on proper embedding of this PDF in the event-generation pipeline.

It will also be interesting to consider signals of such models in other experiments, such as various astrophysical or direct detection searches. (See Refs. [245, 246] for a study of astrophysical bounds on a quark-flavored DM model in the freeze-in regime.) In particular, there is a large part of the parameter space inaccessible to colliders in foreseeable future, motivating searches in the aforementioned complementary fronts.

High energy MuCs are strongly motivated for their ability in probing different models of the Higgs boson UV-completion, flavorful new physics, and DM models. Our study outlines a simple and interesting DM model with unique signatures that can serve as a target for searches at a high energy MuC and inform its detector design.

CHAPTER IV

MORE FLAVORED DARK MATTER MODELS AT MUON COLLIDERS

This chapter reflects ongoing work by Pouya Asadi, Sam Homiller, Aria Radick, and Tien-Tien Yu. This work builds on Aria Radick's workflows from [119] and Sam Homiller is working on methods to incorporate the muon PDF into the analysis.

4.1 Flavored Dark Matter Models

In chapter III we looked at one particular type of flavored dark matter, but there is nothing stopping us from coupling to other types of fermions. In this section we will outline some additional flavored models, including the left-handed lepton model and two quark models.

4.1.1 Left-Handed Lepton Model.

$$\mathcal{L} \supset -\lambda_i \bar{\Phi} \chi L^i + \text{c.c.} \tag{4.1}$$

The left-handed lepton model is analogous to the model we studied in chapter III, except that we now have two new scalars. We introduce Φ, having the same charge as L, namely hypercharge $Y = -1/2$. We still have ϕ^-, which interacts with the charged leptons, but there is a second component of Φ that interacts with neutrinos, ϕ^0. This leads to a new coupling between ϕ^-, ϕ^0, and W. The difference in charge between the two components of Φ leads to a mass splitting [270]

$$\delta m = \frac{\alpha_{\text{EM}} M}{4\pi} f\left(\frac{m_Z}{M}\right) \tag{4.2}$$

where M is the mass of Φ and the functional form of f is given in appendix C.1. For $M \gg m_Z$, f has a simple form $f(r) \simeq 2\pi r$ and this gives a value $\delta m \approx .333$ GeV. This mass splitting, along with the W coupling, opens up a new decay channel for ϕ^- through a W boson, $\phi^- \to \phi^0 \ell \bar{\nu}_\ell$, with $\ell \in [e, \mu]$. Thus, ϕ^- has two decay channels and ϕ^0 has one. The decay widths are

$$\Gamma(\phi^- \to \ell_i \chi) = \frac{\lambda_i^2}{16\pi} M (1 - m_\chi^2/M^2)^2 \tag{4.3}$$

$$\Gamma(\phi^0 \to \nu_i \chi) = \frac{\lambda_i^2}{16\pi} M (1 - m_\chi^2/M^2)^2 \tag{4.4}$$

$$\Gamma(\phi^- \to \phi^0 e \bar{\nu}_e) = \frac{\alpha_{\text{EM}}^2}{30\pi s_W^4} \frac{\delta m^5}{m_W^4} \tag{4.5}$$

Because the muon mass is on the same order as δm, we cannot neglect it, and we do not have an analytic form for the width including the mass of the lepton. However, both decays through the W have an upper bound as $M \to \infty$, namely

$$\lim_{M\to\infty} \Gamma(\phi^- \to \phi^0 e \bar{\nu}_e) \simeq 1.04 \times 10^{-15} \text{ GeV} \tag{4.6}$$

$$\lim_{M\to\infty} \Gamma(\phi^- \to \phi^0 \mu \bar{\nu}_\mu) \simeq 6.42 \times 10^{-16} \text{ GeV} \tag{4.7}$$

Note also that the mass splitting is too small to meaningfully effect the decays to χ. Because we are once again in the freeze-in regime, λ can be very small, meaning that the three-body decay is the dominant decay process for ϕ^- in much of parameter space. This implies that almost all of the parameter space will feature decays within the detector. However, in the regions where the W decay dominates, we will have a disappearing track instead of a displaced lepton, because the lepton from this decay will be very soft.

The addition of ϕ^0 also opens new search channels with fewer final state leptons. In addition to the two lepton search in the RH model, we can also have single lepton final states, or we can pair produce ϕ^0, leading to an entirely invisible final state. In this case we could search for initial state radiation.

4.1.2 Right-Handed Quark Model.

$$\mathcal{L} \supset -\lambda_i \bar{\phi} \chi u_R^i + \text{c.c.} \tag{4.8}$$

The right handed quark model is again analogous to the right handed lepton model, however now ϕ both has color charge and electric charge ($Q_\phi = Q_u = 2/3$). For this model, in the prompt region of parameter space, instead of looking for a dilepton final state, we will be looking for a dijet final state. In the parts of parameter space where ϕ is long-lived, ϕ will form color neutral bound states known as R-hadrons. These states often arise in supersymmetric models, such as split SUSY, where the long-lived particle is the gluino. R-parity violating models can also lead to long lived squarks, which is essentially what ϕ is.

4.1.3 Left-Handed Quark Model.

$$\mathcal{L} \supset -\lambda_i \bar{\Phi} \chi Q_L^i + \text{c.c.} \tag{4.9}$$

For the left handed quark model Φ is again a doublet, with hypercharge $Y = 1/6$ to match Q_L. Now there will be an up type ϕ_u and a down type ϕ_d, with different electric charges as in the LH lepton model. We once again have a coupling with the W, and both components will have a mass splitting given by

$$\delta m = \frac{\alpha_{\text{EM}} M}{12\pi} f\left(\frac{m_Z}{M}\right) \tag{4.10}$$

or 1/3 the mass splitting in the LH lepton case. This means that the three body decay is again open, however, the mass splitting being much closer to the muon mass gives a phase space suppression to the decay to μ, making it essentially negligible compared to the decay to electrons. Otherwise the decay modes are similar to the LH lepton model. As for collider signals, unlike the LH lepton model, neither ϕ is invisible, so therefore our searches are primarily for dijets or R-hadrons, similar to the RH quark model.

CHAPTER V

CONCLUSIONS

5.1 Dependence of Dark Matter – Electron Scattering on the Galactic Dark Matter Velocity Distribution

In this work, we quantify the dependence of the observables of DM-electron scattering, namely the differential scattering rate and the cross section, on the uncertainties of the underlying DM halo velocity distribution. We consider three halo models: the SHM, the Tsallis model, and an empirical model. We study the effects of varying the astrophysical parameters within each model, and calculate the projected event rates and cross-section bounds. In addition, we give a brief overview of the measurements of the relevant astrophysical parameters and propose updated values for $v_0, v_{\rm esc}$, and $\rho_{\rm DM}$.

Ultimately, we find that the empirical model sets the strongest constraints, while the Tsallis model sets the weakest. When varying the halo models across the relevant astrophysical parameters, we find that v_0 is the most influential parameter in the cases of the SHM and Tsallis distributions, while p is the dominant parameter for the empirical model. For $m_\chi = 10$ (1000) MeV, the variation in v_0 leads to changes in the rate ranging from $\sim 15\%$ (0.03%) for $N_e = 1$ and $F_{\rm DM} = 1$ to $\sim 300\%$ (140%) for $N_e = 4$ and $F_{\rm DM} = (\alpha m_e/q)^2$. In the empirical model, the variation in p leads to changes in the rate ranging from $\sim 5\%$ (1%) for $N_e = 1$ and $F_{\rm DM} = 1$ to $\sim 500\%$ (240%) for $N_e = 4$ and $F_{\rm DM} = (\alpha m_e/q)^2$. Overall, the empirical model varies the most within the allowed intervals for its parameters, while the SHM varies the least. Across all three models we see a pattern according to which, the direct detection observables depend more on our choice of VDF and its associated parameters for the lower DM masses, higher threshold energies (N_e), and $F_{DM} \sim 1/q^2$, while the choice of the VDF has a weaker effect when increasing the DM mass, lowering the ionization threshold N_e and setting $F_{DM} = 1$. For all three models, updating the canonical value of the local DM density with a higher value, leads to a stronger bound on the projected cross section.

The sensitivity of DM-nuclear scattering to astrophysical uncertainties is well-known, and must be taken into account when interpreting the results of the direct detection experiments (see *e.g.* [225]). Our results quantify the sensitivity of DM-*electron* scattering observables to the astrophysical parameters, and highlight the importance of extracting accurate measurements for these parameters, aiming at a consistent interpretation of the relevant experimental efforts. Several proposals account for these astrophysics-driven uncertainties in the case of DM-nuclear scattering, ranging from marginalizing over astrophysical uncertainties [226], to presenting the results in a halo-independent manner [227–232]. We emphasize that similar techniques can be developed and applied in the context of DM-electron scattering interactions and are worthy of a dedicated study.

Once data from ongoing and upcoming DD experiments start flowing in, the emergence of a positive signal would mark the onset of the DM discovery mode. Such a development would necessitate/expand the design of statistically-robust analyses, allowing one to accurately reconstruct the properties of the DM particle, through the study of the available DD data [226, 233]. Once such analyses would be in place, one would be in position to ask how well the DM VDF can be determined, by performing various statistical tests with the potential to pin down the underlying DM halo model. Preliminary analyses along these lines show great promise for DM-electron scattering [234], and this direction warrants further exploration.

5.2 Interplay of Freeze-In and Freeze-Out: Lepton-Flavored Dark Matter and Muon Colliders

We initiated a detailed study of the freeze-in flavored DM setup in which flavored DM coupling to the slepton-like mediator is very small. We showed that the interplay of direct freeze-in and the mediator freeze-out gives rise to an interesting abundance calculation, such that the dark matter mass should be below a few TeV in order to avoid overclosing the universe. Combined with the existing collider and astrophysical bounds, this gives rise to a bounded viable parameter space for this model.

We also studied signals of our model at a future high energy Muon Collider (MuC). As a result of the feeble Yukawa coupling of DM, all signals of the model in a MuC originate from the on-shell pair production of the mediator. The range of mediator masses and lifetimes in the viable parameter space is such that we can have prompt, as well as various long-lived particle signals at a MuC. We divided our parameter space into two broad ranges according to the mediator's lifetime, namely prompt and LLP regions.

In the prompt decay region, we proposed a rudimentary analysis and identified the target systematics that ought to be achieved in order to discover our model at a MuC. Our analysis uses cuts on invariant leptonic system mass $m_{\ell\ell}$, missing transverse mass parameter M_{T2}, and the leptonic system transverse momentum $p_{T,\ell\ell}$. We found that in the part of the parameter space with prompt mediator decay, if systematic uncertainties are comparable or smaller than SM background, our proposed analysis can discover this model at effectively the entire kinematically-accessible parameter space.

For longer lifetimes, we will have a charged track in the detector which, depending on the lifetime, can either decay to a lepton and missing energy or decay outside the detector. While the SM background can be reduced away using quantities such as time-of-flight or anomalous ionization rate, detector response can give rise to an irreducible background. A proper study of these effects requires extensive simulations and is left for future works. In the absence of concrete simulations, here we reported the signal yield and various kinematics distributions. In particular, we showed that the displaced lepton distribution has a double-peak signature that could potentially be used for efficient background rejection. This feature appears as two large sets of signal events, produced through the two distinct channels (DY and VBF), in different detector components.

Our work can be extended in many directions. Foremost among them is a detailed study of the detector design that enables detailed studies of the background. Given the great reach of future MuCs in our model's parameter space, the universality of its production rate, and its theoretical motivation, we believe our model can serve as a motivated benchmark target for future studies on development of the detector by setting a target for systematics of such works.

Our analysis can also be repeated for other flavored DM models, *i.e.* mediators with same charges as other SM fermions. All these setups have the added bonus that the artificial alignment of the DM Yukawa and SM Yukawas in flavored DM models, required for evading bounds from flavor-changing neutral currents and lepton flavor violation, are completely avoided thanks to the feeble DM coupling. While the relic abundance calculation resembles the calculation here, we expect a different collider phenomenology for some of them thanks to their different production and decay channels.

Furthermore, as alluded to earlier, the muon PDF is not yet included in `MadGraph5`, thus we neglected its effect in the DY production channel. With the ever-growing interest in BSM signals at a MuC, it is interesting to work on proper embedding of this PDF in the event-generation pipeline.

It will also be interesting to consider signals of such models in other experiments, such as various astrophysical or direct detection searches. (See Refs. [245, 246] for a study of astrophysical bounds on a quark-flavored DM model in the freeze-in regime.) In particular, there is a large part of the parameter space inaccessible to colliders in foreseeable future, motivating searches in the aforementioned complementary fronts.

High energy MuCs are strongly motivated for their ability in probing different models of the Higgs boson UV-completion, flavorful new physics, and DM models. Our study outlines a simple and interesting DM model with unique signatures that can serve as a target for searches at a high energy MuC and inform its detector design.

APPENDIX A

SUPPLEMENTAL MATERIAL FOR DEPENDENCE OF DARK MATTER – ELECTRON SCATTERING ON THE GALACTIC DARK MATTER VELOCITY DISTRIBUTION

A.1 Tsallis Rate and Cross-Section Results

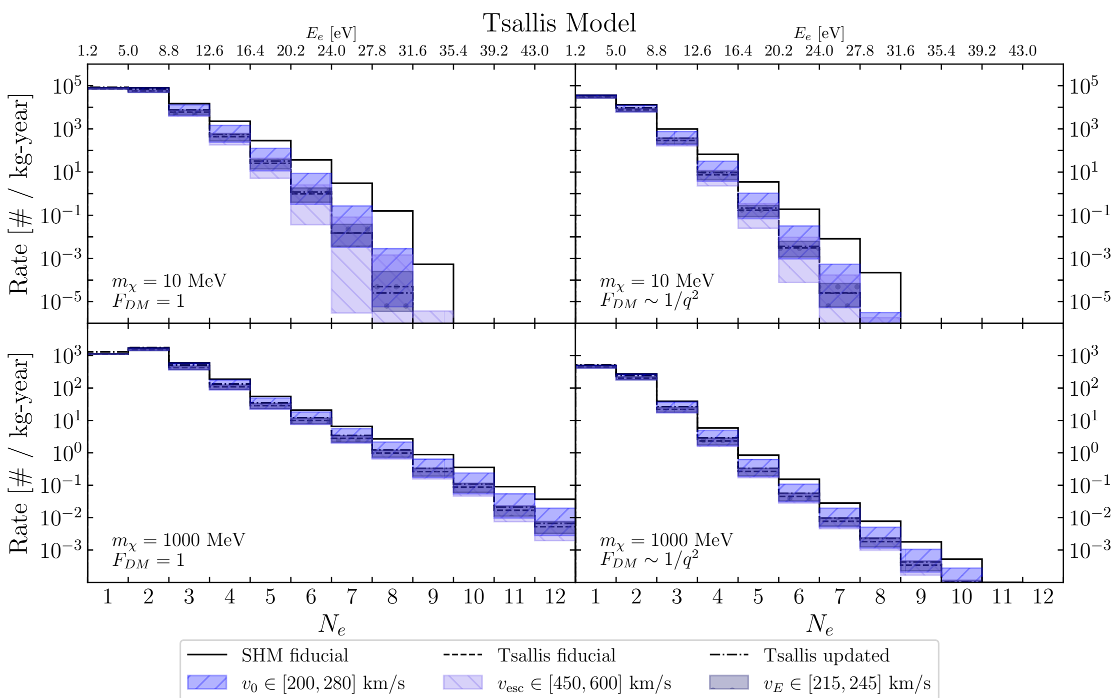

Figure A.1. Rate spectra for the Tsallis model at 1 kg-year exposure and $\overline{\sigma}_e = 10^{-37}$ cm^2 for a range of halo parameters, as a function of the number of observed electrons, N_e, and electron energy E_e. The rate for the Tsallis distribution with fiducial halo parameters is given by the black dashed line, while the rate for the updated halo parameters is given by the black dash-dotted line. For comparison, we show the rate for the SHM with fiducial halo parameters in the black solid line. The top (bottom) panels show the rate for $m_\chi = 10$ MeV ($m_\chi = 1$ GeV), and the left (right) panels for $F_{\rm DM} = 1$ ($F_{\rm DM} = (\alpha m_e/q)^2$).

In this appendix, we present the results for the Tsallis model in greater detail. In fig. A.1, we show the spectrum of events as a function of the electron energy E_e, for two DM form factors ($F_{\rm DM} = 1$ and $F_{\rm DM} = (\alpha m_e/q)^2$) and two

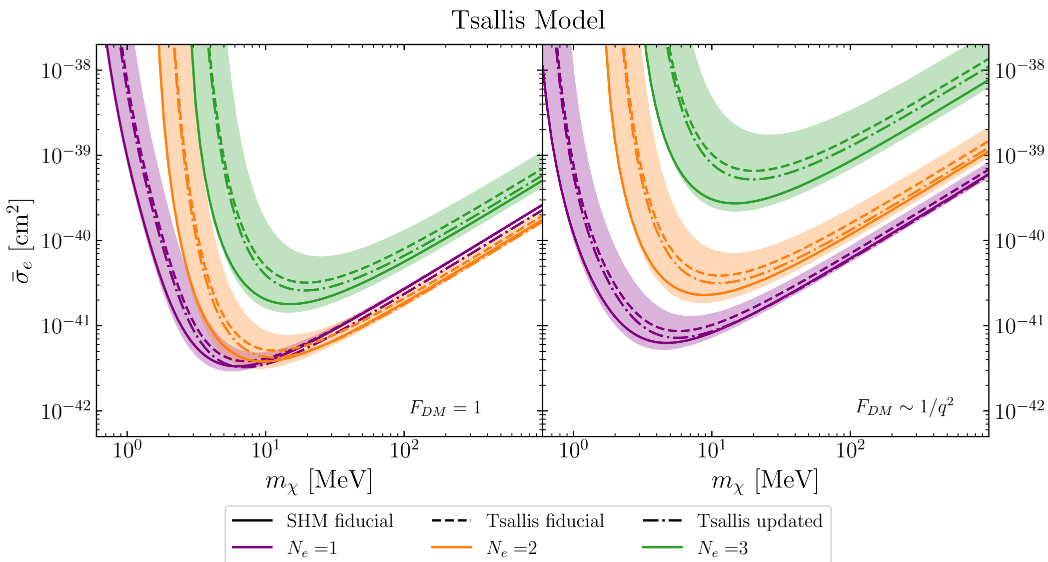

Figure A.2. Projected 95% C.L. cross-section reach for the Tsallis model, assuming 1 kg-year exposure and zero background events. The predictions for the $N_e = 1, 2, 3$ bins are given in purple, orange, and green respectively. The dashed curves are calculated using the fiducial values for the halo parameters, while the dash-dotted curves are calculated with the updated parameters. The bands denote the range of cross sections resulting from the variation of all the halo parameters within their allowed intervals. The solid curves for the SHM, evaluated at its fiducial halo parameters, are shown for comparison.

candidate masses (m_χ = 10 MeV and 1 GeV). The Tsallis distribution exhibits higher sensitivity to variations across its parameters, and especially $v_{\rm esc}$, as we move toward higher N_e bins and lower DM masses. The Tsallis model appears to be more sensitive when varied over its parameters, compared to the SHM.

In fig. A.2, we see the predicted 95% C.L. cross-section reach, assuming 1 kg-year exposure and no background events. Here we notice that the Tsallis model once again shows larger variation when varied across its parameters, compared with the SHM case, and when evaluated at the maximal values allowed for its associated parameters it can reach the fiducial SHM limits. As in the case of the SHM, we see that increases in DM mass lead to increased resistance to changes in the halo-model

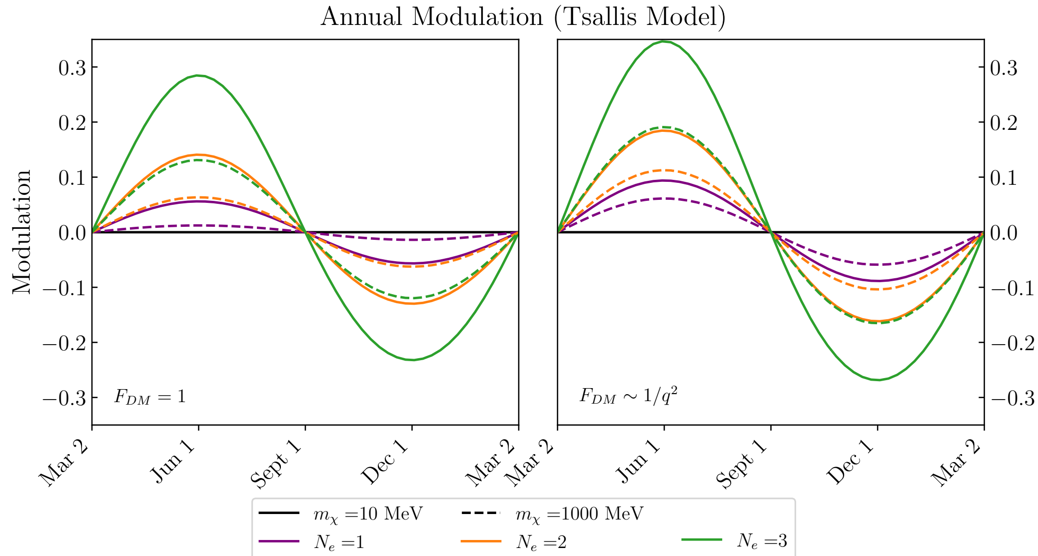

Figure A.3. Annual modulation of the scattering rate for the Tsallis distribution for $F_{\mathrm{DM}} = 1$ (left) and $F_{\mathrm{DM}} \propto 1/q^2$ (right) for two candidate masses $m_\chi = 10$ MeV (solid), 1 GeV (dashed) and $N_e = 1, 2, 3$ (purple, orange, green).

parameters, while increases in N_e make the cross section more susceptible to such changes.

In fig. A.3, we show the annual modulation for the Tsallis model. This distribution results in a larger annual modulation comparatively with the SHM. Like for the latter model, larger DM masses result in smaller modulation, as does the choice of the form factor for the heavy mediator, $F_{DM} = 1$.

A.2 Empirical Rate and Cross-Section Results

In this appendix, we present the results for the empirical model in more detail. In fig. A.4, we show the spectrum of events as a function of the electron energy E_e, for two DM form factors ($F_{\mathrm{DM}} = 1$ and $F_{\mathrm{DM}} = (\alpha m_e/q)^2$) and two candidate masses ($m_\chi = 10$ MeV and 1 GeV). As we saw previously for the SHM and the Tsallis distributions, the empirical model shows more sensitivity when varied across its parameters as we increase the ionization threshold N_e and decrease the DM mass, however now p is the strongest source of variance in *all* cases.

In fig. A.5, we see the predicted 95% C.L. cross-section reach, fixing the exposure at 1 kg-year and assuming zero background events. Here, the top edges of the color bands result from substituting the minimum allowed values for v_0, $v_{\rm esc}$, and v_E, while we have substituted the *maximum* value for the p exponent of the distribution, hence increasing p would lead to *weaker* bounds. Once again we see that the empirical model is affected more when varied across its parameters compared with the SHM and Tsallis distributions, and can well exceed the limits that could be set by either, depending on our choice of p. Results from the Eris simulation suite, that takes into account baryonic feedback effects, suggest a value for p (p=3) greater than the corresponding value inferred by its DM-only counterpart (p=1.5); the choice of the larger value would result in weaker bounds for the empirical model.

In fig. A.6, we show the annual modulation of the count rate for the empirical model. As we saw in the two bottom plots in fig. 7, the empirical model in general has a smaller modulation than the SHM, and follows the same trends as the SHM when it comes to the choice of the DM mass and form factor. Namely, larger masses result in smaller modulation, while a light mediator ($F_{DM} \sim 1/q^2$) would result in larger modulation. Although changes to the p parameter affect the empirical model strongly, we see that variance in v_E plays a minor role, as is the case for the other two velocity profiles.

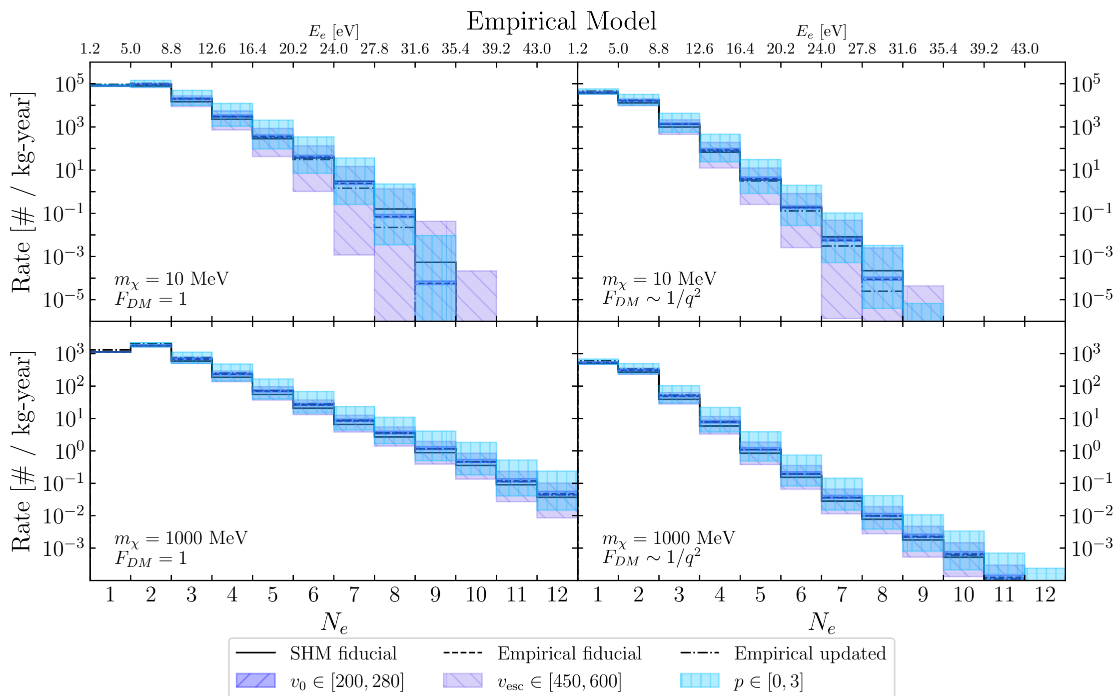

Figure A.4. Rate spectra for the empirical model at 1 kg-year exposure and $\overline{\sigma}_e = 10^{-37}$ cm^2 for a range of halo parameters, as a function of the number of observed electrons, N_e, and electron energy E_e. The rate for the empirical distribution with fiducial halo parameters is given by the black dashed line, while the rate for the updated halo parameters is given by the black dash-dotted line. For comparison, we show the rate for the SHM with fiducial halo parameters in the black solid line. The top (bottom) panels show the rate for $m_\chi = 10$ MeV ($m_\chi = 1$ GeV), and the left (right) panels for $F_{\rm DM} = 1$ ($F_{\rm DM} = (\alpha m_e/q)^2$).

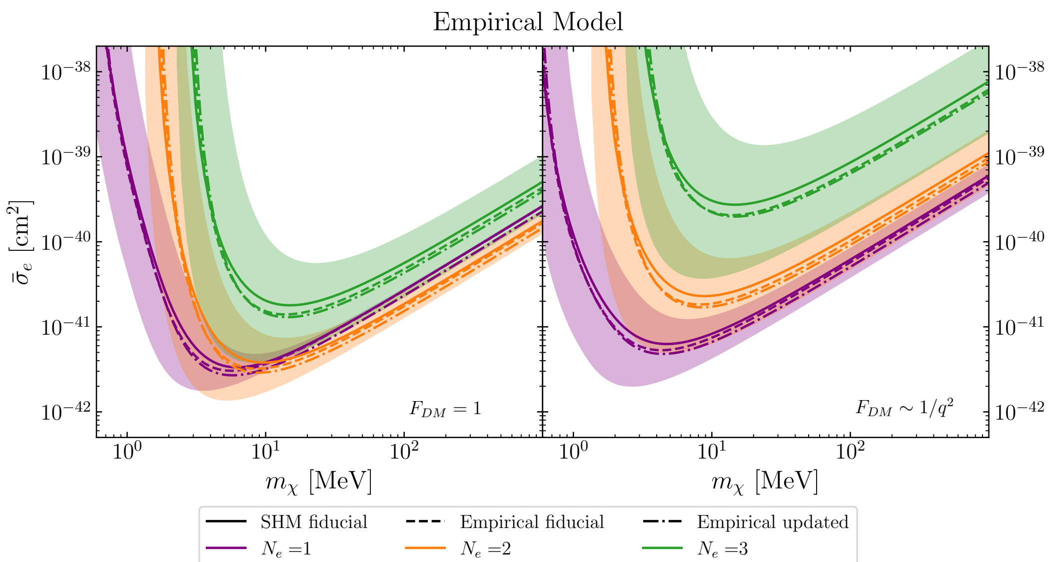

Figure A.5. Projected 95% C.L. cross-section reach for the empirical model, assuming 1 kg-year exposure and zero background events. The predictions for the $N_e = 1, 2, 3$ bins are given in purple, orange, and green respectively. The dashed curves are calculated using the fiducial values for the halo parameters, while the dash-dotted curves are calculated with the updated parameters. The bands denote the range of cross sections resulting from the variation of all the halo parameters within their allowed intervals. The solid curves for the SHM, evaluated at its fiducial halo parameters, are shown for comparison.

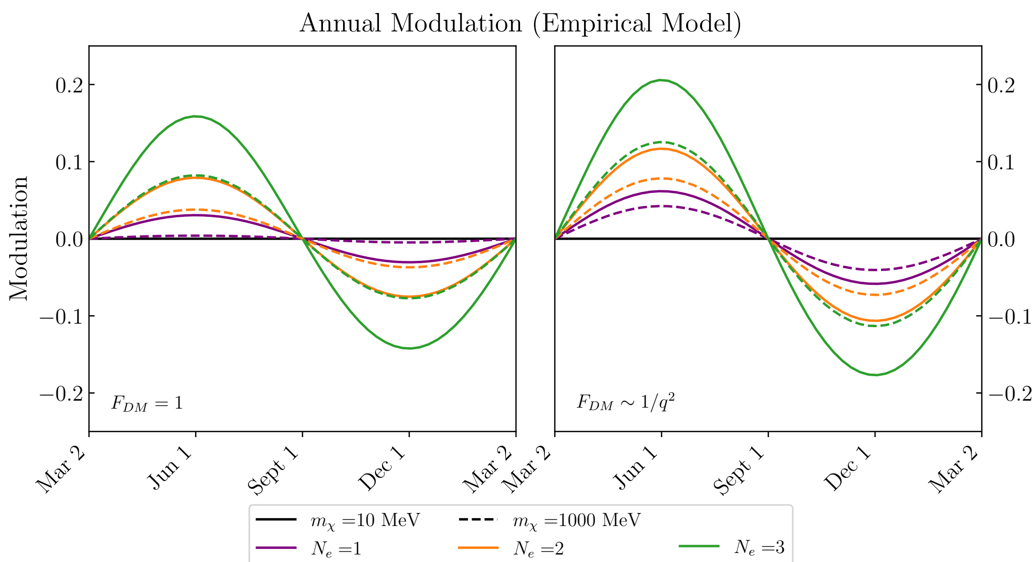

Figure A.6. Annual modulation of the scattering rate for the empirical distribution for $F_{\mathrm{DM}} = 1$ (left) and $F_{\mathrm{DM}} \propto 1/q^2$ (right) for two candidate masses $m_\chi = 10$ MeV (solid), 1 GeV (dashed) and $N_e = 1, 2, 3$ (purple, orange, green).

Tsallis Model (m_χ=10 MeV)

N_e	1		2		3		4	
F_{DM}	1	$(\alpha m_e/q)^2$	1	$(\alpha m_e/q)^2$	1	$(\alpha m_e/q)^2$	1	$(\alpha m_e/q)^2$
Fiducial	7.3×10^4	2.9×10^4	5.8×10^4	7.7×10^3	6.0×10^3	2.9×10^2	4.4×10^2	7.5
Updated	8.5×10^4	3.5×10^4	6.9×10^4	9.3×10^3	7.5×10^3	3.7×10^2	5.5×10^2	9.5
rel. diff.	0.16	0.18	0.20	0.21	0.25	0.26	0.27	0.27
$v_{0,min}$	7.0×10^4	2.7×10^4	4.9×10^4	6.1×10^3	4.1×10^3	1.8×10^2	2.4×10^2	3.7
$v_{0,max}$	8.0×10^4	3.7×10^4	8.1×10^4	1.3×10^4	1.3×10^4	7.6×10^2	1.4×10^3	32
rel. diff.	0.14	0.34	0.56	0.84	1.5	2.0	2.8	3.7
$v_{esc,min}$	7.1×10^4	2.7×10^4	5.0×10^4	6.1×10^3	3.8×10^3	1.6×10^2	1.8×10^2	2.3
$v_{esc,max}$	7.4×10^4	3.0×10^4	6.1×10^4	8.4×10^3	7.1×10^3	3.7×10^2	6.1×10^2	12
rel. diff.	0.045	0.11	0.19	0.30	0.55	0.72	0.99	1.3
$v_{E,min}$	6.8×10^4	2.6×10^4	4.9×10^4	6.3×10^3	4.4×10^3	2.0×10^2	2.8×10^2	4.4
$v_{E,max}$	7.6×10^4	3.2×10^4	6.5×10^4	8.9×10^3	7.4×10^3	3.8×10^2	6.0×10^2	11
rel. diff.	0.11	0.18	0.27	0.34	0.50	0.59	0.74	0.88

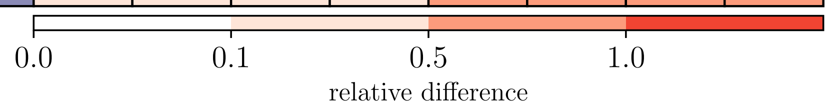

Tsallis Model (m_χ=1000 MeV)

N_e	1		2		3		4	
F_{DM}	1	$(\alpha m_e/q)^2$	1	$(\alpha m_e/q)^2$	1	$(\alpha m_e/q)^2$	1	$(\alpha m_e/q)^2$
Fiducial	1.1×10^3	4.4×10^2	1.5×10^3	2.0×10^2	4.3×10^2	22	1.1×10^2	2.3
Updated	1.3×10^3	5.1×10^2	1.8×10^3	2.4×10^2	5.1×10^2	27	1.3×10^2	2.9
rel. diff.	0.15	0.17	0.17	0.19	0.19	0.22	0.21	0.23
$v_{0,min}$	1.1×10^3	4.2×10^2	1.5×10^3	1.8×10^2	3.7×10^2	17	89	1.7
$v_{0,max}$	1.1×10^3	5.0×10^2	1.7×10^3	2.7×10^2	6.0×10^2	37	1.8×10^2	4.9
rel. diff.	0.0034	0.20	0.18	0.44	0.53	0.89	0.81	1.4
$v_{esc,min}$	1.1×10^3	4.2×10^2	1.5×10^3	1.8×10^2	3.7×10^2	17	88	1.6
$v_{esc,max}$	1.1×10^3	4.5×10^2	1.6×10^3	2.1×10^2	4.5×10^2	24	1.2×10^2	2.7
rel. diff.	0.0016	0.067	0.061	0.15	0.18	0.32	0.29	0.50
$v_{E,min}$	1.1×10^3	4.1×10^2	1.4×10^3	1.8×10^2	3.7×10^2	18	91	1.8
$v_{E,max}$	1.2×10^3	4.6×10^2	1.6×10^3	2.2×10^2	4.8×10^2	26	1.3×10^2	2.9
rel. diff.	0.027	0.12	0.13	0.21	0.25	0.35	0.32	0.46

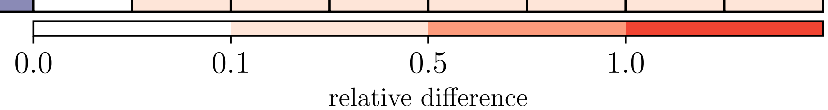

Table A.1. Expected number of events in 1 kg-year for various values of the Tsallis parameters $v_0, v_{\rm esc}$, and v_E, as well as the relative difference between the minimum and maximum values for each parameter, for a given N_e bin and DM form factor $F_{\rm DM}$. The top panel displays the results for $m_\chi = 10$ MeV, and the bottom panel for $m_\chi = 1$ GeV. The color scale indicates the size of the relative difference, with white (red) being the smallest (largest) relative difference.

Empirical Model (m_χ=10 MeV)

N_e	1		2		3		4	
F_{DM}	1	$(\alpha m_e/q)^2$	1	$(\alpha m_e/q)^2$	1	$(\alpha m_e/q)^2$	1	$(\alpha m_e/q)^2$
Fiducial	8.2×10^4	4.0×10^4	9.2×10^4	1.6×10^4	2.0×10^4	1.3×10^3	3.1×10^3	85
Updated	9.3×10^4	4.5×10^4	1.0×10^5	1.7×10^4	2.1×10^4	1.3×10^3	3.0×10^3	77
rel. diff.	0.14	0.12	0.11	0.084	0.050	0.011	-0.032	-0.094
$v_{0,min}$	8.1×10^4	3.9×10^4	8.9×10^4	1.5×10^4	1.9×10^4	1.2×10^3	2.8×10^3	78
$v_{0,max}$	8.4×10^4	4.2×10^4	9.9×10^4	1.8×10^4	2.2×10^4	1.5×10^3	3.6×10^3	1.0×10^2
rel. diff.	0.035	0.078	0.11	0.15	0.19	0.22	0.25	0.27
$v_{esc,min}$	7.6×10^4	3.2×10^4	6.8×10^4	9.7×10^3	8.8×10^3	4.5×10^2	7.2×10^2	12
$v_{esc,max}$	8.5×10^4	4.5×10^4	1.1×10^5	2.0×10^4	2.8×10^4	2.1×10^3	5.6×10^3	1.9×10^2
rel. diff.	0.11	0.31	0.41	0.66	0.95	1.3	1.6	2.1
$v_{E,min}$	7.9×10^4	3.8×10^4	8.4×10^4	1.4×10^4	1.7×10^4	1.1×10^3	2.3×10^3	60.
$v_{E,max}$	8.4×10^4	4.2×10^4	9.8×10^4	1.8×10^4	2.2×10^4	1.6×10^3	3.7×10^3	1.1×10^2
rel. diff.	0.061	0.12	0.15	0.22	0.30	0.38	0.46	0.59
p_{min}	9.3×10^4	5.7×10^4	1.4×10^5	3.2×10^4	5.0×10^4	4.3×10^3	1.2×10^4	4.6×10^2
p_{max}	7.5×10^4	3.3×10^4	6.8×10^4	1.0×10^4	10.0×10^3	5.7×10^2	1.1×10^3	24
rel. diff.	-0.22	-0.62	-0.81	-1.4	-2.0	-2.8	-3.7	-5.1

relative difference: 0.0 0.1 0.5 1.0

Empirical Model (m_χ=1000 MeV)

N_e	1		2		3		4	
F_{DM}	1	$(\alpha m_e/q)^2$	1	$(\alpha m_e/q)^2$	1	$(\alpha m_e/q)^2$	1	$(\alpha m_e/q)^2$
Fiducial	1.1×10^3	5.3×10^2	1.8×10^3	3.1×10^2	6.9×10^2	49	2.3×10^2	7.7
Updated	1.3×10^3	6.0×10^2	2.1×10^3	3.4×10^2	7.6×10^2	52	2.5×10^2	8.0
rel. diff.	0.15	0.13	0.14	0.11	0.11	0.077	0.080	0.034
$v_{0,min}$	1.1×10^3	5.3×10^2	1.8×10^3	3.0×10^2	6.7×10^2	46	2.2×10^2	7.2
$v_{0,max}$	1.1×10^3	5.5×10^2	1.9×10^3	3.3×10^2	7.4×10^2	54	2.5×10^2	8.7
rel. diff.	0.00029	0.051	0.045	0.097	0.11	0.15	0.15	0.20
$v_{esc,min}$	1.1×10^3	4.7×10^2	1.6×10^3	2.3×10^2	5.0×10^2	28	1.4×10^2	3.3
$v_{esc,max}$	1.1×10^3	5.7×10^2	1.9×10^3	3.6×10^2	8.0×10^2	63	3.0×10^2	12
rel. diff.	-0.0015	0.20	0.16	0.41	0.44	0.72	0.69	1.1
$v_{E,min}$	1.1×10^3	5.1×10^2	1.7×10^3	2.8×10^2	6.3×10^2	42	2.0×10^2	6.4
$v_{E,max}$	1.1×10^3	5.5×10^2	1.9×10^3	3.3×10^2	7.4×10^2	54	2.6×10^2	8.9
rel. diff.	0.0090	0.082	0.075	0.15	0.16	0.24	0.23	0.33
p_{min}	1.1×10^3	6.8×10^2	2.2×10^3	5.0×10^2	1.1×10^3	1.0×10^2	4.8×10^2	22
p_{max}	1.1×10^3	4.7×10^2	1.6×10^3	2.3×10^2	5.0×10^2	30.	1.4×10^2	3.8
rel. diff.	0.0075	-0.41	-0.32	-0.85	-0.88	-1.5	-1.4	-2.4

relative difference: 0.0 0.1 0.5 1.0

Table A.2. Expected number of events in 1 kg-year for various values of the empirical parameters $v_0, v_{\rm esc}, v_E$, and p, as well as the relative difference between the minimum and maximum values for each parameter, for a given N_e bin and DM form factor $F_{\rm DM}$. The top panel displays the results for $m_\chi = 10$ MeV, and the bottom panel for $m_\chi = 1$ GeV. The color scale indicates the size of the relative difference, with white (red) being the smallest (largest) relative difference.

APPENDIX B

SUPPLEMENTAL MATERIAL FOR INTERPLAY OF FREEZE-IN AND FREEZE-OUT: LEPTON-FLAVORED DARK MATTER AND MUON COLLIDERS

B.1 More Details on Relic Abundance Calculation

The relic abundance is directly related to the final χ yield, Y_χ^∞,

$$\Omega_\chi = 2m_\chi Y_\chi^\infty \frac{T_0^3}{30}\frac{8\pi G}{3H_0^2} \tag{B.1}$$

where $T_0 = 2.7255$ K and $H_0 = 100h$ km s^{-1} Mpc^{-1} are the temperature and Hubble constant today, respectively, and G is the gravitational constant. The factor of 2 accounts for χ and $\bar{\chi}$ both contributing to the final relic abundance. To be fully accurate, one should run the Boltzmann equation solver out to a sufficiently long time to obtain Y_χ^∞. However, we can also estimate this by noticing that Y_ϕ follows its freeze-out value until decaying, and Y_χ follows its freeze-in value (assuming Y_ϕ is in equilibrium) until ϕ decays. This information leads to the approximation that

$$Y_\chi^\infty \approx Y_\chi^{\text{FI}} + Y_\phi^{\text{FO}} \tag{B.2}$$

This approximation is useful because Y_ϕ^{FO} only depends on ϕ's mass, its couplings to the SM are fixed by its charge, and we can analytically calculate Y_χ^{FI}. We have checked that for the majority of the parameter space, this approximation has less than 1% error in the abundance calculation.

Starting with χ's Boltzmann equation we set $Y_\phi = Y_{\phi,\text{EQ}}$ and start from $Y_\chi = 0$. The Boltzmann equation for χ will be [117]

$$\frac{dY_\chi}{dx} = \frac{x^3}{H(m_\phi)}\frac{g_\phi 3\Gamma_{\phi\to\ell\chi}}{2\pi^2}K_1(x), \tag{B.3}$$

and we can simply integrate this from $x = 0$ to $x = \infty$ to find

$$Y_\chi^{\rm FI} = \frac{9 g_\phi \Gamma_{\phi\to\ell\chi}}{4\pi H(m_\phi)}, \tag{B.4}$$

with the decay width for $\phi \to \ell\chi$ given by

$$\Gamma_{\phi\to\ell\chi} = \frac{\lambda^2 m_\phi}{16\pi}\left(1 - \frac{m_\chi^2}{m_\phi^2}\right)^2. \tag{B.5}$$

We can plug in the approximation to the relic abundance to get

$$\Omega_\chi = 2m_\chi \left(Y_\chi^{\rm FI} + Y_\phi^{\rm FO}\right)\frac{T_0^3}{30}\frac{8\pi G}{3H_0^2} \tag{B.6}$$

To find the particular λ that gives the correct relic abundance $\Omega_\chi h^2 \approx 0.12$, we insert our expression for $Y_\chi^{\rm FI}$ and rearrange to get the Yukawa coupling that gives rise to the right relic abundance today

$$\lambda' = \frac{8\pi}{3(1 - m_\chi^2/m_\phi^2)}\sqrt{\frac{H(m_\phi)}{g_\phi m_\chi m_\phi}}\sqrt{\frac{45\Omega_\chi H_0^2}{8\pi G T_0^3} - m_\chi Y_\phi^{\rm FO}}. \tag{B.7}$$

We plot this quantity in Figure 10.

B.2 More Details on the Prompt Search

In this appendix we provide further results of our `MadGraph5` simulations that inform the cuts we used in our prompt region search.

To better determine what cuts can optimize the reach of a MuC collider, in Figure B.1 (Figure B.2) we show 2D histograms of the ratio of the signal (S) to square root of the background (B) for a few different ϕ masses and for center of mass energy of 3 TeV (10 TeV). These histograms inform us about what lower bounds on each kinematic parameter yields the best reach for any given mediator mass and collider's center of mass energy.

Based on these results, we can define a set of signal regions that together are sensitive to all values of m_ϕ. The definition of signal regions we use and their background B is included in Figure B.3.

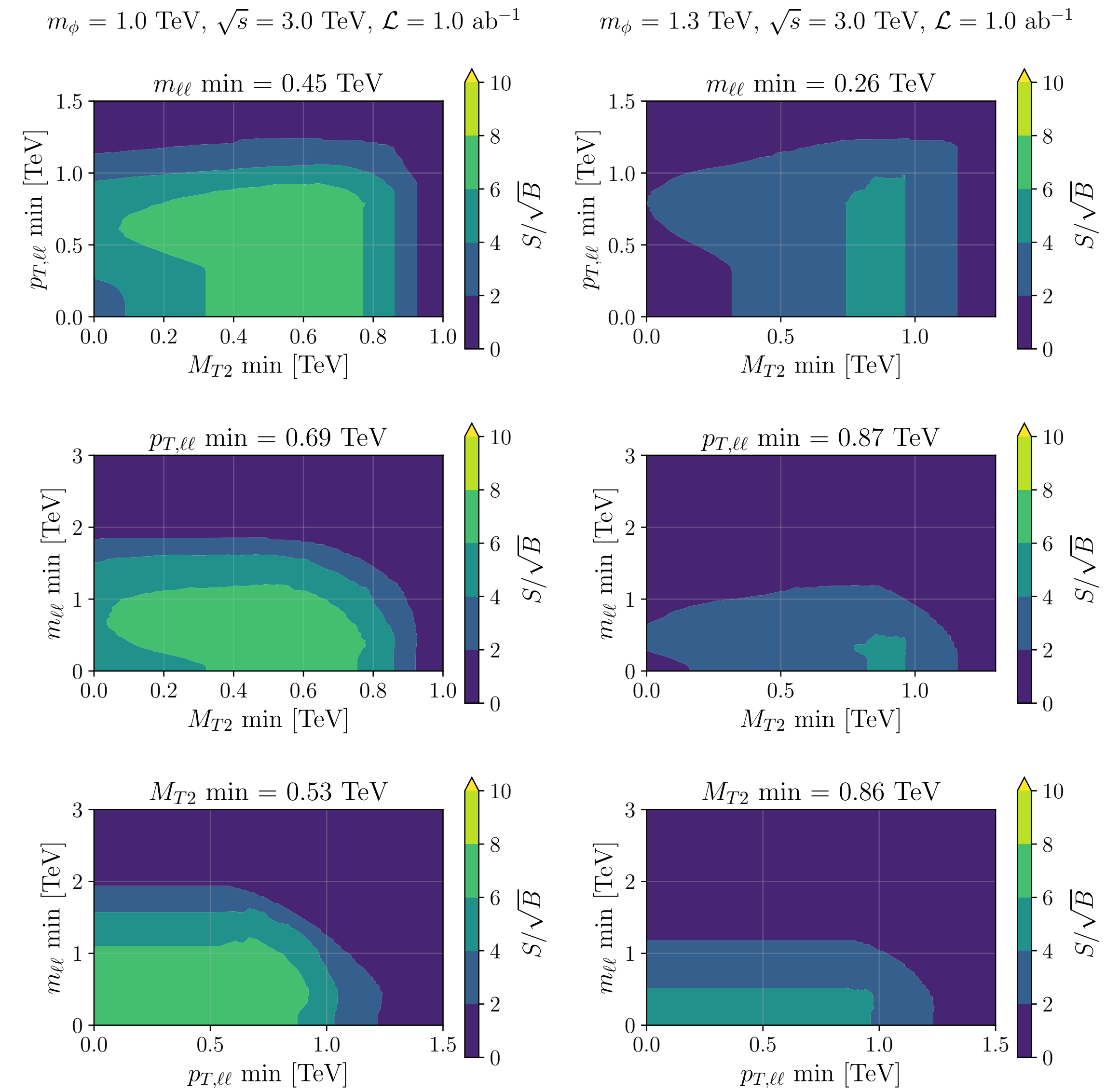

Figure B.1. Contours of significance of the signal (signal count S over square root of background $\sqrt{B}$) for different minimum values on each observable. We show the effect of cuts on events from two different ϕ masses, 1 TeV (**left**) and 1.3 TeV (**right**), at a MuC with center of mass energy of $\sqrt{s} = 3$ TeV. In each panel we show the effect of varying two cuts, while fixing the third one to the value that maximizes the significance. We find large significances are attainable. These figures inform the cuts used in definition of the signal regions.

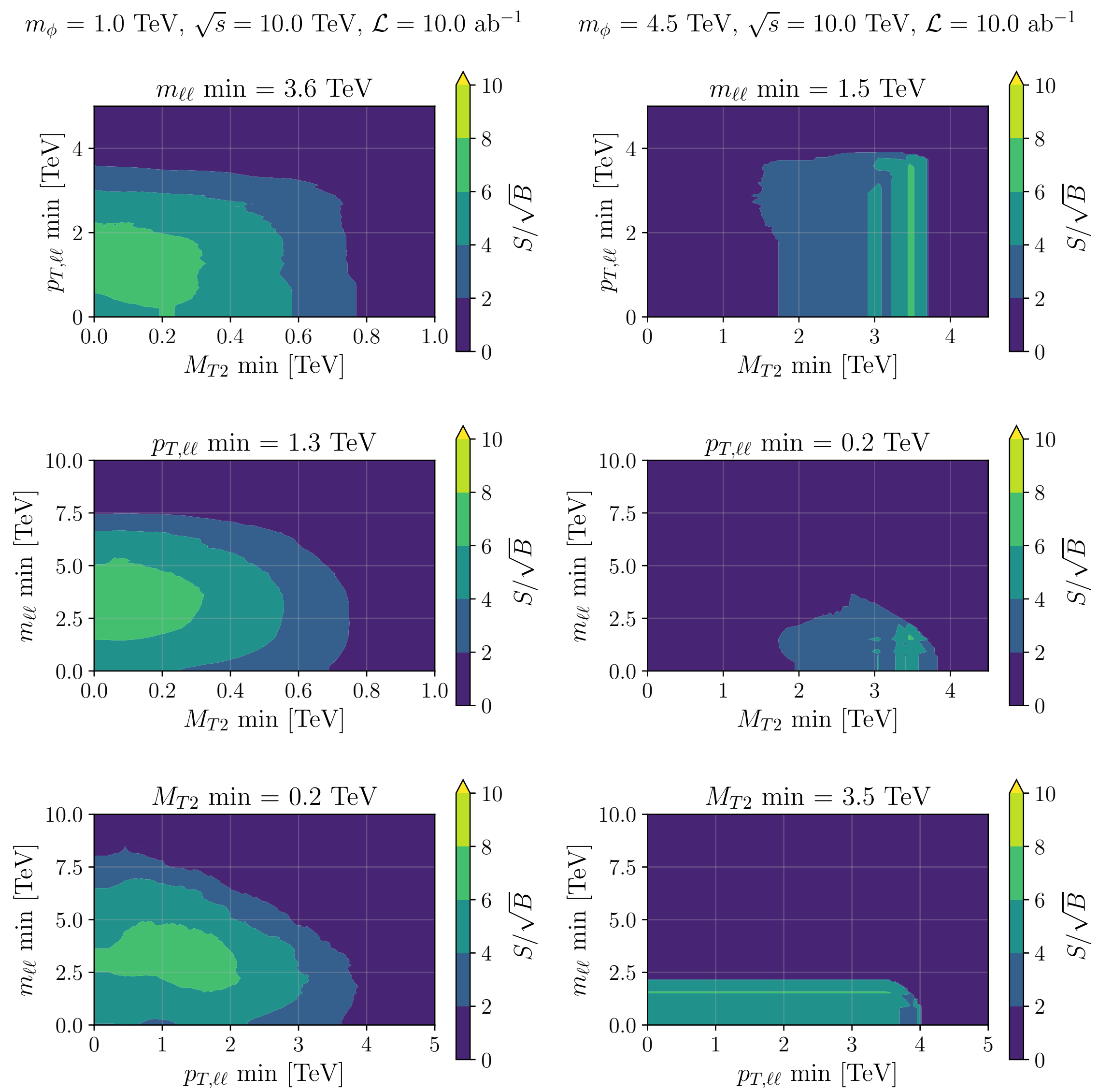

Figure B.2. Contours of significance of the signal (signal count S over square root of background $\sqrt{B}$) for different minimum values on each observable. This is the same as Figure B.1, but for ϕ masses 1 TeV (**left**) and 4.5 TeV (**right**), and at a MuC with center of mass energy of $\sqrt{s} = 10$ TeV. We find large significances are attainable. These figures inform the cuts used in definition of the signal regions.

$\sqrt{s} = 3$ TeV , $m_{\ell\ell} \geqslant 450$ GeV

SR 3 $p_\ell = 690$ GeV $M_{T_2} = 860$ GeV $B = 454$	SR 6 $p_\ell = 780$ GeV $M_{T_2} = 860$ GeV $B = 454$	SR 9 $p_\ell = 870$ GeV $M_{T_2} = 860$ GeV $B = 451$
SR 2 $p_\ell = 690$ GeV $M_{T_2} = 700$ GeV $B = 1223$	SR 5 $p_\ell = 780$ GeV $M_{T_2} = 700$ GeV $B = 1030$	SR 8 $p_\ell = 870$ GeV $M_{T_2} = 700$ GeV $B = 782$
SR 1 $p_\ell = 690$ GeV $M_{T_2} = 530$ GeV $B = 2310$	SR 4 $p_\ell = 780$ GeV $M_{T_2} = 530$ GeV $B = 1652$	SR 7 $p_\ell = 870$ GeV $M_{T_2} = 530$ GeV $B = 1147$

$\sqrt{s} = 10$ TeV , $m_{\ell\ell} \geqslant 3600$ GeV

SR 3 $p_\ell = 1300$ GeV $M_{T_2} = 3500$ GeV $B = 20$	SR 6 $p_\ell = 750$ GeV $M_{T_2} = 3500$ GeV $B = 20$	SR 9 $p_\ell = 200$ GeV $M_{T_2} = 3500$ GeV $B = 20$
SR 2 $p_\ell = 1300$ GeV $M_{T_2} = 1800$ GeV $B = 1385$	SR 5 $p_\ell = 750$ GeV $M_{T_2} = 1800$ GeV $B = 1385$	SR 8 $p_\ell = 200$ GeV $M_{T_2} = 1800$ GeV $B = 1385$
SR 1 $p_\ell = 1300$ GeV $M_{T_2} = 200$ GeV $B = 7931$	SR 4 $p_\ell = 750$ GeV $M_{T_2} = 200$ GeV $B = 19738$	SR 7 $p_\ell = 200$ GeV $M_{T_2} = 200$ GeV $B = 35079$

$\sqrt{s} = 3$ TeV , $m_{\ell\ell} \geqslant 360$ GeV

SR 12 $p_\ell = 690$ GeV $M_{T_2} = 860$ GeV $B = 521$	SR 15 $p_\ell = 780$ GeV $M_{T_2} = 860$ GeV $B = 521$	SR 18 $p_\ell = 870$ GeV $M_{T_2} = 860$ GeV $B = 518$
SR 11 $p_\ell = 690$ GeV $M_{T_2} = 700$ GeV $B = 1392$	SR 14 $p_\ell = 780$ GeV $M_{T_2} = 700$ GeV $B = 1185$	SR 17 $p_\ell = 870$ GeV $M_{T_2} = 700$ GeV $B = 915$
SR 10 $p_\ell = 690$ GeV $M_{T_2} = 530$ GeV $B = 2647$	SR 13 $p_\ell = 780$ GeV $M_{T_2} = 530$ GeV $B = 1913$	SR 16 $p_\ell = 870$ GeV $M_{T_2} = 530$ GeV $B = 1347$

$\sqrt{s} = 10$ TeV , $m_{\ell\ell} \geqslant 2600$ GeV

SR 12 $p_\ell = 1300$ GeV $M_{T_2} = 3500$ GeV $B = 20$	SR 15 $p_\ell = 750$ GeV $M_{T_2} = 3500$ GeV $B = 20$	SR 18 $p_\ell = 200$ GeV $M_{T_2} = 3500$ GeV $B = 20$
SR 11 $p_\ell = 1300$ GeV $M_{T_2} = 1800$ GeV $B = 2329$	SR 14 $p_\ell = 750$ GeV $M_{T_2} = 1800$ GeV $B = 2329$	SR 17 $p_\ell = 200$ GeV $M_{T_2} = 1800$ GeV $B = 2329$
SR 10 $p_\ell = 1300$ GeV $M_{T_2} = 200$ GeV $B = 15060$	SR 13 $p_\ell = 750$ GeV $M_{T_2} = 200$ GeV $B = 35963$	SR 16 $p_\ell = 200$ GeV $M_{T_2} = 200$ GeV $B = 55882$

$\sqrt{s} = 3$ TeV , $m_{\ell\ell} \geqslant 260$ GeV

SR 21 $p_\ell = 690$ GeV $M_{T_2} = 860$ GeV $B = 594$	SR 24 $p_\ell = 780$ GeV $M_{T_2} = 860$ GeV $B = 594$	SR 27 $p_\ell = 870$ GeV $M_{T_2} = 860$ GeV $B = 588$
SR 20 $p_\ell = 690$ GeV $M_{T_2} = 700$ GeV $B = 1579$	SR 23 $p_\ell = 780$ GeV $M_{T_2} = 700$ GeV $B = 1357$	SR 26 $p_\ell = 870$ GeV $M_{T_2} = 700$ GeV $B = 1049$
SR 19 $p_\ell = 690$ GeV $M_{T_2} = 530$ GeV $B = 3079$	SR 22 $p_\ell = 780$ GeV $M_{T_2} = 530$ GeV $B = 2243$	SR 25 $p_\ell = 870$ GeV $M_{T_2} = 530$ GeV $B = 1582$

$\sqrt{s} = 10$ TeV , $m_{\ell\ell} \geqslant 990$ GeV

SR 21 $p_\ell = 1300$ GeV $M_{T_2} = 3500$ GeV $B = 20$	SR 24 $p_\ell = 750$ GeV $M_{T_2} = 3500$ GeV $B = 20$	SR 27 $p_\ell = 200$ GeV $M_{T_2} = 3500$ GeV $B = 20$
SR 20 $p_\ell = 1300$ GeV $M_{T_2} = 1800$ GeV $B = 3112$	SR 23 $p_\ell = 750$ GeV $M_{T_2} = 1800$ GeV $B = 3112$	SR 26 $p_\ell = 200$ GeV $M_{T_2} = 1800$ GeV $B = 3112$
SR 19 $p_\ell = 1300$ GeV $M_{T_2} = 200$ GeV $B = 28814$	SR 22 $p_\ell = 750$ GeV $M_{T_2} = 200$ GeV $B = 70299$	SR 25 $p_\ell = 200$ GeV $M_{T_2} = 200$ GeV $B = 98170$

Figure B.3. Signal regions (SRs) used in our proposed search for $\sqrt{s} = 3$ TeV (**left**) and for $\sqrt{s} = 10$ TeV (**right**). The cuts used on each kinematic variable and the SM background in each region is reported. Determination of the cuts are informed by the most sensitive cuts on various extreme masses in the parameter space from Eqs. (3.7)–(3.10).

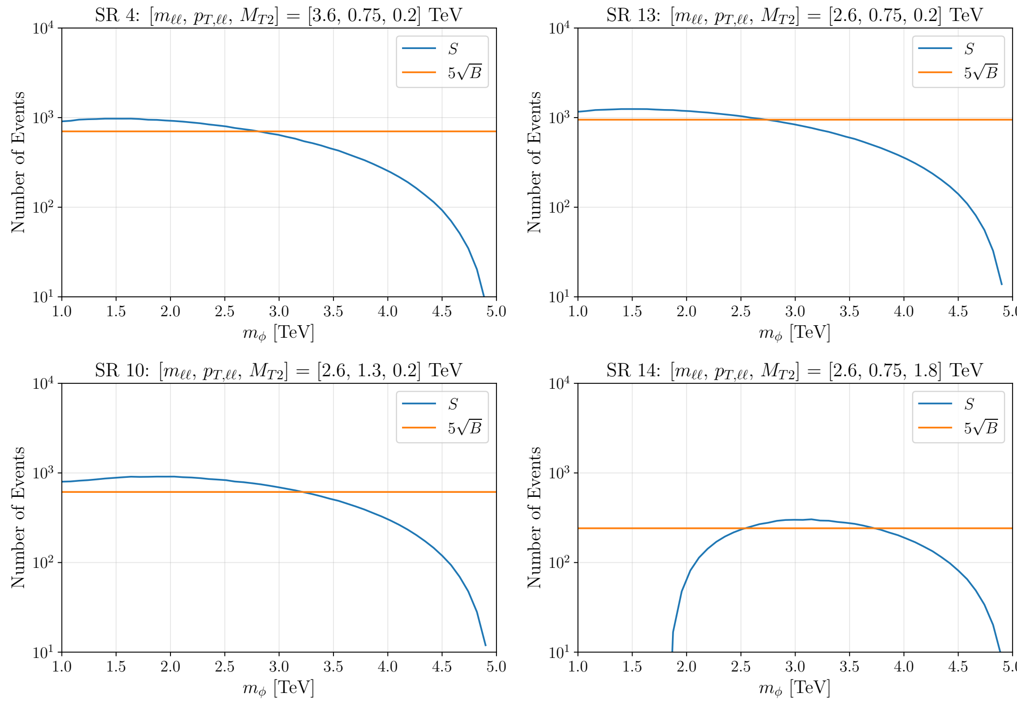

Figure B.4. Signal yield and the SM background of four sample signal regions with similar cuts, for different mediator masses. For each mass if a signal region has $S \geqslant 5\sqrt{B}$ signal events it can give rise to a discovery (neglecting systematics). We find that the M_{T2} cut controls the lowest mediator mass each signal region is sensitive too. Different $m_{\ell\ell}$ cuts affect the total number of events, while leaving the overall dependence on mediator mass unchanged. Comparing the signal regions with similar cuts we find that increasing the $p_{T,\ell\ell}$ cut shifts the signal distribution to higher ϕ masses.

To further illustrate the effect of each cut as a function of ϕ mass, in Figure B.4 we show the signal yield and the background for four sample signal regions with very similar cuts. These figures indicate that an M_{T2} cut is the lower bound on the mediator masses that populate a signal region, as expected [261]. The $p_{T,\ell\ell}$ and $m_{\ell\ell}$ cuts also reduce the SM and total signal yield in a signal region. Increasing the $p_{T,\ell\ell}$ cut shifts the distribution to higher m_ϕ masses as well.

B.3 More Details on the LLP Search

For completeness, in this appendix we include the 2D histograms of events in different kinematic observables in the LLP search. In particular, in Figure B.5 (Figure B.6) we show the 2D histograms of the distribution of events in the transverse distance $L(t = \gamma\tau_\phi)/\tau_\phi$ and their pseudorapidity η (their $\beta\gamma$), for a few mass points in the parameter space. The double-peak feature in Figures 18-21 are still visible here as well. The figure also shows that the smaller the mediator mass, the more separated in L/τ_ϕ the two peaks in the distribution.

Figure B.5 also reiterates the concentration of events at small $|\eta|$ values. This allows us to introduce stringent cuts on this variable to cut down the SM background, while preserving majority of signal events. The fact that the DY-generated events are more concentrated at smaller $|\eta|$ values is also an underlying cause of the separation of the cluster of events from different channels in Figures 22–25.

In Figures B.7 and B.8 we show the maximum number of decays across different detector segments. To make these plots, for each point in the parameter space we simply report the maximum event count from among all panels in Figures 22–25. We find that for most points in the parameter space we have at least $10^3 - 10^4$ events in at least one part of the detector (including events that are detector stable and give rise to stable charged tracks).

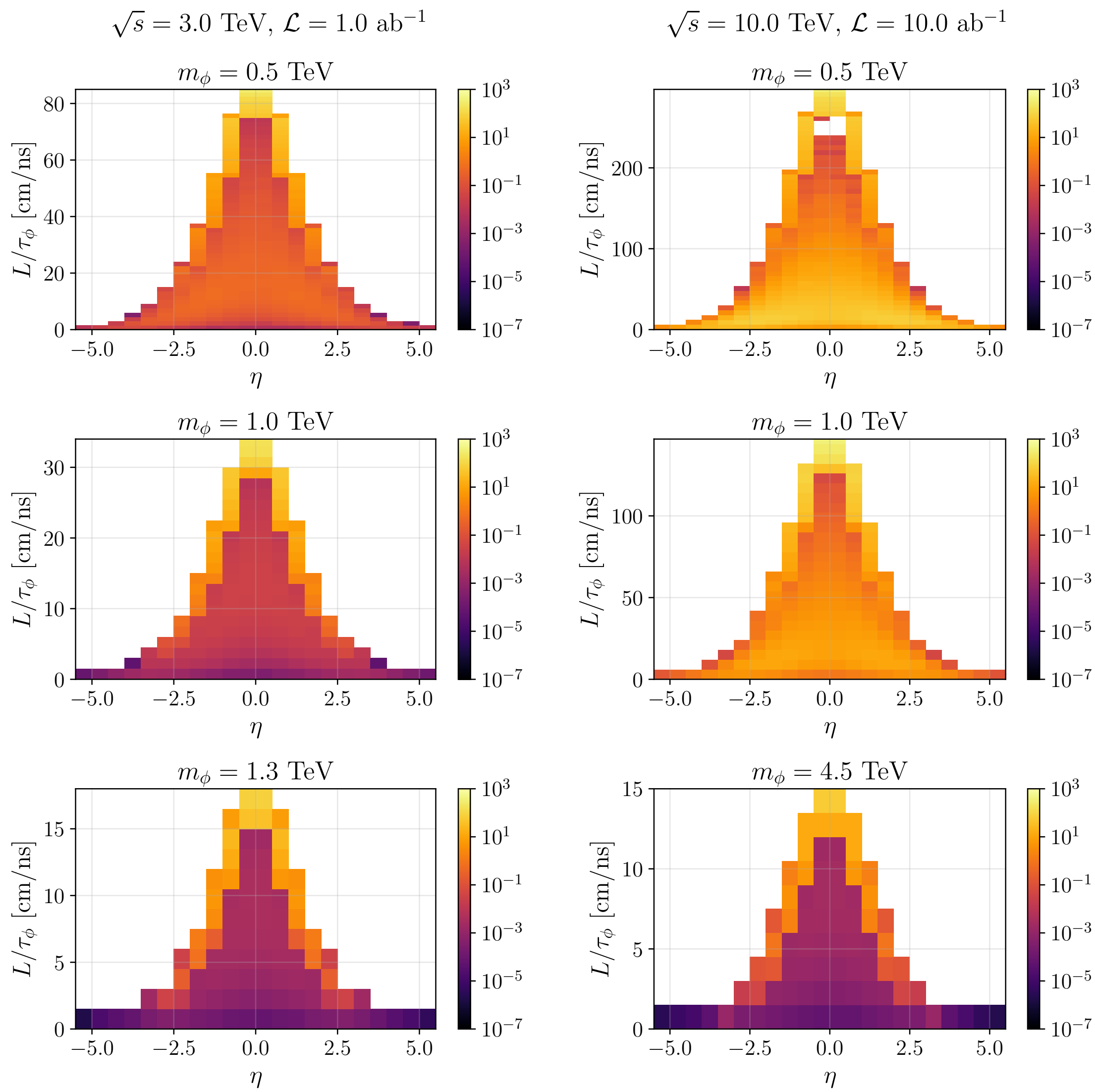

Figure B.5. Joint distribution of events in $\eta \quad - \quad L/\tau_\phi$ for three different mediator masses (different rows) at a 3 TeV MuC (**left**) or a 10 TeV MuC (**right**). The bin sizes are all 0.5 for η and 1.5 cm/ns for L/τ_ϕ (except for $\sqrt{s} = 10$ TeV, $m_\phi = 0.5$ and 1 TeV where they are 6 cm/ns). Events at the largest L/τ_ϕ values are due to the DY initial channel. The double-peak feature in the distribution (at large and small L values) is manifested as well.

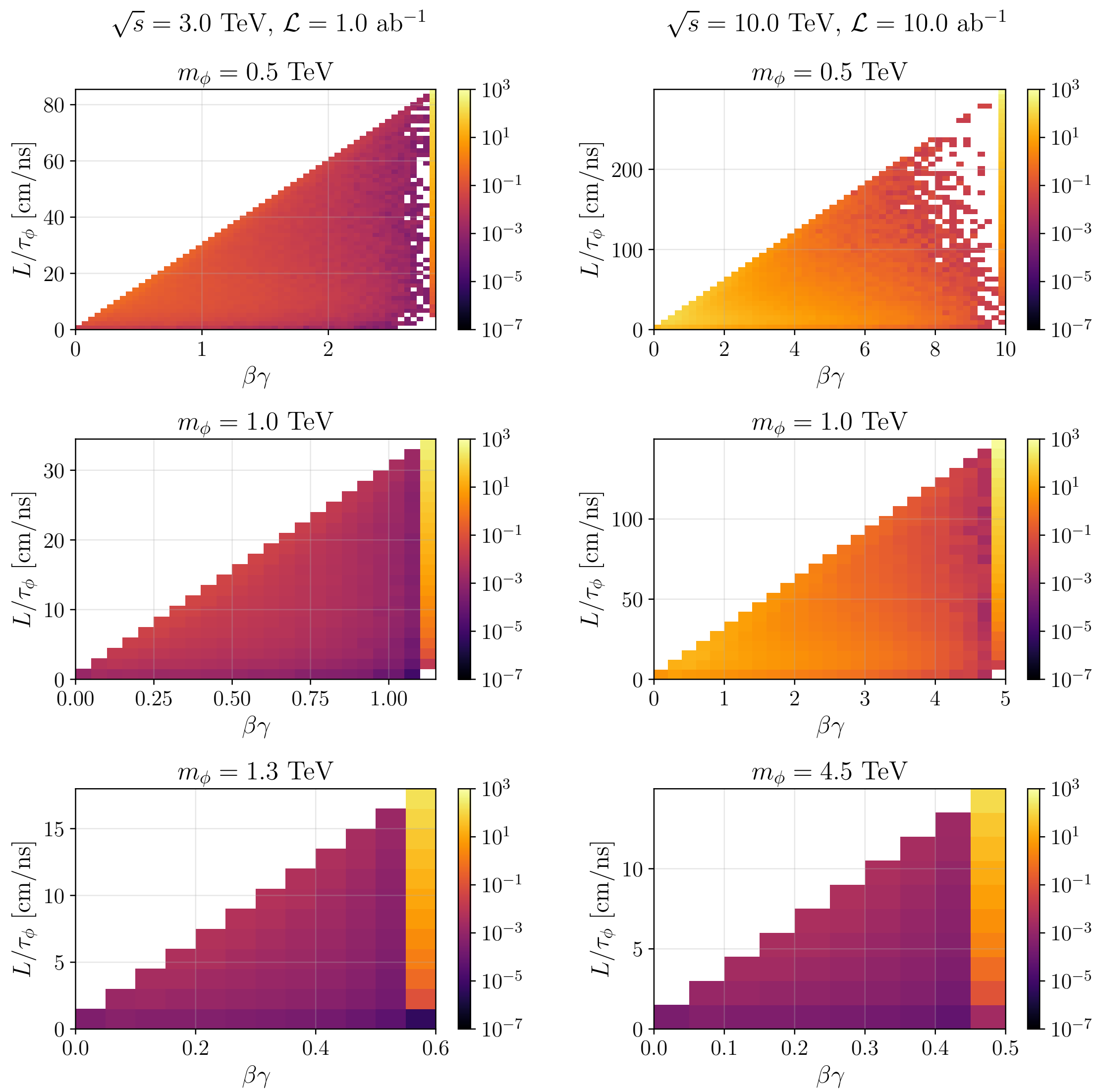

Figure B.6. Joint distribution of events in $\beta\gamma - L/\tau_\phi$ for three different mediator masses (different rows) at a 3 TeV MuC (**left**) or a 10 TeV MuC (**right**). Bin sizes are $(L/\tau_\phi,\, \beta\gamma) = (1.5$ cm/ns, $0.05)$ (except $\sqrt{s} = 10$ TeV, $m_\phi = 0.5$ and 1 TeV where they are $(L/\tau_\phi,\, \beta\gamma) = (6$ cm/ns, $0.2)$). Events at the largest L/τ_ϕ values are due to the DY initial channel. The double-peak feature in the distribution (at large and small L values) is manifested as well.

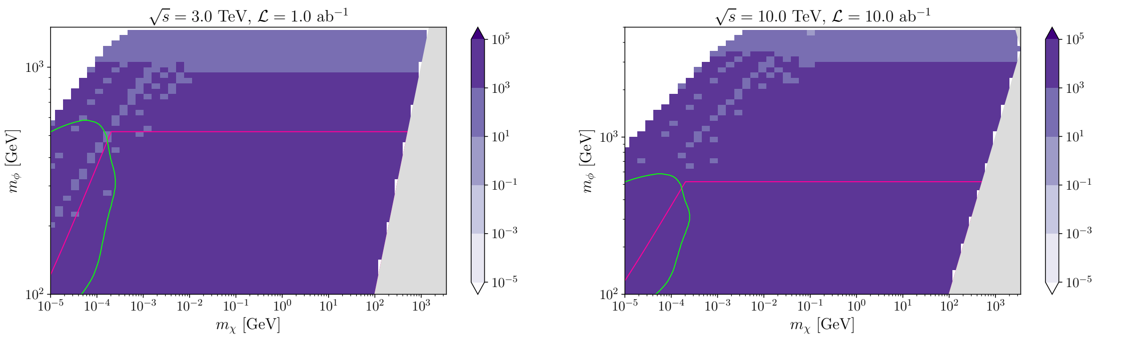

Figure B.7. Maximum rate of displaced leptons across different detector regions or stable charged tracks for every point in the parameter space in a 3 TeV (**left**) and a 10 TeV (**right**) MuC. The region below the green (pink) line is already ruled out by the LHC search in Ref. [1] (Ref. [2]).

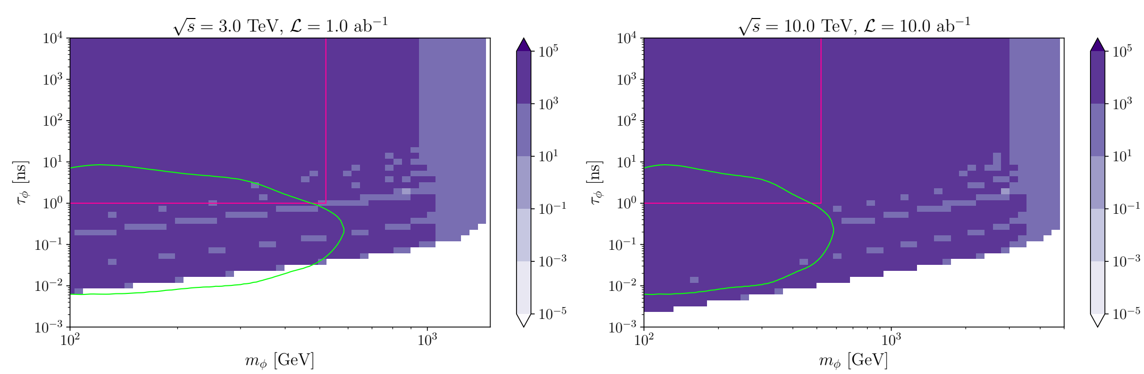

Figure B.8. Similar to Figure B.7 but on the plane of m_ϕ-τ_ϕ instead. The region below the green (pink) line is already ruled out by the LHC search in Ref. [1] (Ref. [2]).

APPENDIX C

SUPPLEMENTAL MATERIAL FOR MORE FLAVORED DARK MATTER MODELS AT MUON COLLIDERS

C.1 Explicit Formulas for Mass Splitting

The mass difference induced by loops of SM gauge bosons between two components of a new doublet (with hypercharge Y) and component electric charges Q and Q' is [270]

$$M_Q - M_{Q'} = \frac{\alpha_2 M}{4\pi}\left[(Q^2 - Q'^2)s_W^2 f\left(\frac{m_Z}{M}\right) + (Q-Q')(Q+Q'-2Y)\left[f\left(\frac{m_W}{M}\right) - f\left(\frac{m_Z}{M}\right)\right]\right] \tag{C.1}$$

where $\alpha_2 = \alpha/s_W^2$, and for scalars

$$f(r) = -\frac{r}{4}\left[2r^2\ln r + (r^2-4)^{3/2}\ln A(r)\right] \tag{C.2}$$

with

$$A(r) = \frac{1}{2}(r^2 - 2 - r\sqrt{r^2-4}) \tag{C.3}$$

Bibliography

[1] **ATLAS** Collaboration, G. Aad *et al.*, "Search for Displaced Leptons in $\sqrt{s} = 13$ TeV pp Collisions with the ATLAS Detector," *Phys. Rev. Lett.* **127** no. 5, (2021) 051802, `arXiv:2011.07812 [hep-ex]`.

[2] **CMS** Collaboration, "Search for heavy long-lived charged particles with large ionization energy loss in proton-proton collisions at $\sqrt{s} = 13$ TeV," tech. rep., CERN, Geneva, 2024. `https://cds.cern.ch/record/2893595`.

[3] J. Alwall, M. Herquet, F. Maltoni, O. Mattelaer, and T. Stelzer, "MadGraph 5 : Going Beyond," *JHEP* **06** (2011) 128, `arXiv:1106.0522 [hep-ph]`.

[4] **Muon Collider** Collaboration, N. Bartosik *et al.*, "Simulated Detector Performance at the Muon Collider," `arXiv:2203.07964 [hep-ex]`.

[5] X. Fan, T. G. Myers, B. A. D. Sukra, and G. Gabrielse, "Measurement of the Electron Magnetic Moment," *Phys. Rev. Lett.* **130** no. 7, (2023) 071801, `arXiv:2209.13084 [physics.atom-ph]`.

[6] **ATLAS** Collaboration, G. Aad *et al.*, "Observation of a new particle in the search for the Standard Model Higgs boson with the ATLAS detector at the LHC," *Phys. Lett. B* **716** (2012) 1–29, `arXiv:1207.7214 [hep-ex]`.

[7] **CMS** Collaboration, S. Chatrchyan *et al.*, "Observation of a New Boson at a Mass of 125 GeV with the CMS Experiment at the LHC," *Phys. Lett. B* **716** (2012) 30–61, `arXiv:1207.7235 [hep-ex]`.

[8] M. Schumann, "Direct detection of wimp dark matter: concepts and status," *Journal of Physics G: Nuclear and Particle Physics* **46** no. 10, (Aug., 2019) 103003. http://dx.doi.org/10.1088/1361-6471/ab2ea5.

[9] J. H. Oort, "The force exerted by the stellar system in the direction perpendicular to the galactic plane and some related problems," *Bulletin of the Astronomical Institutes of the Netherlands* **6** (Aug., 1932) 249.

[10] F. Zwicky, "Die Rotverschiebung von extragalaktischen Nebeln," *Helv. Phys. Acta* **6** (1933) 110–127.

[11] V. C. Rubin, W. K. Ford, Jr., and N. Thonnard, "Extended rotation curves of high-luminosity spiral galaxies. IV. Systematic dynamical properties, Sa through Sc," *Astrophys. J. Lett.* **225** (1978) L107–L111.

[12] R. Massey, T. Kitching, and J. Richard, "The dark matter of gravitational lensing," *Rept. Prog. Phys.* **73** (2010) 086901, arXiv:1001.1739 [astro-ph.CO].

[13] S. Dodelson, *Modern Cosmology*. Academic Press, Amsterdam, 2003.

[14] **Planck** Collaboration, P. A. R. Ade *et al.*, "Planck 2015 results. XIII. Cosmological parameters," *Astron. Astrophys.* **594** (2016) A13, arXiv:1502.01589 [astro-ph.CO].

[15] C. Pérez de los Heros, "Status, Challenges and Directions in Indirect Dark Matter Searches," *Symmetry* **12** no. 10, (2020) 1648, arXiv:2008.11561 [astro-ph.HE].

[16] A. Drukier and L. Stodolsky, "Principles and Applications of a Neutral Current Detector for Neutrino Physics and Astronomy," *Phys. Rev. D* **30** (1984) 2295.

[17] M. W. Goodman and E. Witten, "Detectability of Certain Dark Matter Candidates," *Phys. Rev. D* **31** (1985) 3059.

[18] S. P. Ahlen, F. T. Avignone, R. L. Brodzinski, A. K. Drukier, G. Gelmini, and D. N. Spergel, "Limits on Cold Dark Matter Candidates from an Ultralow Background Germanium Spectrometer," *Phys. Lett. B* **195** (1987) 603–608.

[19] A. K. Drukier, K. Freese, and D. N. Spergel, "Detecting cold dark-matter candidates," *Physical Review D* **33** no. 12, (1986) 3495.

[20] R. Essig *et al.*, "Snowmass2021 Cosmic Frontier: The landscape of low-threshold dark matter direct detection in the next decade," in *Snowmass 2021*. 3, 2022. `arXiv:2203.08297 [hep-ph]`.

[21] **CDF** Collaboration, F. Abe *et al.*, "Observation of top quark production in $\bar{p}p$ collisions," *Phys. Rev. Lett.* **74** (1995) 2626–2631, `arXiv:hep-ex/9503002`.

[22] **D0** Collaboration, S. Abachi *et al.*, "Observation of the top quark," *Phys. Rev. Lett.* **74** (1995) 2632–2637, `arXiv:hep-ex/9503003`.

[23] L. Di Lella and C. Rubbia, "The Discovery of the W and Z Particles," *Adv. Ser. Direct. High Energy Phys.* **23** (2015) 137–163.

[24] S. Gourlay *et al.*, "Snowmass'21 Accelerator Frontier Report," `arXiv:2209.14136 [physics.acc-ph]`.

[25] H. Al Ali *et al.*, "The muon Smasher's guide," *Rept. Prog. Phys.* **85** no. 8, (2022) 084201, `arXiv:2103.14043 [hep-ph]`.

[26] **P5** Collaboration, S. Asai *et al.*, "Pathways to Innovation and Discovery in Particle Physics: Report of the 2023 Particle Physics Project Prioritization Panel (P5),".

[27] N. Bozorgnia, F. Calore, M. Schaller, M. Lovell, G. Bertone, C. S. Frenk, R. A. Crain, J. F. Navarro, J. Schaye, and T. Theuns, "Simulated Milky Way analogues: implications for dark matter direct searches," *JCAP* **05** (2016) 024, `arXiv:1601.04707 [astro-ph.CO]`.

[28] A. Eddington, "The distribution of stars in globular clusters," *Monthly Notices of the Royal Astronomical Society* **76** (1916) 572–585.

[29] T. Lacroix, M. Stref, and J. Lavalle, "Anatomy of eddington-like inversion methods in the context of dark matter searches," *Journal of Cosmology and Astroparticle Physics* **2018** no. 09, (2018) 040.

[30] J. Herzog-Arbeitman, M. Lisanti, P. Madau, and L. Necib, "Empirical determination of dark matter velocities using metal-poor stars," *Physical review letters* **120** no. 4, (2018) 041102.

[31] L. Necib, M. Lisanti, and V. Belokurov, "Inferred evidence for dark matter kinematic substructure with sdss–gaia," *The Astrophysical Journal* **874** no. 1, (2019) 3.

[32] M. Kuhlen, N. Weiner, J. Diemand, P. Madau, B. Moore, D. Potter, J. Stadel, and M. Zemp, "Dark matter direct detection with non-maxwellian

velocity structure," *Journal of Cosmology and Astroparticle Physics* **2010** no. 02, (2010) 030.

[33] C. McCabe, "Astrophysical uncertainties of dark matter direct detection experiments," *Physical Review D* **82** no. 2, (2010) 023530.

[34] A. M. Green, "Astrophysical uncertainties on the local dark matter distribution and direct detection experiments," *Journal of Physics G: Nuclear and Particle Physics* **44** no. 8, (2017) 084001.

[35] A. Nuñez-Castiñeyra, E. Nezri, and V. Bertin, "Dark matter capture by the sun: revisiting velocity distribution uncertainties," *Journal of Cosmology and Astroparticle Physics* **2019** no. 12, (2019) 043.

[36] **SENSEI** Collaboration, J. Tiffenberg, M. Sofo-Haro, A. Drlica-Wagner, R. Essig, Y. Guardincerri, S. Holland, T. Volansky, and T.-T. Yu, "Single-electron and single-photon sensitivity with a silicon Skipper CCD," *Phys. Rev. Lett.* **119** no. 13, (2017) 131802, `arXiv:1706.00028 [physics.ins-det]`.

[37] **SENSEI** Collaboration, M. Crisler, R. Essig, J. Estrada, G. Fernandez, J. Tiffenberg, M. Sofo haro, T. Volansky, and T.-T. Yu, "SENSEI: First Direct-Detection Constraints on sub-GeV Dark Matter from a Surface Run," *Phys. Rev. Lett.* **121** no. 6, (2018) 061803, `arXiv:1804.00088 [hep-ex]`.

[38] **SENSEI** Collaboration, O. Abramoff *et al.*, "SENSEI: Direct-Detection Constraints on Sub-GeV Dark Matter from a Shallow Underground Run Using a Prototype Skipper-CCD," *Phys. Rev. Lett.* **122** no. 16, (2019) 161801, `arXiv:1901.10478 [hep-ex]`.

[39] **SENSEI** Collaboration, L. Barak *et al.*, "SENSEI: Direct-Detection Results on sub-GeV Dark Matter from a New Skipper-CCD," `arXiv:2004.11378 [astro-ph.CO]`.

[40] **SuperCDMS** Collaboration, R. Agnese *et al.*, "First Dark Matter Constraints from a SuperCDMS Single-Charge Sensitive Detector," *Phys. Rev. Lett.* **121** no. 5, (2018) 051301, `arXiv:1804.10697 [hep-ex]`. [Erratum: Phys.Rev.Lett. 122, 069901 (2019)].

[41] **DAMIC** Collaboration, A. Aguilar-Arevalo *et al.*, "Constraints on Light Dark Matter Particles Interacting with Electrons from DAMIC at SNOLAB," *Phys. Rev. Lett.* **123** no. 18, (2019) 181802, `arXiv:1907.12628 [astro-ph.CO]`.

[42] **EDELWEISS** Collaboration, Q. Arnaud *et al.*, "First germanium-based constraints on sub-MeV Dark Matter with the EDELWEISS experiment," `arXiv:2003.01046 [astro-ph.GA]`.

[43] **DAMIC, DAMIC-M** Collaboration, S. J. Lee, B. Kilminster, and A. Macchiolo, "Dark Matter in CCDs at Modane (DAMIC-M) : A silicon detector apparatus searching for low-energy physics processes," *JINST* **15** no. 02, (2020) C02050, `arXiv:2001.01209 [physics.ins-det]`.

[44] **DAMIC-M** Collaboration, N. Castelló-Mor, "DAMIC-M Experiment: Thick, Silicon CCDs to search for Light Dark Matter," *Nucl. Instrum. Meth. A* **958** (2020) 162933, `arXiv:2001.01476 [physics.ins-det]`.

[45] "Doe dark matter new initiatives."
https://science.osti.gov/-/media/hep/pdf/Awards/Dark-Matter-New-Initiatives-FY-2019--List-of-Awards.pdf.

[46] **Muon Collider** Collaboration, D. Stratakis *et al.*, "A Muon Collider Facility for Physics Discovery," arXiv:2203.08033 [physics.acc-ph].

[47] C. M. Ankenbrandt *et al.*, "Status of muon collider research and development and future plans," *Phys. Rev. ST Accel. Beams* **2** (1999) 081001, arXiv:physics/9901022.

[48] M.-H. Wang, Y. Nosochkov, Y. Cai, and M. Palmer, "Design of a 6 tev muon collider," *Journal of Instrumentation* **11** no. 09, (Sep, 2016) P09003. https://dx.doi.org/10.1088/1748-0221/11/09/P09003.

[49] M. Boscolo, J.-P. Delahaye, and M. Palmer, "The future prospects of muon colliders and neutrino factories," *Rev. Accel. Sci. Tech.* **10** no. 01, (2019) 189–214, arXiv:1808.01858 [physics.acc-ph].

[50] D. Neuffer and V. Shiltsev, "On the feasibility of a pulsed 14 TeV c.m.e. muon collider in the LHC tunnel," *JINST* **13** no. 10, (2018) T10003, arXiv:1811.10694 [physics.acc-ph].

[51] J. P. Delahaye, M. Diemoz, K. Long, B. Mansoulié, N. Pastrone, L. Rivkin, D. Schulte, A. Skrinsky, and A. Wulzer, "Muon Colliders," arXiv:1901.06150 [physics.acc-ph].

[52] V. Shiltsev and F. Zimmermann, "Modern and Future Colliders," *Rev. Mod. Phys.* **93** (2021) 015006, arXiv:2003.09084 [physics.acc-ph].

[53] **Muon Collider** Collaboration, J. de Blas *et al.*, "The physics case of a 3 TeV muon collider stage," arXiv:2203.07261 [hep-ph].

[54] **Muon Collider** Collaboration, S. Jindariani *et al.*, "Promising Technologies and R&D Directions for the Future Muon Collider Detectors," arXiv:2203.07224 [physics.ins-det].

[55] K. M. Black *et al.*, "Muon Collider Forum Report," arXiv:2209.01318 [hep-ex].

[56] C. Accettura *et al.*, "Towards a muon collider," *Eur. Phys. J. C* **83** no. 9, (2023) 864, arXiv:2303.08533 [physics.acc-ph].

[57] E. Eichten and A. Martin, "The Muon Collider as a H/A Factory," *Phys. Lett. B* **728** (2014) 125–130, arXiv:1306.2609 [hep-ph].

[58] N. Chakrabarty, T. Han, Z. Liu, and B. Mukhopadhyaya, "Radiative Return for Heavy Higgs Boson at a Muon Collider," *Phys. Rev. D* **91** no. 1, (2015) 015008, arXiv:1408.5912 [hep-ph].

[59] D. Buttazzo, D. Redigolo, F. Sala, and A. Tesi, "Fusing Vectors into Scalars at High Energy Lepton Colliders," *JHEP* **11** (2018) 144, arXiv:1807.04743 [hep-ph].

[60] M. Chiesa, F. Maltoni, L. Mantani, B. Mele, F. Piccinini, and X. Zhao, "Measuring the quartic Higgs self-coupling at a multi-TeV muon collider," *JHEP* **09** (2020) 098, arXiv:2003.13628 [hep-ph].

[61] T. Han, D. Liu, I. Low, and X. Wang, "Electroweak couplings of the Higgs boson at a multi-TeV muon collider," *Phys. Rev. D* **103** no. 1, (2021) 013002, arXiv:2008.12204 [hep-ph].

[62] P. Bandyopadhyay and A. Costantini, "Obscure Higgs boson at Colliders," *Phys. Rev. D* **103** no. 1, (2021) 015025, `arXiv:2010.02597 [hep-ph]`.

[63] D. Buttazzo, R. Franceschini, and A. Wulzer, "Two Paths Towards Precision at a Very High Energy Lepton Collider," *JHEP* **05** (2021) 219, `arXiv:2012.11555 [hep-ph]`.

[64] W. Liu and K.-P. Xie, "Probing electroweak phase transition with multi-TeV muon colliders and gravitational waves," *JHEP* **04** (2021) 015, `arXiv:2101.10469 [hep-ph]`.

[65] T. Han, S. Li, S. Su, W. Su, and Y. Wu, "Heavy Higgs bosons in 2HDM at a muon collider," *Phys. Rev. D* **104** no. 5, (2021) 055029, `arXiv:2102.08386 [hep-ph]`.

[66] R. Franceschini and M. Greco, "Higgs and BSM Physics at the Future Muon Collider," *Symmetry* **13** no. 5, (2021) 851, `arXiv:2104.05770 [hep-ph]`.

[67] M. Chiesa, B. Mele, and F. Piccinini, "Multi Higgs production via photon fusion at future multi-TeV muon colliders," `arXiv:2109.10109 [hep-ph]`.

[68] S. Chen, A. Glioti, R. Rattazzi, L. Ricci, and A. Wulzer, "Learning from radiation at a very high energy lepton collider," *JHEP* **05** (2022) 180, `arXiv:2202.10509 [hep-ph]`.

[69] S. Spor, "Probe of the anomalous neutral triple gauge couplings in photon-induced collision at future muon colliders," *Nucl. Phys. B* **991** (2023) 116198, `arXiv:2207.11585 [hep-ph]`.

[70] H. Amarkhail, S. C. Inan, and A. V. Kisselev, "Probing anomalous $\gamma\gamma\gamma\gamma$ couplings at a future muon collider," `arXiv:2306.03653 [hep-ph]`.

[71] R. Capdevilla, D. Curtin, Y. Kahn, and G. Krnjaic, "Discovering the physics of $(g-2)_\mu$ at future muon colliders," *Phys. Rev. D* **103** no. 7, (2021) 075028, arXiv:2006.16277 [hep-ph].

[72] D. Buttazzo and P. Paradisi, "Probing the muon $g-2$ anomaly with the Higgs boson at a muon collider," *Phys. Rev. D* **104** no. 7, (2021) 075021, arXiv:2012.02769 [hep-ph].

[73] W. Yin and M. Yamaguchi, "Muon g-2 at a multi-TeV muon collider," *Phys. Rev. D* **106** no. 3, (2022) 033007, arXiv:2012.03928 [hep-ph].

[74] G.-y. Huang, F. S. Queiroz, and W. Rodejohann, "Gauged $L_\mu - L_\tau$ at a muon collider," *Phys. Rev. D* **103** no. 9, (2021) 095005, arXiv:2101.04956 [hep-ph].

[75] R. Capdevilla, D. Curtin, Y. Kahn, and G. Krnjaic, "No-lose theorem for discovering the new physics of (g-2)μ at muon colliders," *Phys. Rev. D* **105** no. 1, (2022) 015028, arXiv:2101.10334 [hep-ph].

[76] N. Chen, B. Wang, and C.-Y. Yao, "The collider tests of a leptophilic scalar for the anomalous magnetic moments," arXiv:2102.05619 [hep-ph].

[77] G.-y. Huang, S. Jana, F. S. Queiroz, and W. Rodejohann, "Probing the RK(*) anomaly at a muon collider," *Phys. Rev. D* **105** no. 1, (2022) 015013, arXiv:2103.01617 [hep-ph].

[78] P. Asadi, R. Capdevilla, C. Cesarotti, and S. Homiller, "Searching for leptoquarks at future muon colliders," *JHEP* **10** (2021) 182, arXiv:2104.05720 [hep-ph].

[79] P. Bandyopadhyay, A. Karan, R. Mandal, and S. Parashar, "Distinguishing signatures of scalar leptoquarks at hadron and muon colliders," *Eur. Phys. J. C* **82** no. 10, (2022) 916, `arXiv:2108.06506 [hep-ph]`.

[80] S. Qian, C. Li, Q. Li, F. Meng, J. Xiao, T. Yang, M. Lu, and Z. You, "Searching for heavy leptoquarks at a muon collider," *JHEP* **12** (2021) 047, `arXiv:2109.01265 [hep-ph]`.

[81] S. Homiller, Q. Lu, and M. Reece, "Complementary signals of lepton flavor violation at a high-energy muon collider," *JHEP* **07** (2022) 036, `arXiv:2203.08825 [hep-ph]`.

[82] A. Azatov, F. Garosi, A. Greljo, D. Marzocca, J. Salko, and S. Trifinopoulos, "New physics in $b \to s\mu\mu$: FCC-hh or a muon collider?," *JHEP* **10** (2022) 149, `arXiv:2205.13552 [hep-ph]`.

[83] J.-L. Yang, C.-H. Chang, and T.-F. Feng, "The leptonic di-flavor and di-number violation processes at high energy $\mu^\pm\mu^\pm$ colliders," `arXiv:2302.13247 [hep-ph]`.

[84] W. Altmannshofer, S. A. Gadam, and S. Profumo, "Probing New Physics with $\mu^+\mu^- \to bs$ at a Muon Collider," `arXiv:2306.15017 [hep-ph]`.

[85] S. Jana and S. Klett, "Muonic Force and Neutrino Non-Standard Interactions at Muon Colliders," `arXiv:2308.07375 [hep-ph]`.

[86] N. Ghosh, S. K. Rai, and T. Samui, "Search For a Leptoquark and Vector-like Lepton in a Muon Collider," `arXiv:2309.07583 [hep-ph]`.

[87] T. Han, Z. Liu, L.-T. Wang, and X. Wang, "WIMPs at High Energy Muon Colliders," *Phys. Rev. D* **103** no. 7, (2021) 075004, arXiv:2009.11287 [hep-ph].

[88] S. Bottaro, A. Strumia, and N. Vignaroli, "Minimal Dark Matter bound states at future colliders," *JHEP* **06** (2021) 143, arXiv:2103.12766 [hep-ph].

[89] J. Liu, Z.-L. Han, Y. Jin, and H. Li, "Unraveling the Scotogenic model at muon collider," *JHEP* **12** (2022) 057, arXiv:2207.07382 [hep-ph].

[90] A. Jueid and S. Nasri, "Lepton portal dark matter at muon colliders: Total rates and generic features for phenomenologically viable scenarios," *Phys. Rev. D* **107** no. 11, (2023) 115027, arXiv:2301.12524 [hep-ph].

[91] N. Vignaroli, "Charged resonances and MDM bound states at a multi-TeV muon collider," *JHEP* **10** (2023) 121, arXiv:2304.12362 [hep-ph].

[92] M. Belfkir, A. Jueid, and S. Nasri, "Boosting dark matter searches at muon colliders with Machine Learning: the mono-Higgs channel as a case study," arXiv:2309.11241 [hep-ph].

[93] L. Di Luzio, R. Gröber, and G. Panico, "Probing new electroweak states via precision measurements at the LHC and future colliders," *JHEP* **01** (2019) 011, arXiv:1810.10993 [hep-ph].

[94] A. Costantini, F. De Lillo, F. Maltoni, L. Mantani, O. Mattelaer, R. Ruiz, and X. Zhao, "Vector boson fusion at multi-TeV muon colliders," *JHEP* **09** (2020) 080, arXiv:2005.10289 [hep-ph].

[95] W. Liu, K.-P. Xie, and Z. Yi, "Testing leptogenesis at the LHC and future muon colliders: A Z' scenario," *Phys. Rev. D* **105** no. 9, (2022) 095034, arXiv:2109.15087 [hep-ph].

[96] M. Casarsa, M. Fabbrichesi, and E. Gabrielli, "Monochromatic single photon events at the muon collider," *Phys. Rev. D* **105** no. 7, (2022) 075008, arXiv:2111.13220 [hep-ph].

[97] Y. Bao, J. Fan, and L. Li, "Electroweak ALP searches at a muon collider," *JHEP* **08** (2022) 276, arXiv:2203.04328 [hep-ph].

[98] S. C. İnan and A. V. Kisselev, "Probe of axion-like particles in vector boson scattering at a muon collider," *J. Phys. G* **50** no. 10, (2023) 105002, arXiv:2207.03325 [hep-ph].

[99] G.-S. Lv, X.-M. Cui, Y.-Q. Li, and Y.-B. Liu, "Pair production of the vectorlike top partner at future muon collider," *Nucl. Phys. B* **985** (2022) 116016.

[100] M. Chen and D. Liu, "Top Yukawa Coupling at the Muon Collider," arXiv:2212.11067 [hep-ph].

[101] T. H. Kwok, L. Li, T. Liu, and A. Rock, "Searching for Heavy Neutral Leptons at A Future Muon Collider," arXiv:2301.05177 [hep-ph].

[102] S. C. İnan and A. V. Kisselev, "Probe of a Randall-Sundrum-like model from muon pair production at high energy muon collider," arXiv:2301.08585 [hep-ph].

[103] T. A. Chowdhury, A. Jueid, S. Nasri, and S. Saad, "Probing Zee-Babu states at Muon Colliders," arXiv:2306.01255 [hep-ph].

[104] M. Belfkir, T. A. Chowdhury, and S. Nasri, "Doubly-charged scalars of the Minimal Left-Right Symmetric Model at Muon Colliders," arXiv:2307.16111 [hep-ph].

[105] S. Chigusa, S. Girmohanta, Y. Nakai, and Y. Zhang, "Aiming for Tops of ALPs with a Muon Collider," arXiv:2310.11018 [hep-ph].

[106] C. Cesarotti, S. Homiller, R. K. Mishra, and M. Reece, "Probing New Gauge Forces with a High-Energy Muon Beam Dump," *Phys. Rev. Lett.* **130** no. 7, (2023) 071803, arXiv:2202.12302 [hep-ph].

[107] C. Cesarotti and R. Gambhir, "The New Physics Case for Beam-Dump Experiments with Accelerated Muon Beams," arXiv:2310.16110 [hep-ph].

[108] P. Agrawal, S. Blanchet, Z. Chacko, and C. Kilic, "Flavored Dark Matter, and Its Implications for Direct Detection and Colliders," *Phys. Rev. D* **86** (2012) 055002, arXiv:1109.3516 [hep-ph].

[109] B. Batell, T. Lin, and L.-T. Wang, "Flavored Dark Matter and R-Parity Violation," *JHEP* **01** (2014) 075, arXiv:1309.4462 [hep-ph].

[110] P. Agrawal, B. Batell, D. Hooper, and T. Lin, "Flavored Dark Matter and the Galactic Center Gamma-Ray Excess," *Phys. Rev. D* **90** no. 6, (2014) 063512, arXiv:1404.1373 [hep-ph].

[111] P. Agrawal, M. Blanke, and K. Gemmler, "Flavored dark matter beyond Minimal Flavor Violation," *JHEP* **10** (2014) 072, arXiv:1405.6709 [hep-ph].

[112] P. Agrawal, Z. Chacko, C. Kilic, and C. B. Verhaaren, "A Couplet from Flavored Dark Matter," *JHEP* **08** (2015) 072, arXiv:1503.03057 [hep-ph].

[113] P. Agrawal, Z. Chacko, E. C. F. S. Fortes, and C. Kilic, "Skew-Flavored Dark Matter," *Phys. Rev. D* **93** no. 10, (2016) 103510, arXiv:1511.06293 [hep-ph].

[114] P. Agrawal, C. Kilic, S. Swaminathan, and C. Trendafilova, "Secretly Asymmetric Dark Matter," *Phys. Rev. D* **95** no. 1, (2017) 015031, arXiv:1608.04745 [hep-ph].

[115] N. Desai, C. Kilic, Y.-P. Yang, and T. Youn, "Suppressed flavor violation in Lepton Flavored Dark Matter from an extra dimension," *Phys. Rev. D* **101** (2020) 075043, arXiv:2001.00720 [hep-ph].

[116] H. Acaroğlu, P. Agrawal, and M. Blanke, "Lepton-flavoured scalar dark matter in Dark Minimal Flavour Violation," *JHEP* **05** (2023) 106, arXiv:2211.03809 [hep-ph].

[117] L. J. Hall, K. Jedamzik, J. March-Russell, and S. M. West, "Freeze-In Production of FIMP Dark Matter," *JHEP* **03** (2010) 080, arXiv:0911.1120 [hep-ph].

[118] A. Radick, A.-M. Taki, and T.-T. Yu, "Dependence of Dark Matter - Electron Scattering on the Galactic Dark Matter Velocity Distribution," *JCAP* **02** (2021) 004, arXiv:2011.02493 [hep-ph].

[119] P. Asadi, A. Radick, and T.-T. Yu, "Interplay of freeze-in and freeze-out: Lepton-flavored dark matter and muon colliders," *Phys. Rev. D* **110** no. 3, (2024) 035022, arXiv:2312.03826 [hep-ph].

[120] R. Essig, M. Fernandez-Serra, J. Mardon, A. Soto, T. Volansky, and T.-T. Yu, "Direct Detection of sub-GeV Dark Matter with Semiconductor Targets," *JHEP* **05** (2016) 046, arXiv:1509.01598 [hep-ph].

[121] V. S. Vavilov, "RADIATION IONIZATION PROCESSES IN GERMANIUM AND SILICON CRYSTALS," *Soviet Physics Uspekhi* **4** no. 5, (May, 1962) 761–769. https://doi.org/10.1070%2Fpu1962v004n05abeh003376.

[122] D. Rodrigues *et al.*, "Absolute measurement of the Fano factor using a Skipper-CCD," arXiv:2004.11499 [physics.ins-det].

[123] M. Lisanti, "Lectures on dark matter physics," in *New Frontiers in Fields and Strings: TASI 2015 Proceedings of the 2015 Theoretical Advanced Study Institute in Elementary Particle Physics*, pp. 399–446. World Scientific, 2017.

[124] J. Binney and S. Tremaine, "Galactic dynamics 2nd ed. ed j," 2008.

[125] C. Hunter and E. Qian, "Two-integral distribution functions for axisymmetric galaxies," *Monthly Notices of the Royal Astronomical Society* **262** no. 2, (1993) 401–428.

[126] M. Petač and P. Ullio, "Two-integral distribution functions in axisymmetric galaxies: implications for dark matter searches," *Physical Review D* **99** no. 4, (2019) 043003.

[127] M. Petac, "Equilibrium axisymmetric halo model for the milky way and its implications for direct and indirect dm searches," *arXiv preprint arXiv:2008.11172* (2020) .

[128] P. Ullio and M. Kamionkowski, "Velocity distributions and annual-modulation signatures of weakly-interacting massive particles," *Journal of High Energy Physics* **2001** no. 03, (2001) 049.

[129] N. Bozorgnia, R. Catena, and T. Schwetz, "Anisotropic dark matter distribution functions and impact on wimp direct detection," *Journal of Cosmology and Astroparticle Physics* **2013** no. 12, (2013) 050.

[130] M. Fornasa and A. M. Green, "Self-consistent phase-space distribution function for the anisotropic dark matter halo of the milky way," *Physical Review D* **89** no. 6, (2014) 063531.

[131] N. W. Evans, C. A. O'Hare, and C. McCabe, "Refinement of the standard halo model for dark matter searches in light of the gaia sausage," *Physical Review D* **99** no. 2, (2019) 023012.

[132] M. Vogelsberger, A. Helmi, V. Springel, S. D. White, J. Wang, C. S. Frenk, A. Jenkins, A. Ludlow, and J. F. Navarro, "Phase-space structure in the local dark matter distribution and its signature in direct detection experiments," *Monthly Notices of the Royal Astronomical Society* **395** no. 2, (2009) 797–811.

[133] F.-S. Ling, E. Nezri, E. Athanassoula, and R. Teyssier, "Dark matter direct detection signals inferred from a cosmological n-body simulation with baryons," *Journal of Cosmology and Astroparticle Physics* **2010** no. 02, (2010) 012.

[134] M. Sparre and S. H. Hansen, "The behaviour of shape and velocity anisotropy in dark matter haloes," *Journal of Cosmology and Astroparticle Physics* **2012** no. 10, (2012) 049.

[135] N. Bozorgnia and G. Bertone, "Implications of hydrodynamical simulations for the interpretation of direct dark matter searches," *International Journal of Modern Physics A* **32** no. 21, (2017) 1730016.

[136] J. D. Lewin and P. F. Smith, "Review of mathematics, numerical factors, and corrections for dark matter experiments based on elastic nuclear recoil," *Astropart. Phys.* **6** (1996) 87–112.

[137] M. Fairbairn and T. Schwetz, "Spin-independent elastic wimp scattering and the dama annual modulation signal," *Journal of Cosmology and Astroparticle Physics* **2009** no. 01, (2009) 037.

[138] J. March-Russell, C. McCabe, and M. McCullough, "Inelastic dark matter, non-standard halos and the dama/libra results," *Journal of High Energy Physics* **2009** no. 05, (2009) 071.

[139] Y.-Y. Mao, L. E. Strigari, R. H. Wechsler, H.-Y. Wu, and O. Hahn, "Halo-to-halo similarity and scatter in the velocity distribution of dark matter," *The Astrophysical Journal* **764** no. 1, (2013) 35.

[140] A. Pillepich, M. Kuhlen, J. Guedes, and P. Madau, "The distribution of dark matter in the milky way's disk," *The Astrophysical Journal* **784** no. 2, (2014) 161.

[141] N. Bozorgnia, F. Calore, M. Schaller, M. Lovell, G. Bertone, C. S. Frenk, R. A. Crain, J. F. Navarro, J. Schaye, and T. Theuns, "Simulated milky way analogues: implications for dark matter direct searches," *Journal of Cosmology and Astroparticle Physics* **2016** no. 05, (2016) 024.

[142] I. Butsky, A. V. Maccio, A. A. Dutton, L. Wang, A. Obreja, G. S. Stinson, C. Penzo, X. Kang, B. W. Keller, and J. Wadsley, "Nihao project ii: Halo shape, phase-space density and velocity distribution of dark matter in galaxy formation simulations," *Monthly Notices of the Royal Astronomical Society* **462** no. 1, (2016) 663–680.

[143] C. Kelso, C. Savage, M. Valluri, K. Freese, G. S. Stinson, and J. Bailin, "The impact of baryons on the direct detection of dark matter," *Journal of Cosmology and Astroparticle Physics* **2016** no. 08, (2016) 071.

[144] J. D. Sloane, M. R. Buckley, A. M. Brooks, and F. Governato, "Assessing astrophysical uncertainties in direct detection with galaxy simulations," *The Astrophysical Journal* **831** no. 1, (2016) 93.

[145] C. Tsallis, "Possible generalization of boltzmann-gibbs statistics," *Journal of Statistical Physics* **52** (07, 1988) 479–487.

[146] S. H. Hansen, B. Moore, M. Zemp, and J. Stadel, "A universal velocity distribution of relaxed collisionless structures," *Journal of Cosmology and Astroparticle Physics* **2006** no. 01, (Jan, 2006) 014–014.

[147] J. Vergados, S. Hansen, and O. Host, "The impact of going beyond the Maxwell distribution in direct dark matter detection rates," *Phys. Rev. D* **77** (2008) 023509, `arXiv:0711.4895 [astro-ph]`.

[148] F. S. Ling, E. Nezri, E. Athanassoula, and R. Teyssier, "Dark Matter Direct Detection Signals inferred from a Cosmological N-body Simulation with Baryons," *JCAP* **1002** (2010) 012, `arXiv:0909.2028 [astro-ph.GA]`.

[149] S. H. Hansen, D. Egli, L. Hollenstein, and C. Salzmann, “Dark matter distribution function from non-extensive statistical mechanics,” *New Astronomy* **10** no. 5, (2005) 379–384.

[150] J. Lima, R. Silva, and A. Plastino, “Nonextensive thermostatistics and the h theorem,” *Physical review letters* **86** no. 14, (2001) 2938.

[151] S. H. Hansen, B. Moore, M. Zemp, and J. Stadel, “A universal velocity distribution of relaxed collisionless structures,” *Journal of Cosmology and Astroparticle Physics* **2006** no. 01, (2006) 014.

[152] R. Teyssier, “Cosmological hydrodynamics with adaptive mesh refinement-a new high resolution code called ramses,” *Astronomy & Astrophysics* **385** no. 1, (2002) 337–364.

[153] M. Vogelsberger, F. Marinacci, P. Torrey, and E. Puchwein, “Cosmological simulations of galaxy formation,” *Nature Reviews Physics* **2** no. 1, (2020) 42–66.

[154] M. Lisanti, L. E. Strigari, J. G. Wacker, and R. H. Wechsler, “The Dark Matter at the End of the Galaxy,” *Phys. Rev. D* **83** (2011) 023519, `arXiv:1010.4300 [astro-ph.CO]`.

[155] J. D. Sloane, M. R. Buckley, A. M. Brooks, and F. Governato, “Assessing Astrophysical Uncertainties in Direct Detection with Galaxy Simulations,” *Astrophys. J.* **831** (2016) 93, `arXiv:1601.05402 [astro-ph.GA]`.

[156] A. Hryczuk, E. Karukes, L. Roszkowski, and M. Talia, “Impact of uncertainties in the halo velocity profile on direct detection of sub-GeV dark matter,” `arXiv:2001.09156 [hep-ph]`.

[157] Y.-Y. Mao, L. E. Strigari, R. H. Wechsler, H.-Y. Wu, and O. Hahn, "Halo-to-Halo Similarity and Scatter in the Velocity Distribution of Dark Matter," *Astrophys. J.* **764** (2013) 35, `arXiv:1210.2721 [astro-ph.CO]`.

[158] Y.-Y. Mao, L. E. Strigari, and R. H. Wechsler, "Connecting Direct Dark Matter Detection Experiments to Cosmologically Motivated Halo Models," *Phys. Rev.* **D89** no. 6, (2014) 063513, `arXiv:1304.6401 [astro-ph.CO]`.

[159] H.-Y. Wu, O. Hahn, R. H. Wechsler, Y.-Y. Mao, and P. S. Behroozi, "Rhapsody. i. structural properties and formation history from a statistical sample of re-simulated cluster-size halos," *The Astrophysical Journal* **763** no. 2, (2013) 70.

[160] A. A. Klypin, S. Trujillo-Gomez, and J. Primack, "Dark matter halos in the standard cosmological model: Results from the bolshoi simulation," *The Astrophysical Journal* **740** no. 2, (2011) 102.

[161] J. Guedes, S. Callegari, P. Madau, and L. Mayer, "Forming realistic late-type spirals in a λcdm universe: the eris simulation," *The Astrophysical Journal* **742** no. 2, (2011) 76.

[162] D. Carollo, T. C. Beers, M. Chiba, J. E. Norris, K. C. Freeman, Y. S. Lee, Ž. Ivezić, C. M. Rockosi, and B. Yanny, "Structure and kinematics of the stellar halos and thick disks of the milky way based on calibration stars from sloan digital sky survey dr7," *The Astrophysical Journal* **712** no. 1, (2010) 692.

[163] J. Herzog-Arbeitman, M. Lisanti, and L. Necib, "The metal-poor stellar halo in rave-tgas and its implications for the velocity distribution of dark matter," *Journal of Cosmology and Astroparticle Physics* **2018** no. 04, (2018) 052.

[164] A. Kunder, G. Kordopatis, M. Steinmetz, T. Zwitter, P. J. McMillan, L. Casagrande, H. Enke, J. Wojno, M. Valentini, C. Chiappini, *et al.*, "The radial velocity experiment (rave): fifth data release," *The Astronomical Journal* **153** no. 2, (2017) 75.

[165] D. Michalik, L. Lindegren, and D. Hobbs, "The tycho-gaia astrometric solution-how to get 2.5 million parallaxes with less than one year of gaia data," *Astronomy & Astrophysics* **574** (2015) A115.

[166] C. P. Ahn, R. Alexandroff, C. A. Prieto, S. F. Anderson, T. Anderton, B. H. Andrews, É. Aubourg, S. Bailey, E. Balbinot, R. Barnes, *et al.*, "The ninth data release of the sloan digital sky survey: first spectroscopic data from the sdss-iii baryon oscillation spectroscopic survey," *The Astrophysical Journal Supplement Series* **203** no. 2, (2012) 21.

[167] A. Brown, A. Vallenari, T. Prusti, J. De Bruijne, C. Babusiaux, C. Bailer-Jones, M. Biermann, D. W. Evans, L. Eyer, F. Jansen, *et al.*, "Gaia data release 2-summary of the contents and survey properties," *Astronomy & astrophysics* **616** (2018) A1.

[168] M. Lisanti and D. N. Spergel, "Dark matter debris flows in the milky way," *Physics of the Dark Universe* **1** no. 1-2, (2012) 155–161.

[169] M. Kuhlen, M. Lisanti, and D. N. Spergel, "Direct detection of dark matter debris flows," *Physical Review D* **86** no. 6, (2012) 063505.

[170] J. Diemand, M. Kuhlen, P. Madau, M. Zemp, B. Moore, D. Potter, and J. Stadel, "Clumps and streams in the local dark matter distribution," *Nature* **454** no. 7205, (2008) 735–738.

[171] M. Kuhlen, J. Diemand, P. Madau, and M. Zemp, "The via lactea incite simulation: galactic dark matter substructure at high resolution," in *J. Phys. Conf. Ser*, vol. 125, pp. 0810–3614. 2008.

[172] N. W. Evans, C. A. O'Hare, and C. McCabe, "Shm++: A refinement of the standard halo model for dark matter searches," *arXiv preprint arXiv:1810.11468* .

[173] "Dark Matter Velocity Distribution." `https://linoush.github.io/DM_Velocity_Distribution/`. Accessed: 2020-11-11.

[174] J. Buch, M. A. Buen-Abad, J. Fan, and J. S. C. Leung, "Dark matter substructure under the electron scattering lamppost," *arXiv preprint arXiv:2007.13750* (2020) .

[175] J. C. Kapteyn, "First attempt at a theory of the arrangement and motion of the sidereal system," *The Astrophysical Journal* **55** (1922) 302.

[176] J. Oort, "Note on the determination of kz and on the mass density near the sun.," *Bulletin of the Astronomical Institutes of the Netherlands* **15** (1960) 45.

[177] J. N. Bahcall, "Self-consistent determinations of the total amount of matter near the sun," *The Astrophysical Journal* **276** (1984) 169–181.

[178] K. Kuijken and G. Gilmore, "The galactic disk surface mass density and the galactic force k (z) at z= 1.1 kiloparsecs," *The Astrophysical Journal* **367** (1991) L9–L13.

[179] S. Garbari, C. Liu, J. I. Read, and G. Lake, "A new determination of the local dark matter density from the kinematics of k dwarfs," *Monthly Notices of the Royal Astronomical Society* **425** no. 2, (2012) 1445–1458.

[180] J. Bovy and S. Tremaine, "On the local dark matter density," *The Astrophysical Journal* **756** no. 1, (2012) 89.

[181] L. Zhang, H.-W. Rix, G. van de Ven, J. Bovy, C. Liu, and G. Zhao, "The gravitational potential near the sun from segue k-dwarf kinematics," *The Astrophysical Journal* **772** no. 2, (2013) 108.

[182] W. Dehnen and J. Binney, "Mass models of the milky way," *Monthly Notices of the Royal Astronomical Society* **294** no. 3, (1998) 429–438.

[183] M. Weber and W. de Boer, "Determination of the local dark matter density in our galaxy," *Astronomy & Astrophysics* **509** (2010) A25.

[184] R. Catena and P. Ullio, "A novel determination of the local dark matter density," *Journal of Cosmology and Astroparticle Physics* **2010** no. 08, (2010) 004.

[185] P. J. McMillan, "Mass models of the milky way," *Monthly Notices of the Royal Astronomical Society* **414** no. 3, (2011) 2446–2457.

[186] J. Read, "The local dark matter density," *Journal of Physics G: Nuclear and Particle Physics* **41** no. 6, (2014) 063101.

[187] J. Buch, S. C. J. Leung, and J. Fan, "Using gaia dr2 to constrain local dark matter density and thin dark disk," *Journal of Cosmology and Astroparticle Physics* **2019** no. 04, (2019) 026.

[188] M. Zemp, J. Diemand, M. Kuhlen, P. Madau, B. Moore, D. Potter, J. Stadel, and L. Widrow, "The graininess of dark matter haloes," *Monthly Notices of the Royal Astronomical Society* **394** no. 2, (2009) 641–659.

[189] M. Pato, O. Agertz, G. Bertone, B. Moore, and R. Teyssier, "Systematic uncertainties in the determination of the local dark matter density," *Physical Review D* **82** no. 2, (2010) 023531.

[190] N. Bernal, J. E. Forero-Romero, R. Garani, and S. Palomares-Ruiz, "Systematic uncertainties from halo asphericity in dark matter searches," *Journal of Cosmology and Astroparticle Physics* **2014** no. 09, (2014) 004.

[191] A. Widmark, "Measuring the local matter density using gaia dr2," *Astronomy & Astrophysics* **623** (2019) A30.

[192] **Particle Data Group** Collaboration, P. Zyla *et al.*, "Review of Particle Physics," *PTEP* **2020** no. 8, (2020) 083C01.

[193] S. Sivertsson, H. Silverwood, J. I. Read, G. Bertone, and P. Steger, "The localdark matter density from sdss-segue g-dwarfs," *Monthly Notices of the Royal Astronomical Society* **478** no. 2, (2018) 1677–1693.

[194] **Particle Data Group** Collaboration, M. Tanabashi *et al.*, "Review of Particle Physics," *Phys. Rev. D* **98** no. 3, (2018) 030001.

[195] S. E. Koposov, H.-W. Rix, and D. W. Hogg, "Constraining the milky way potential with a six-dimensional phase-space map of the gd-1 stellar stream," *The Astrophysical Journal* **712** no. 1, (2010) 260.

[196] M. Feast and P. Whitelock, "Galactic kinematics of cepheids from hipparcos proper motions," *Monthly Notices of the Royal Astronomical Society* **291** no. 4, (1997) 683–693.

[197] F. J. Kerr and D. Lynden-Bell, "Review of galactic constants," *Monthly Notices of the Royal Astronomical Society* **221** no. 4, (1986) 1023–1038.

[198] J. Bovy, C. A. Prieto, T. C. Beers, D. Bizyaev, L. N. Da Costa, K. Cunha, G. L. Ebelke, D. J. Eisenstein, P. M. Frinchaboy, A. E. G. Pérez, *et al.*, "The milky way's circular-velocity curve between 4 and 14 kpc from apogee data," *The Astrophysical Journal* **759** no. 2, (2012) 131.

[199] J. Bland-Hawthorn and O. Gerhard, "The galaxy in context: structural, kinematic, and integrated properties," *Annual Review of Astronomy and Astrophysics* **54** (2016) 529–596.

[200] M. J. Reid and A. Brunthaler, "The proper motion of sagittarius a*. ii. the mass of sagittarius a," *The Astrophysical Journal* **616** no. 2, (2004) 872.

[201] G. Strömberg, "The motions of the stars within 20 parsecs of the sun.," *The Astrophysical Journal* **104** (1946) 12.

[202] R. Schönrich, J. Binney, and W. Dehnen, "Local kinematics and the local standard of rest," *Monthly Notices of the Royal Astronomical Society* **403** no. 4, (2010) 1829–1833.

[203] M. J. Reid, "The distance to the center of the galaxy," *Annual review of astronomy and astrophysics* **31** (1993) 345–372.

[204] A. M. Green, "Effect of realistic astrophysical inputs on the phase and shape of the weakly interacting massive particles annual modulation signal," *Physical Review D* **68** no. 2, (2003) 023004.

[205] S. Gillessen, F. Eisenhauer, T. Fritz, H. Bartko, K. Dodds-Eden, O. Pfuhl, T. Ott, and R. Genzel, "The orbit of the star s2 around sgr a* from very large telescope and keck data," *The Astrophysical Journal Letters* **707** no. 2, (2009) L114.

[206] M. Reid, K. Menten, A. Brunthaler, X. Zheng, T. Dame, Y. Xu, Y. Wu, B. Zhang, A. Sanna, M. Sato, *et al.*, "Trigonometric parallaxes of high mass star forming regions: the structure and kinematics of the milky way," *The Astrophysical Journal* **783** no. 2, (2014) 130.

[207] A.-C. Eilers, D. W. Hogg, H.-W. Rix, and M. K. Ness, "The circular velocity curve of the milky way from 5 to 25 kpc," *The Astrophysical Journal* **871** no. 1, (2019) 120.

[208] S. R. Majewski, R. P. Schiavon, P. M. Frinchaboy, C. A. Prieto, R. Barkhouser, D. Bizyaev, B. Blank, S. Brunner, A. Burton, R. Carrera, *et al.*, "The apache point observatory galactic evolution experiment (apogee)," *The Astronomical Journal* **154** no. 3, (2017) 94.

[209] M. Skrutskie, R. Cutri, R. Stiening, M. Weinberg, S. Schneider, J. Carpenter, C. Beichman, R. Capps, T. Chester, J. Elias, *et al.*, "The two micron all sky survey (2mass)," *The Astronomical Journal* **131** no. 2, (2006) 1163.

[210] E. L. Wright, P. R. Eisenhardt, A. K. Mainzer, M. E. Ressler, R. M. Cutri, T. Jarrett, J. D. Kirkpatrick, D. Padgett, R. S. McMillan, M. Skrutskie, *et al.*, "The wide-field infrared survey explorer (wise): mission description and initial on-orbit performance," *The Astronomical Journal* **140** no. 6, (2010) 1868.

[211] D. W. Hogg, A.-C. Eilers, and H.-W. Rix, "Spectrophotometric parallaxes with linear models: Accurate distances for luminous red-giant stars," *The Astronomical Journal* **158** no. 4, (2019) 147.

[212] R. Abuter, A. Amorim, M. Bauböck, J. Berger, H. Bonnet, W. Brandner, V. Cardoso, Y. Clénet, P. de Zeeuw, J. Dexter, *et al.*, "Detection of the schwarzschild precession in the orbit of the star s2 near the galactic centre massive black hole," *Astronomy & Astrophysics* **636** (2020) L5.

[213] M. Reid, K. Menten, X. Zheng, A. Brunthaler, L. Moscadelli, Y. Xu, B. Zhang, M. Sato, M. Honma, T. Hirota, *et al.*, "Trigonometric parallaxes of massive star-forming regions. vi. galactic structure, fundamental parameters, and noncircular motions," *The Astrophysical Journal* **700** no. 1, (2009) 137.

[214] P. J. McMillan and J. J. Binney, "The uncertainty in galactic parameters," *Monthly Notices of the Royal Astronomical Society* **402** no. 2, (2010) 934–940.

[215] P. J. Leonard and S. Tremaine, "The local galactic escape speed," *The Astrophysical Journal* **353** (1990) 486–493.

[216] M. C. Smith, G. R. Ruchti, A. Helmi, R. F. Wyse, J. P. Fulbright, K. C. Freeman, J. F. Navarro, G. M. Seabroke, M. Steinmetz, M. Williams, *et al.*,

"The rave survey: constraining the local galactic escape speed," *Monthly Notices of the Royal Astronomical Society* **379** no. 2, (2007) 755–772.

[217] T. Piffl, C. Scannapieco, J. Binney, M. Steinmetz, R.-D. Scholz, M. E. Williams, R. S. De Jong, G. Kordopatis, G. Matijevič, O. Bienayme, *et al.*, "The rave survey: the galactic escape speed and the mass of the milky way," *Astronomy & Astrophysics* **562** (2014) A91.

[218] J. Lavalle and S. Magni, "Making sense of the local galactic escape speed estimates in direct dark matter searches," *Physical Review D* **91** no. 2, (2015) 023510.

[219] A. J. Deason, A. Fattahi, V. Belokurov, N. W. Evans, R. J. Grand, F. Marinacci, and R. Pakmor, "The local high-velocity tail and the galactic escape speed," *Monthly Notices of the Royal Astronomical Society* **485** no. 3, (2019) 3514–3526.

[220] G. Monari, B. Famaey, I. Carrillo, T. Piffl, M. Steinmetz, R. F. Wyse, F. Anders, C. Chiappini, and K. Janssen, "The escape speed curve of the galaxy obtained from gaia dr2 implies a heavy milky way," *Astronomy & Astrophysics* **616** (2018) L9.

[221] G. Gelmini and P. Gondolo, "Weakly interacting massive particle annual modulation with opposite phase in late-infall halo models," *Physical Review D* **64** no. 2, (2001) 023504.

[222] S. K. Lee, M. Lisanti, and B. R. Safdi, "Dark-Matter Harmonics Beyond Annual Modulation," *JCAP* **11** (2013) 033, `arXiv:1307.5323 [hep-ph]`.

[223] C. McCabe, "The earth's velocity for direct detection experiments," *Journal of Cosmology and Astroparticle Physics* **2014** no. 02, (2014) 027.

[224] F. C. Porter, "Testing Consistency of Two Histograms," `arXiv:0804.0380 [physics.data-an]`.

[225] M. Benito, F. Iocco, and A. Cuoco, "Uncertainties in the Galactic dark matter distribution: an update," `arXiv:2009.13523 [astro-ph.GA]`.

[226] M. Pato, L. E. Strigari, R. Trotta, and G. Bertone, "Taming astrophysical bias in direct dark matter searches," *JCAP* **02** (2013) 041, `arXiv:1211.7063 [astro-ph.CO]`.

[227] P. J. Fox, G. D. Kribs, and T. M. Tait, "Interpreting dark matter direct detection independently of the local velocity and density distribution," *Physical Review D* **83** no. 3, (2011) 034007.

[228] P. J. Fox, J. Liu, and N. Weiner, "Integrating Out Astrophysical Uncertainties," *Phys. Rev. D* **83** (2011) 103514, `arXiv:1011.1915 [hep-ph]`.

[229] P. Gondolo and G. B. Gelmini, "Halo independent comparison of direct dark matter detection data," *Journal of Cosmology and Astroparticle Physics* **2012** no. 12, (2012) 015.

[230] E. Del Nobile, G. B. Gelmini, P. Gondolo, and J.-H. Huh, "Halo-independent analysis of direct detection data for light WIMPs," *JCAP* **10** (2013) 026, `arXiv:1304.6183 [hep-ph]`.

[231] N. Bozorgnia, J. Herrero-Garcia, T. Schwetz, and J. Zupan, "Halo-independent methods for inelastic dark matter scattering," *JCAP* **07** (2013) 049, `arXiv:1305.3575 [hep-ph]`.

[232] P. J. Fox, Y. Kahn, and M. McCullough, “Taking halo-independent dark matter methods out of the bin,” *Journal of Cosmology and Astroparticle Physics* **2014** no. 10, (2014) 076.

[233] E. Andersson, A. Bökmark, R. Catena, T. Emken, H. K. Moberg, and E. Åstrand, “Projected sensitivity to sub-gev dark matter of next-generation semiconductor detectors,” *Journal of Cosmology and Astroparticle Physics* **2020** no. 05, (2020) 036.

[234] J. Buch, M. A. Buen-Abad, J. Fan, and J. S. C. Leung, “Dark Matter Substructure under the Electron Scattering Lamppost,” *Phys. Rev. D* **102** no. 8, (2020) 083010, `arXiv:2007.13750 [hep-ph]`.

[235] S. Chang, R. Edezhath, J. Hutchinson, and M. Luty, “Effective WIMPs,” *Phys. Rev. D* **89** no. 1, (2014) 015011, `arXiv:1307.8120 [hep-ph]`.

[236] S. Chang, R. Edezhath, J. Hutchinson, and M. Luty, “Leptophilic Effective WIMPs,” *Phys. Rev. D* **90** no. 1, (2014) 015011, `arXiv:1402.7358 [hep-ph]`.

[237] Y. Bai and J. Berger, “Fermion Portal Dark Matter,” *JHEP* **11** (2013) 171, `arXiv:1308.0612 [hep-ph]`.

[238] Y. Bai and J. Berger, “Lepton Portal Dark Matter,” *JHEP* **08** (2014) 153, `arXiv:1402.6696 [hep-ph]`.

[239] A. DiFranzo, K. I. Nagao, A. Rajaraman, and T. M. P. Tait, “Simplified Models for Dark Matter Interacting with Quarks,” *JHEP* **11** (2013) 014, `arXiv:1308.2679 [hep-ph]`. [Erratum: JHEP 01, 162 (2014)].

[240] M. Garny, A. Ibarra, S. Rydbeck, and S. Vogl, "Majorana Dark Matter with a Coloured Mediator: Collider vs Direct and Indirect Searches," *JHEP* **06** (2014) 169, arXiv:1403.4634 [hep-ph].

[241] F. Elahi, C. Kolda, and J. Unwin, "UltraViolet Freeze-in," *JHEP* **03** (2015) 048, arXiv:1410.6157 [hep-ph].

[242] G. D'Ambrosio, S. Chatterjee, R. Laha, and S. K. Vempati, "Freezing In with Lepton Flavored Fermions," *SciPost Phys.* **11** (2021) 006, arXiv:2103.03886 [hep-ph].

[243] J. A. Evans and J. Shelton, "Long-Lived Staus and Displaced Leptons at the LHC," *JHEP* **04** (2016) 056, arXiv:1601.01326 [hep-ph].

[244] L. Calibbi, F. D'Eramo, S. Junius, L. Lopez-Honorez, and A. Mariotti, "Displaced new physics at colliders and the early universe before its first second," *JHEP* **05** (2021) 234, arXiv:2102.06221 [hep-ph].

[245] M. Garny and J. Heisig, "Interplay of super-WIMP and freeze-in production of dark matter," *Phys. Rev. D* **98** no. 9, (2018) 095031, arXiv:1809.10135 [hep-ph].

[246] Q. Decant, J. Heisig, D. C. Hooper, and L. Lopez-Honorez, "Lyman-α constraints on freeze-in and superWIMPs," *JCAP* **03** (2022) 041, arXiv:2111.09321 [astro-ph.CO].

[247] E. W. Kolb and M. S. Turner, *The Early Universe*, vol. 69. 1990.

[248] **Planck** Collaboration, N. Aghanim *et al.*, "Planck 2018 results. VI. Cosmological parameters," *Astron. Astrophys.* **641** (2020) A6,

arXiv:1807.06209 [astro-ph.CO]. [Erratum: Astron.Astrophys. 652, C4 (2021)].

[249] **ATLAS** Collaboration, G. Aad *et al.*, "Search for direct pair production of sleptons and charginos decaying to two leptons and neutralinos with mass splittings near the W-boson mass in $\sqrt{s} = 13$ TeV pp collisions with the ATLAS detector," *JHEP* **06** (2023) 031, arXiv:2209.13935 [hep-ex].

[250] **ATLAS** Collaboration, G. Aad *et al.*, "Search for electroweak production of charginos and sleptons decaying into final states with two leptons and missing transverse momentum in $\sqrt{s} = 13$ TeV pp collisions using the ATLAS detector," *Eur. Phys. J. C* **80** no. 2, (2020) 123, arXiv:1908.08215 [hep-ex].

[251] **DELPHI** Collaboration, J. Abdallah *et al.*, "Searches for supersymmetric particles in e+ e- collisions up to 208-GeV and interpretation of the results within the MSSM," *Eur. Phys. J. C* **31** (2003) 421–479, arXiv:hep-ex/0311019.

[252] **ALEPH** Collaboration, A. Heister *et al.*, "Search for charginos nearly mass degenerate with the lightest neutralino in e+ e- collisions at center-of-mass energies up to 209-GeV," *Phys. Lett. B* **533** (2002) 223–236, arXiv:hep-ex/0203020.

[253] F. D'Eramo and A. Lenoci, "Lower mass bounds on FIMP dark matter produced via freeze-in," *JCAP* **10** (2021) 045, arXiv:2012.01446 [hep-ph].

[254] **MICE** Collaboration, M. Bogomilov *et al.*, "Demonstration of cooling by the Muon Ionization Cooling Experiment," *Nature* **578** no. 7793, (2020) 53–59, arXiv:1907.08562 [physics.acc-ph].

[255] **CLICdp** Collaboration, N. Alipour Tehrani *et al.*, "CLICdet: The post-CDR CLIC detector model,".

[256] **ILC** Collaboration, G. Aarons *et al.*, "ILC Reference Design Report Volume 4 - Detectors," arXiv:0712.2356 [physics.ins-det].

[257] S. Knapen and S. Lowette, "A guide to hunting long-lived particles at the LHC," arXiv:2212.03883 [hep-ph].

[258] T. Han, Y. Ma, and K. Xie, "High energy leptonic collisions and electroweak parton distribution functions," *Phys. Rev. D* **103** no. 3, (2021) L031301, arXiv:2007.14300 [hep-ph].

[259] T. Han, Y. Ma, and K. Xie, "Quark and gluon contents of a lepton at high energies," *JHEP* **02** (2022) 154, arXiv:2103.09844 [hep-ph].

[260] R. Ruiz, A. Costantini, F. Maltoni, and O. Mattelaer, "The Effective Vector Boson Approximation in high-energy muon collisions," *JHEP* **06** (2022) 114, arXiv:2111.02442 [hep-ph].

[261] C. G. Lester and D. J. Summers, "Measuring masses of semiinvisibly decaying particles pair produced at hadron colliders," *Phys. Lett. B* **463** (1999) 99–103, arXiv:hep-ph/9906349.

[262] K. J. Kim and Y.-S. Tsai, "Improved weizsäcker-williams method and its application to lepton and w-boson pair production," *Phys. Rev. D* **8** (Nov, 1973) 3109–3125. https://link.aps.org/doi/10.1103/PhysRevD.8.3109.

[263] S. Frixione, M. L. Mangano, P. Nason, and G. Ridolfi, "Improving the Weizsacker-Williams approximation in electron - proton collisions," *Phys. Lett. B* **319** (1993) 339–345, `arXiv:hep-ph/9310350`.

[264] L. Lee, C. Ohm, A. Soffer, and T.-T. Yu, "Collider Searches for Long-Lived Particles Beyond the Standard Model," *Prog. Part. Nucl. Phys.* **106** (2019) 210–255, `arXiv:1810.12602 [hep-ph]`. [Erratum: Prog.Part.Nucl.Phys. 122, 103912 (2022)].

[265] O. Buchmueller, A. De Roeck, K. Hahn, M. McCullough, P. Schwaller, K. Sung, and T.-T. Yu, "Simplified Models for Displaced Dark Matter Signatures," *JHEP* **09** (2017) 076, `arXiv:1704.06515 [hep-ph]`.

[266] R. Capdevilla, F. Meloni, R. Simoniello, and J. Zurita, "Hunting wino and higgsino dark matter at the muon collider with disappearing tracks," *JHEP* **06** (2021) 133, `arXiv:2102.11292 [hep-ph]`.

[267] S. Bottaro, D. Buttazzo, M. Costa, R. Franceschini, P. Panci, D. Redigolo, and L. Vittorio, "Closing the window on WIMP Dark Matter," *Eur. Phys. J. C* **82** no. 1, (2022) 31, `arXiv:2107.09688 [hep-ph]`.

[268] S. Bottaro, D. Buttazzo, M. Costa, R. Franceschini, P. Panci, D. Redigolo, and L. Vittorio, "The last complex WIMPs standing," *Eur. Phys. J. C* **82** no. 11, (2022) 992, `arXiv:2205.04486 [hep-ph]`.

[269] J. Alimena *et al.*, "Searching for long-lived particles beyond the Standard Model at the Large Hadron Collider," *J. Phys. G* **47** no. 9, (2020) 090501, `arXiv:1903.04497 [hep-ex]`.

[270] M. Cirelli, N. Fornengo, and A. Strumia, "Minimal dark matter," *Nucl. Phys. B* **753** (2006) 178–194, `arXiv:hep-ph/0512090`.